POLITECNICO DI TORINO

Collegio di Ingegneria Chimica e dei Materiali

Master of Science Course
in Materials Engineering

Master of Science Thesis

Electrophoretic co-deposition of Fe-doped MnCo spinel as protective coatings for Solid Oxide Fuel Cells interconnects

Tutor

prof. Federico Smeacetto

Candidate

Elisa Zanchi

September 2018

Ai miei nonni

“Innanzi ed intorno a me non vedevo altro che mare e cielo;
e così fra quelle due immensità abbellite anche molto dai raggi del sole
che si tuffava nell’onde, io mi passava un’ora di delizie fantasticando;
e quivi avrei composte molte poesie,
se avessi saputo scrivere o in rima o in prosa in una lingua qual che si fosse.”

*(*Vittorio Alfieri*, Vita scritta da esso,* 1806*)*

Preface

This thesis is based on the work I carried out from November 2017 to June 2018, in a joint research between the Department of Applied Science and Technology, Politecnico di Torino (POLITO) and the Department of Energy Conversion and Storage, Technical University of Denmark (DTU).

The samples were prepared at the laboratories of POLITO, under the supervision of Dr. Antonio G. Sabato and Prof. Federico Smeacetto.

I have conducted all the experimental characterizations at DTU, supervised and supported by Dr. Belma Talic and the all section of Mixed Semiconductors (MIX), headed by Prof. Peter Vang Hendriksen.

All the microscopic characterization was done by me independently, at DTU.

Some new experiments are now running at the Gdansk University of Technology, Poland, by Dr. Sebastian Molin.

Abstract

Solid oxide fuel cells (SOFCs) are considered a promising technology for the production of clean energy. Ferritic stainless steels are widely used as interconnects in the SOFC stack. The development of volatile Cr-containing species, which can poison the cathode are the main causes of degradation of the device.

Manganese cobalt-based spinels (MCO) have been proposed as protective coating materials for metallic interconnects due to their high electrical conductivity and the good CTE match with the steel substrates. The doping of the spinel structure by transition metals leads to the modification of its properties, with the possibility to improve the coating performances.

In this work, undoped and Fe-doped MCO spinel coatings were produced, by electrophoretic co-deposition of $Mn_{1,5}Co_{1,5}O_4$ and Fe_2O_3 as iron precursor; two suspensions with increasing amount of iron oxide were prepared. Crofer 22 APU, an alloy specially developed as SOFC interconnect, and the commercial AISI 441 were used as substrates for the deposition.

The coatings were sintered by a two-step heat treatment, performed in different atmospheres and at different temperatures. Dense and continuous coatings were obtained. The achievement of the "in-situ" formation of the modified spinel was verified by XRD.

The effect of the Fe-doping was studied for both the substrates in comparison with the undoped coating. All coated samples were tested in relevant conditions at 750°C in air atmosphere and following experimental approach was used:

-The oxidation kinetics were evaluated by thermogravimetric analysis, up to 2000 h at 750 °C, demonstrating that the Fe addition remarkably reduces the parabolic oxidation rate for Crofer 22 APU.

-The electrical properties were tested in terms of area specific resistance (ASR), up to 3200 h at 750 °C, using $La_{0,85}Sr_{0,1}Mn_{1,1}O_3$ (LSM) contact plates, that simulate the interactions with the SOFC cathode. The results were compared with those obtained by ASR measurement with platinum contacts on the samples aged for 1000 and 2000 h at the same temperature.

All Crofer 22 APU samples exhibited an increasing ASR starting from ca. 1500 h, likely due to the formation of a Cr-rich reaction layer between the oxide scale and the coating.

Despite the microscopic analysis detected the presence of a continuous silica layer on the surface of AISI 441 samples after 3200 h aging, this steel showed a better ASR stability over time at constant temperature.

Based on these results, two different oxidation mechanisms for Crofer 22 APU and AISI 441 were proposed.

Riassunto

Introduzione

La ricerca in campo energetico sta affrontando due tematiche contrapposte: da un lato la crescente domanda mondiale di energia, dall'altro la necessità di ridurre l'emissione dei gas serra. A tal proposito, le fonti di energia rinnovabile, principalmente solare e eolico, hanno guadagnato notevole attenzione. Tuttavia, uno dei fattori limitanti per il loro utilizzo è la fluttuazione della produzione, che risulta talvolta in eccesso rispetto alla richiesta, talvolta insufficiente.

Una possibile soluzione a tale problematica è rappresentata dalla creazione di storage, in cui il surplus energetico possa essere immagazzinato in forma di energia chimica e ritrasformato in elettricità all'occorrenza. Ciò può essere ottenuto utilizzando le celle ad ossidi solidi (SOC), ulteriormente classificate in celle elettrolitiche (SOEC) e celle a combustibile (SOFC), a seconda della modalità di utilizzo.

In particolare, le SOFC sono dispositivi in grado di convertire energia chimica in elettrica, sfruttando reazioni di ossidoriduzione ad alta temperatura (500-800 °C); l'assenza di reazioni di combustione evita la formazione di gas inquinanti come sottoprodotti. Una cella è composta da tre elementi (Figura 1): il catodo, a contato con l'atmosfera ossidante, l'anodo, a contatto con quella riducente, entrambi separati da un elettrolita solido responsabile della migrazione degli ioni ossigeno.

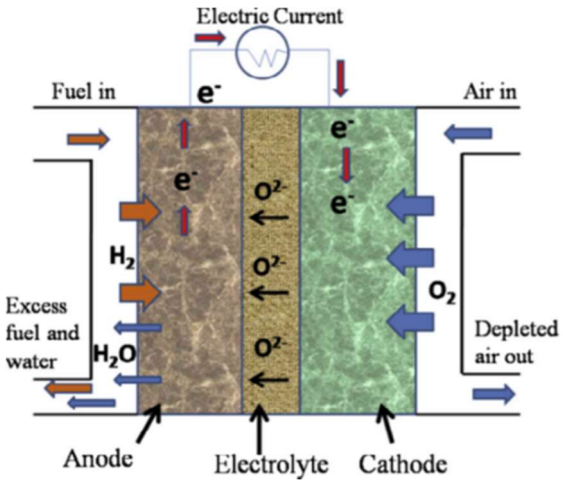

Figura 1: Schema di una unità SOFC [1]

Una sola cella non è però sufficiente a garantire una realistica potenza in uscita; per questo motivo, le unità SOFC sono generalmente impilate a formare una stack, in cui ogni cella è separata da quelle adiacenti attraverso un interconnettore. Questo elemento ha il duplice compito di garantire la connessine elettrica tra le celle e il circuito esterno e di smistare i gas in entrata e uscita, evitando che le atmosfere entrino in contatto. Il materiale scelto per la sua realizzazione deve quindi essere caratterizzato da elevata conducibilità elettrica e termica, avere buona resistenza termo-meccanica, deve essere impermeabile ai gas, deve essere chimicamente compatibile con anodo e catodo e deve presentare un coefficiente di dilatazione termica (CTE) simile a quello degli altri componenti della cella (tra 10-11x10^{-6} K^{-1}).

Gli acciai inossidabili ferritici (FSS) sono ad oggi la classe di materiali più utilizzata, in quanto offrono il miglior rapporto proprietà/costo. Tuttavia, quando mantenuti ad alta temperatura per un lungo periodo, essi vanno incontro a due problematiche, causando la degradazione dell'intera stack: corrosione, che

porta all'inspessimento dello strato superficiale di Cr_2O_3 e alla riduzione della conducibilità elettrica, e formazione di composti volatili del cromo, che danno luogo a processi di avvelenamento del catodo.

Per ovviare a questi inconvenienti sono state sviluppate delle apposite leghe contenenti elevati quantità di cromo, manganese, terre rare, e bassissimi livelli di impurezze ottenuti tramite costose tecniche di fusione sottovuoto; tuttavia questi accorgimenti non si sono dimostrati sufficienti.

È quindi stata ormai riconosciuta la necessità di applicare rivestimenti protettivi (coating) all'acciaio al fine di prolungare la vita del dispositivo (stimata ad almeno 40000 h). Gli spinelli a base di manganese e cobalto (MCO) sono la tipologia più studiata, grazie alla notevole conducibilità elettrica (tra 50 e 90 Scm^{-1}), adeguato CTE (tra 13 e 9 $x10^{-6}K^{-1}$), efficacia nel ridurre l'ossidazione del metallo e buona adesione con il substrato. La formulazione più utilizzata è $Mn_{1,5}Co_{1,5}O_4$, che a temperatura ambiente risulta essere una miscela dello spinello cubico $MnCo_2O_4$ a di quello tetragonale Mn_2CoO_4, ma che si trasforma nella fase interamente cubica sopra i 400 °C. Esso è un semiconduttore, in cui la conducibilità elettrica è assicurata dalle interazioni tra gli elettroni e le lacune elettroniche ed è quindi molto sensibile sia alla temperatura sia ai difetti reticolari.

A tal proposito, la nuova prospettiva che ad oggi si sta investigando è la modificazione della struttura cristallina dello spinello Mn-Co, tramite dopaggio con metalli di transizione, per verificare se e quali proprietà del rivestimento risultino migliorate. Tali spinelli modificati sono generalmente ottenuti sfruttando le stesse tecniche di produzione dello spinello di partenza (come reazioni allo stato solido, processi sol-gel, spray pirolisi) che possono quindi essere definite "ex situ", in quanto precedenti al processo di deposizione del coating stesso.

L'obiettivo di questa tesi è quindi quello di verificare la possibilità di ottenere un drogaggio "in-situ" (cioè contemporaneo al processo di produzione del rivestimento stesso) dello spinello di partenza con ferro e di valutare le proprietà dei rivestimenti ottenuti su due acciai.

Il primo substrato scelto è il Crofer 22 APU, una costosa lega appositamente progetta per interconnettori di SOFC; il secondo è l'AISI 441, un FSS commerciale, adatto per applicazioni ad alta temperatura, che differisce dal primo per il minor contenuto di cromo in lega, l'assenza di terre rare e una tolleranza molto più ampia sul livello di impurezze. Entrambi sono FSS, per cui si suppone che la formazione e la crescita dello strato passivante di ossido di cromo sulla superficie sia regolata dalla diffusione di ioni, come schematizzato in Figura 2. Un meccanismo di tale specie è caratterizzato da una velocità di crescita decrescente nel tempo (a causa dell'estensione del cammino di diffusione) ed è definito parabolico.

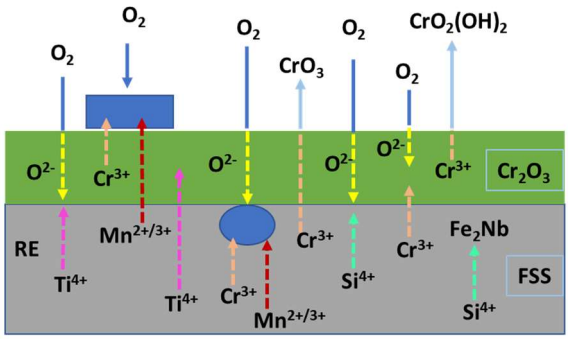

Figura 2: Schematizzazione del meccanismo di formazione dello strato passivante su acciaio inossidabile ferritico.

Metodi e procedure sperimentali

I rivestimenti sono stati prodotti utilizzando la tecnica di deposizione elettroforetica (EPD), un metodo di sintesi che sfrutta il movimento di particelle cariche all'interno di una soluzione o dispersione, quando al sistema è applicato un potenziale elettrico. Il principio alla base dell'EPD è la capacità delle superfici

di acquisire una carica superficiale, dipendente principalmente dai gruppi chimici presenti sulle superfici stesse e dal pH del liquido con cui sono a contatto.

In questo caso le sospensioni sono state preparate con una soluzione contenente 60 wt. % di etanolo e 40 wt. % di acqua, cui è stata aggiunta una quantità di fase solida tale da raggiungere una concentrazione di 37,5 gL^{-1}. Le polveri utilizzate sono lo spinello $Mn_{1,5}Co_{1,5}O_4$ e Fe_2O_3, come precursore del ferro. Esse sono state aggiunte alla soluzione in modo da ottenere tre sospensioni differenti: la prima, nominata MCO, contenente solo $Mn_{1,5}Co_{1,5}O_4$, la seconda e la terza contenenti rispettivamente 5 e 10 wt. % di Fe_2O_3, e per questo chiamate 5FeMCO e 10FeMCO.

Le deposizioni sono state effettuate applicando una differenza di potenziale di 50 V ai due elettrodi (entrambi situati a 1 cm di distanza dai campioni) per 20 secondi.

In Figura 3 è mostrata una foto della strumentazione utilizzata per la deposizione.

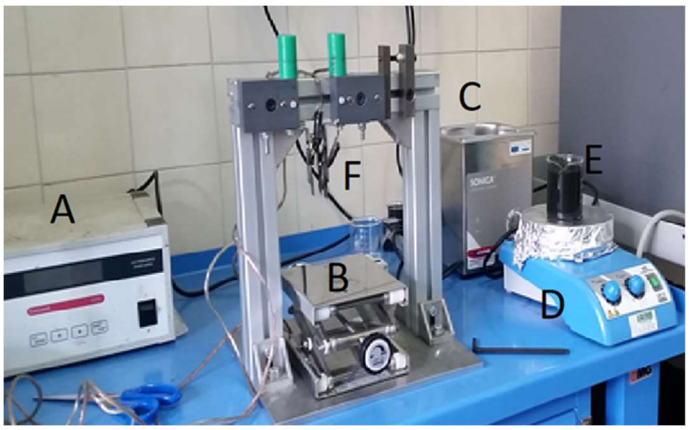

Figura 3: Strumentazione utilizzata per l'EPD. A) alimentatore, B) supporto, C) bagno ultrasonico, D) agitatore magnetico, E) sospensione, F) elettrodi.

I rivestimenti sono stati consolidati tramite una sinterizzazione in due step. Il primo è la riduzione (Ar/H_2, 2 h, 900 °C), poi seguita da una ri-ossidazione (aria, 2 h, 900 °C). Si è inoltre scelto di sottoporre un set di campioni rivestiti con il 10FeMCO ad una riduzione a più alta temperatura (1000 °C anziché 900 °C), mantenendo invariati tutti gli altri parametri. I campioni di tale tipologia sono stati chiamati 10FeMCO_R1000.

Dopo entrambi gli step di sinterizzazione, i campioni sono stati caratterizzati tramite XRD e FE-SEM.

L'adeguatezza degli acciai rivestiti come materiali per interconnettori è stata studiata in base alla resistenza alla corrosione ad alta temperatura e della conducibilità elettrica dei campioni.

Per quanto riguarda il primo punto, essa è stata valutata tramite misurazioni termo-gravimetriche: i campioni sono stati mantenuti a 750 °C a cicli di 250 h, al termine di ognuno dei quali sono stati pesati, per un totale di 2000 h. Il concetto fondante alla base di tale metodo risiede nel fatto che, quando non avvengono fenomeni di perdita di materiale (spallation), tutto l'aumento di peso registrato nel corso del tempo è attribuibile alla presa di ossigeno necessaria per la formazione dello strato di ossido di cromo tra acciaio e rivestimento. Pertanto, calcolando la variazione dell'aumento di peso nel tempo, possono essere individuate le cinetiche di ossidazione, nonché i meccanismi da cui sono regolate.

Le proprietà elettriche sono invece state valutate seguendo due metodi, entrambi basati sul calcolo della resistenza specifica di area (ASR) [$\Omega\ cm^2$].

Per il primo, sono stati utilizzati contatti di $La_{0,85}Sr_{0,1}Mn_{1,1}O_3$ (LSM), materiale di cui sono costituiti i catodi e che risulta quindi utile per simulare la conducibilità dell'interconnettore nell'ambiente della cella. I campioni sono stati posizionati come mostrato in Figura 4. Due fogli di oro sono stati posizionati alle due estremità della stack per distribuire la potenza elettrica; la caduta di potenziale su entrambe le

superfici di ogni campione è stata misurata tramite una resistenza esterna collegata ai fili di platino saldati sui campioni stessi. Le misurazioni sono state registrate in modo continuativo per 3200 h alla temperatura costante di 750 °C, applicando una densità di corrente pari a 0,5 Acm^{-2}.

Figura 4: Foto della disposizione dei campioni per la misura di ASR con contatti di LSM.

Per il secondo metodo di misurazione dell'ASR sono stati invece utilizzati i campioni invecchiati per 1000 e 2000 h, sui quali sono stati depositati dei contatti di platino (Pt sputtering seguito da platinum paste brushing). Sono state dunque eseguite misure di impedenza puntuali in condizione di corrente quasi continua (0,1-1 Hz), durante il raffreddamento, a partire da 750 °C. Dalla dipendenza dell'ASR rispetto alla temperatura è stato possibile calcolare l'energia di attivazione per la conduzione dei semiconduttori. Avendo utilizzato contatti costituiti da un metallo nobile che, a differenza dell'LSM, non reagisce con il rivestimento, tale metodologia è stata seguita per ottenere una valutazione più teorica del meccanismo di conduzione dato dai coating.

L'analisi FE-SEM/EDS è stata eseguita sui campioni invecchiati a 750 °C in aria in seguito a regolari intervalli di invecchiamento, come mostrato in Figura 5.

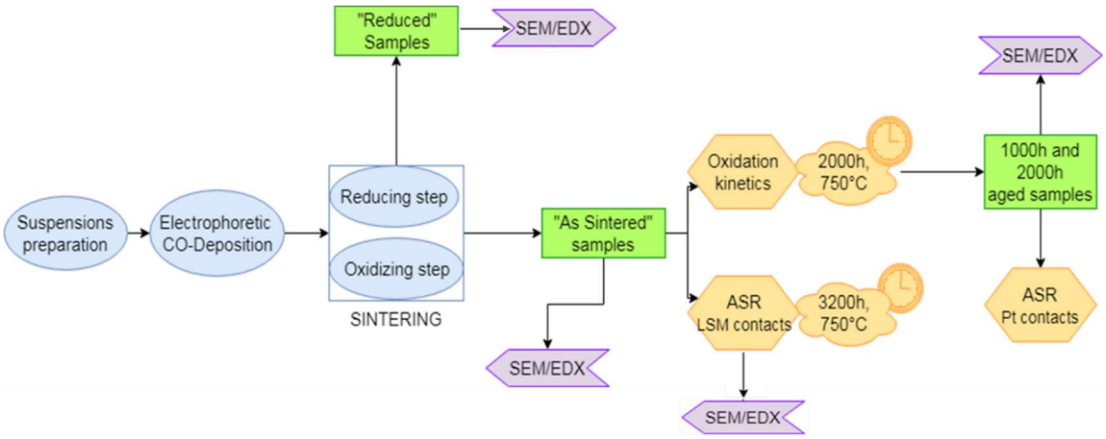

Figura 5: Schema del lavoro sperimentale svolto per questa tesi.

Risultati

La prima parte di caratterizzazione è stata incentrata sulla verifica dell'avvenuta reazione tra lo spinello di manganese cobalto e l'ossido di ferro co-depositati mediante EPD.

L'analisi dei patterns XRD dei rivestimenti dopo trattamento di riduzione ha confermato la decomposizione dei composti in ossido di manganese, cobalto metallico e composto intermetallico ferro-cobalto ($Co_{0,7}Fe_{0,3}$). L'aggiunta del ferro sembrerebbe inoltre favorire la miglior dispersione

e il coarsening del cobalto in particelle sferiche, effetto ulteriormente intensificato dalla maggiore temperatura di riduzione.

Dopo la ri-ossidazione la stessa analisi XRD ha confermato la formazione dello spinello Fe-Mn-Co, in fase cubica e tetragonale: a tal proposito, l'analisi EDS ha inoltre suggerito che negli spinelli modificati fosse presente una alternanza più fine dei grani delle due fasi, che risulterebbero quindi avere dimensione in generale inferiore. In ogni caso, l'assenza di ossido di ferro residuo ha dunque confermato la possibilità di raggiungere "in-situ" il drogaggio dello spinello iniziale con il ferro.

La ricerca è poi stata focalizzata sulla caratterizzazione del comportamento dei due acciaio con i rivestimenti prodotti.

La Figura 6 mostra i dati di aumento di peso registrati per i campioni di Crofer 22 APU e AISI 441. Come si può apprezzare, i valori misurati per il secondo acciaio sono sensibilmente superiori; inoltre, essi seguono approssimativamente delle linee rette. Invece, i valori del Crofer 22 APU sono posizionati secondo un andamento parabolico.

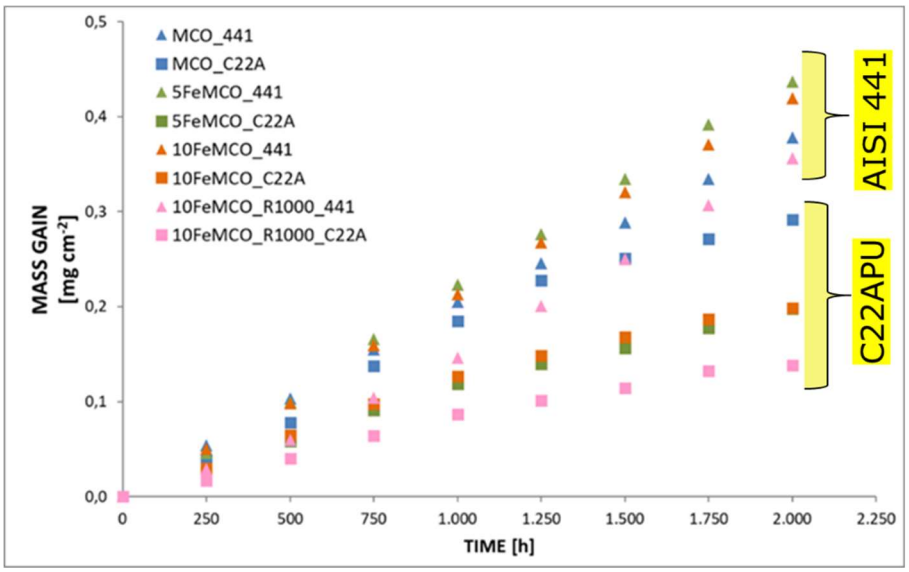

Figura 6: Aumento di peso versus tempo dei campioni studiati (750°C, 2000 h).

L'ultima considerazione è meglio verificata inserendo nel grafico l'aumento peso in unità paraboliche, che equivale ad applicare la legge parabolica:

$$\left(\frac{\Delta m}{A}\right)^2 = k_{p,m}t + C$$

dove $\left(\frac{\Delta m}{A}\right)^2$ è l'aumento di peso su unità di area superficiale elevato alla seconda potenza [g^2cm^{-4}], t è in tempo [s], C è una costante di integrazione e $k_{p,m}$ è la velocità di ossidazione parabolica espressa secondo l'aumento di peso [$g^2cm^{-4}s^{-1}$].

La Figura 7 mostra quanto appena espresso per i campioni di Crofer 22 APU, da cui si può notare che in tal caso l'aumento di peso segue un andamento perfettamente parabolico. La velocità di ossidazione è quindi ricavabile dalla pendenza delle rette in figura.

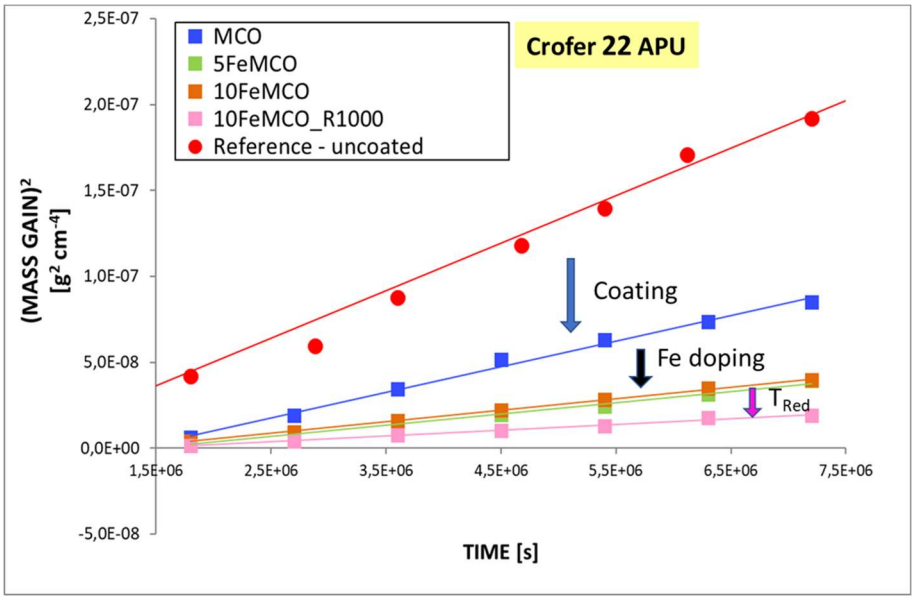

Figura 7: Aumento di peso in unità paraboliche per i campioni di Crofer 22 APU.

Come si può vedere dalla Figura 7, l'applicazione del rivestimento a base di MCO, riduce notevolmente l'ossidazione dell'acciaio, che è ulteriormente migliorata dal drogaggio con il Fe dello spinello e dalla maggiore temperatura applicata durante il trattamento riducente ella sinterizzazione.

Non è stato possibile applicare lo stesso ragionamento ai campioni di AISI 441, i quali hanno dimostrato un andamento para-lineare, con un $k_{p,m}$ non costante, ma crescente nel tempo; inoltre, lo stesso trend legato al drogaggio con Fe non è stato verificato.

L'analisi microscopica ha permesso di comprendere il motivo di questo diverso comportamento.

Infatti, al termine delle 2000 h di ossidazione, è stata appurata la presenza di cristalli, più precisamente spinelli misti Mn-Cr-Co, sulle superfici dei rivestimenti sul solo AISI 441; forma e dimensione di tali composti si è rivelata dipendente dal livello di doping. In Figura 8 sono mostrati gli spinelli di forma allungata cresciuti su 10FeMCO.

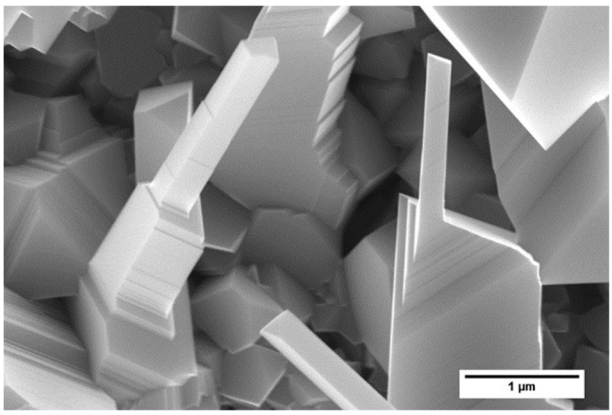

Figura 8: Immagine FE-SEM della superficie di 10FeMCO su AISI 441 dopo 2000 h a 750°C.

L'origine di tale quantità di cromo sulla superficie dei rivestimenti è stata identificata nella frattura o delaminazione avvenuta tra il coating e lo stesso acciaio durante i cicli termici, a causa del diverso CTE. Di contro, i campioni di Crofer 22 APU hanno confermato avere un'ottima interfaccia coating/substrato (Figura 9).

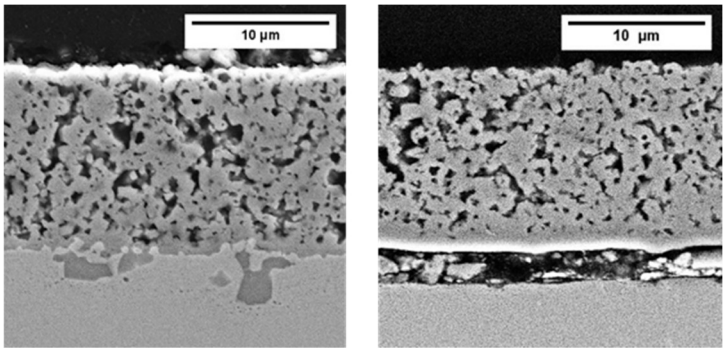

Figura 9: Immagini FE-SEM del cross sections dei coating 10FeMCO
su Crofer 22 APU (sinistra) e AISI 441 (destra), dopo 1000 h di invecchiamento.

Le misurazioni di conducibilità elettrica hanno rivelato in tutti i casi valori adatti per l'utilizzo come interconnettori: le ASR misurate rientrano infatti nell'intervallo 24,3 - 32,0 mΩcm^2.

Tuttavia, i due acciai hanno dimostrato comportamenti opposti anche in questo frangente.

In Figura 10 sono mostrati i dati di ASR con contatti di LSM, relativi ai campioni di Crofer 22 APU. La prima parte delle curve ha un andamento decrescente dovuto alla sinterizzazione dei contatti in LSM, che porta alla progressiva diminuzione della resistenza. A partire da circa 1000-1500 h le linee mostrano però valori crescenti, sintomo dell'attivazione di meccanismi di reazione con conseguente formazione di composti a conducibilità inferiore a quella del rivestimento depositato. In prima istanza, tale aumento della ASR può essere attribuito all'inspessimento dello strato di ossido di cromo.

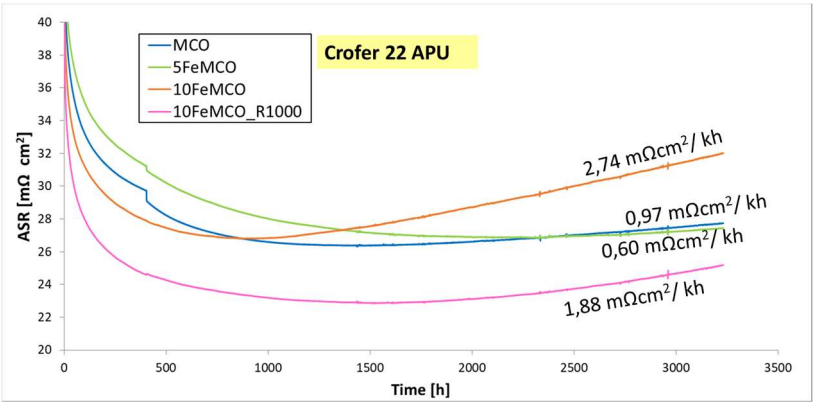

Figura 10: Misurazioni di ASR con contatti di LSM per i campioni di Crofer 22 APU.

I casi peggiori sono stati registrati per i coating con il livello di doping maggiore; infatti, estrapolando la pendenza della retta di degradazione fino a 40 000 ore, si ottengono valori di resistenza troppo elevati per un interconnettore. Tuttavia, come già discusso, la formazione dello strato passivante è governata da legge parabolica, per cui risulta che la previsione fatta rappresenti l'ipotesi più pessimistica.

Al contrario, tutti i campioni di AISI 441 hanno mostrato un valore di ASR completamente stabile nel tempo, da cui si potrebbe dedurre che la velocità di crescita dello strato di ossido tra acciaio e rivestimento sia trascurabile. Questa valutazione è tuttavia in contrasto con quanto osservato al microscopio al termine delle misurazioni (3200 h).

In Figura 11 è presentata una mappa EDS dell'interfaccia AISI 441/10FeMO, da cui si può notare la presenza di un regolare strato di Cr_2O_3 dello spessore di circa 2 µm, cresciuto verso l'esterno della superficie dell'acciaio.

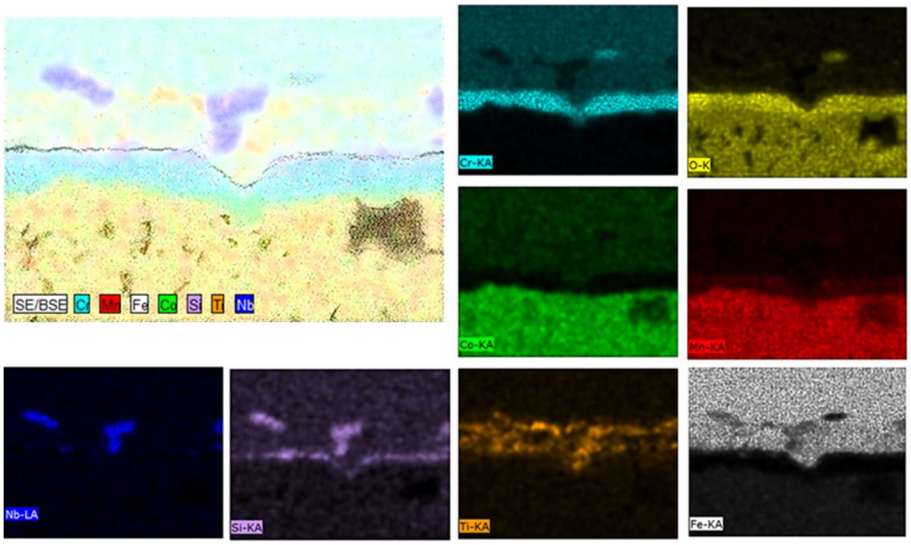

Figura 11: Mappa EDS di 10FeMCO_R1000 di AISI 441, dopo 3200 h a 750 °C.

In aggiunta al Cr_2O_3, è presente anche uno strato continuo di ossido di silicio, con proprietà isolanti; ciò prova l'insufficienza dell'aggiunta i Nb in lega, atto a formare le cosiddette "Laves phase", composti intermetallici Fe-Nb, che dovrebbero evitare la diffusione del silicio. Inoltre, nella zona sub-superficiale, si è osservata una notevole concentrazione di ossidi di titanio.

Infine, si può notare la presenza di una cricca lungo tutta l'interfaccia tra ossido di cromo e di silicio; tale frattura è avvenuta durante il raffreddamento del forno a causa della differenza di CTE tra le due fasi. Questa evidenza ha confermato che l'ottimo comportamento in ASR dell'AISI 441 avrebbe in realtà avuto un esisto disastroso qualora fossero stati applicati dei cicli termici.

Sul motivo per cui le misurazioni ASR dei campioni di AISI 441 non abbiano mostrato un andamento crescente, nonostante la presenza di uno strato piuttosto spesso di Cr_2O_3 (semiconduttore con scarsa conducibilità elettrica) e di uno di silice (isolante), non sono state raggiunte conclusioni certe. Una ipotesi potrebbe essere legata alla notevole diffusione di cationi metallici dall'acciaio stesso, in particolare del titanio. Infatti, la conducibilità dei materiali semiconduttori è fortemente influenzata anche da livelli di drogaggio decisamente limitati.

Per confronto, la Figura 12 mostra la mappa EDS della sezione dello stesso rivestimento applicato sul Crofer 22 APU.

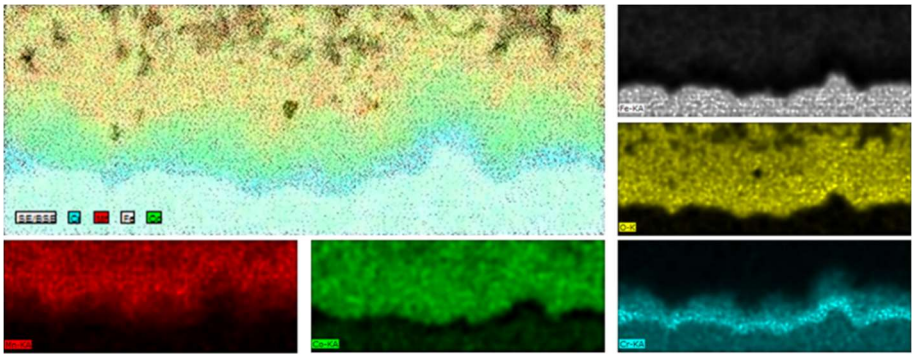

Figura 12: Mappa EDS di 10FeMCO_R1000 di Crofer 22 APU, dopo 3200 h a 750°C.

Dalla Figura 12 si può notare che in questo acciaio lo strato di ossido di cromo è molto più sottile (inferiore a 1 μm) e ha una morfologia piuttosto irregolare. Rilevante è anche la presenta di un denso

strato di reazione (RL) formato dall'inter-diffusione del cobalto e del cromo, che nei campioni di AISI 441 non è stato individuato. Inoltre, è stato notato che i rivestimenti contenenti ferro hanno formato uno strato di coating densificato proprio a contato con il RL: ciò è stato parzialmente spiegato ipotizzando che la modificazione della struttura cristallina tramite aggiunta di alcuni atomi di ferro abbia causato un aumento del disordine e quindi quella reattività.

La crescita dei due strati appena descritti è quindi stata ritenuta il fattore che ha causato l'aumento dell'ASR registrato per il Crofer 22 APU; di contro, essi risultano positivi per la protezione dell'acciaio contro l'ossidazione.

Nel tentativo di fornire una spiegazione complessiva dei risultati ottenuti, sono di seguito presentati i due diversi meccanismi di ossidazione ipotizzati, che relazionano le caratteristiche dei due acciai con quelli dei rivestimenti depositati.

La Figura 13 mostra il meccanismo ipotizzato per Crofer 22 APU. Lo schema è stato ottenuto modificando una immagine della sezione del campione rivestito con 10FeMCO, dopo un invecchiamento di 3200 h.

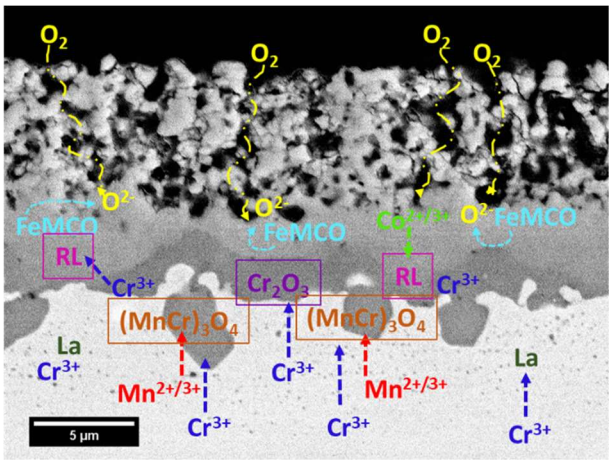

Figura 13: Meccanismo di ossidazione proposto per Crofer 22 APU (campione dopo 3200 h a 750°C).

La morfologia del rivestimento regola come l'ossigeno possa migrare nei pori fino a raggiungere il substrato; affinché avvenga l'ossidazione, gli ioni ossigeno devono diffondere fino a reagire con i cationi del cromo. Tuttavia, come segnalato nell'immagine, la presenza di La permette al Crofer 22 APU di raggiungere un'elevata ritenzione di cromo, con l'effetto di ridurre la sua velocità di diffusione verso la superficie. Inoltre, anche l'aggiunta del manganese risulta molto vantaggiosa per lo stesso motivo: si è infatti verificato che tale elemento forma spinelli Mn-Cr sotto la superficie dell'acciaio.

Data la scarsa mobilità dei cationi Cr^{3+}, la crescita dello strato di ossido verso l'esterno è limitata: risultano quindi favorite le cinetiche di reazione tra Cr_2O_3 e rivestimento, per diffusione del cobalto, che portano alla formazione del RL.

Infine, lo strato densificato presente nei rivestimenti dopati, ma non nell'MCO puro, è dato dalla maggiore reattività dello spinello modificato verso la riduzione dell'ossigeno.

In Figura 14 è invece proposto il meccanismo di ossidazione per l'AISI 441.

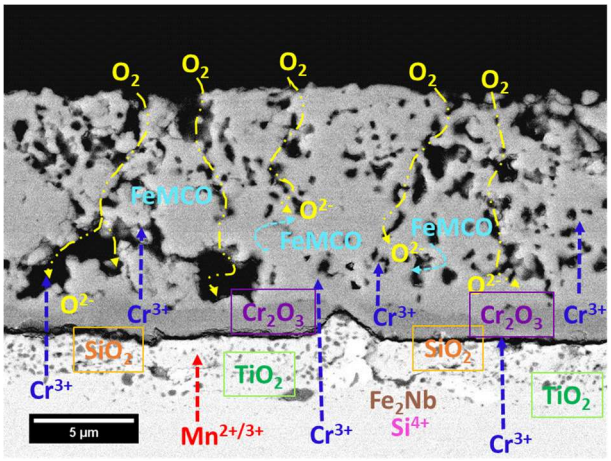

Figura 14: Meccanismo di ossidazione proposto per AISI 441
(campione dopo 3200 h a 750°C)

Come è evidente, la morfologia è molto distante da quella del caso precedente.

Innanzitutto, si può notare la diversa interfaccia coating/acciaio. Nel caso dell'AISI 441, la formazione di due strati a composizione ben definita di ossido di cromo e di silice facilita la formazione di cricche per diverso coefficiente di dilatazione termica.

L'assenza di terre rare, la scarsa aggiunta di Mn in lega, come anche l'effetto meno protettivo dello strato passivante, fanno sì che la diffusione del cromo sia il meccanismo preponderante, rispetto alla diffusione verso l'intero degli ioni ossigeno. Infatti, lo strato di cromia cresce verso l'esterno dell'acciaio (all'opposto di quanto avviene per il Crofer 22 APU).

La velocità di diffusione verso l'esterno dei cationi risulta aumentata dalla formazione di ossidi sub superficiali, tipicamente di titanio e silicio: essi, formando fasi secondarie, aumentano l'estensione dell'area dei bordi di grano, siti con elevata concentrazione di difetti dove la diffusione è facilitata.

Riguardo al coating, si può inoltre notare che, a parte le porosità piuttosto evidenti e che costituiscono i canali preferenziali per la migrazione verso l'interno dell'ossigeno, il rivestimento è in generale molto densificato lungo tutto lo spessore. Ciò è il risultato sia della costante diffusione di metalli dall'interno e della maggiore reattività del rivestimento contenente ferro.

In tal caso il RL, che è stato dimostrato entrare in gioco solo quando la cinetica della diffusione del cromo diventa pressoché irrilevante, non si può formare.

Conclusioni

Il presente lavoro di tesi ha portato alle seguenti conclusioni:

- La co-deposizione elettroforetica è un metodo di sintesi valido per l'ottenimento "in-situ" di spinelli MCO modificati con metalli quali il Fe. Un successivo sviluppo di tale metodo potrebbe riguardare la co-deposizione di ossido di cobalto, ossido di manganese e ossido di ferro come precursori dell'intero spinello.
- Applicare un rivestimento di spinello manganese-cobalto dopato con ferro migliora la resistenza a corrosione del Crofer 22 APU; resta da valutare più approfonditamente l'effetto sull'ASR della crescita dello strato di reazione.
- Il comportamento dell'AISI 441 non ha dimostrato essere migliorato dall'applicazione degli stessi rivestimenti. A tal proposito, sembra necessario svolgere delle misurazioni di evaporazione del cromo, al fine di correlare in modo più chiaro i dati dell'ossidazione con quelli della resistenza elettrica.

Contents

Preface i
Abstract iii
Riassunto v
1. Introduction 1
1.1. Background 1
1.2. Aim of the work 6
1.2.1. Thesis outline 6
1.3. Materials 7
1.3.1. Manganese cobalt spinel: structure, properties and doping possibilities 7
1.3.2. Ferritic stainless steels: Crofer 22 APU and AISI 441 11
1.3.1. FSS and MCO at high temperature: critical issues 13
1.4. Theory and methods 15
1.4.1. Electrophoretic deposition 15
1.4.2. Sintering 19
1.4.3. High temperature oxidation 20
1.4.4. Electrical conductivity of interconnects 23
2. Experimental procedures 25
2.1. Samples preparation 25
2.2. Characterization 29
2.2.1. Oxidation and gravimetric measurements 29
2.2.2. Area specific resistance 31
3. Results and discussion 37
3.1. Microstructural investigation of the reduced and as sintered samples 37
3.2. Oxidation kinetics 43
3.2.1. Microstructural investigation of the 1000 and 2000 h aged samples 47
3.2.2. Surface reactivity and chromium absorption 62
3.3. ASR: comparison between the “in situ” and “ex situ” methods 63
3.3.1. Microstructural investigation of the 3200 h aged samples 67
3.4. Oxidation mechanisms 75
4. Conclusions 83
4.1. In-situ Fe-doping by electrophoretic co-deposition 83
4.2. Suitability of Fe-doped MCO coatings for Crofer 22 APU 83
4.3. Suitability of Fe-doped MCO coatings for AISI 441 84
4.4. Future perspectives 84
Abbreviations 85
Bibliography 86

1. Introduction

1.1. Background

The research in the energy production field is facing two issues: on the one hand the increasing of the demand ([2], [3]), on the other, the need to reduce the production of greenhouse gases [4]. In this context, the renewable energy sources, such as wind or solar power, are playing a key role in the debate on how the traditional energy production methods could be replaced [5].

A greater development of renewable energies would be advantageous non only from an environmental point of view, but also from the economic and political one, thanks to the possibility of reducing the energy dependency on foreign countries [6].

One of the issues related to the exploitation of solar and wind energy is related to the fluctuation of power production, caused by the alternation of the seasons, day and night, as well as atmospheric events; this made it necessary to think about a mean to store excess energy, so that it was usable when it was impossible to provide some new one [7]. One possible way is to create chemical energy storages.

In this scenario, fuel cells (FC) and electrolyser cells (EC), devices able to convert respectively chemical energy into electricity and the opposite, through electrochemical reactions, have gained much attention.

Many different types of them have been proposed, differing mainly for the materials used in the manufacturing, for the operating temperatures, for the ionic species involved in the reactions and the nature of fuels employed ([8], [9]).

Among them, there are the Solid Oxide Fuel Cells (SOFC), which are the topic of this work and whose schematization is illustrated in the Figure 1.1.

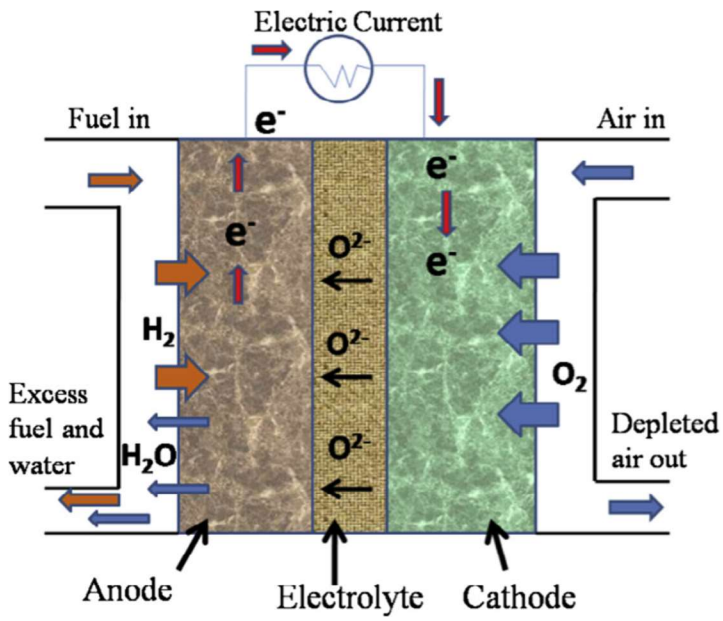

Figure 1.1: Scheme of a SOFC unit, adapted from [1].

As shown in Figure 1.1, the SOFC unit is made up of two electrodes, an anode, where the fuel comes to, and a cathode in contact with the air; both are separated by an electrolyte, responsible for the ions diffusion.

The operating principle of the cell can be summed up by the following two equations:

$$\text{Cathode} \quad \frac{1}{2}O_{2(g)} + 2e^- \rightarrow O^{2-}$$

$$\text{Anode} \quad H_{2(g)} + O^{2-} \rightarrow H_2O + 2e^-$$

As it can be seen, oxygen molecules react at the cathodes with electrons, forming oxygen ions; these diffuse through the electrolyte till they reach the anode, where they react with hydrogen; therefore, for every hydrogen molecule added to the system, two electrons are produced, which can be used as electricity, and the only by product of the overall system is water.

It is important to note that, in order to make the reactions described above with high efficiency, appropriate materials should be selected.

The cathodes must have high catalytic activity for the oxygen reduction and be stable in the oxidizing atmosphere: for this aim the most widespread are the perovskite family composites, mainly the lanthanum strontium manganite perovskite (LSM) and its doped compounds [10].

Conversely, as far as anodes are concerned, the most studied materials are Ni/YSZ cermets, which offer high reactivity towards hydrogen oxidation and stability in reducing atmosphere [1].

Both the cathode and anode materials must be porous and have high electrical conductivity.

Then, the most commonly chosen as the electrolyte materials are yttrium or ceria stabilized zirconia (YSZ, CSZ), gadolinium doped ceria (CGO), perovskites such as gadolinium doped LSM, but many other options have been proposed [10], all joined by the property of being good ionic, but poor electronic, conductors; moreover, the electrolyte has to be dense, in order to ovoid gas migration and mixing.

For SOFC supplying, not only hydrogen, but various fuels can be exploited, such us methanol and diesel; anyway, nowadays, the most promising opportunity offered by the SOFC system is to integrate them to other renewable power generators and to provide them with the self-produced hydrogen, previously stored, while operating in the reversible way ([7],[11]).

However, a single cell, as the one in Figure 1.1, can provide an electrical potential of 1 V and a current density of 1 Acm^{-2} [12], which is too low for a realistic power supply; for this reason, many cells are commonly assembled together in order to form a stack.

Figure 1.2 shows the planar configuration of a solid oxide cell stack.

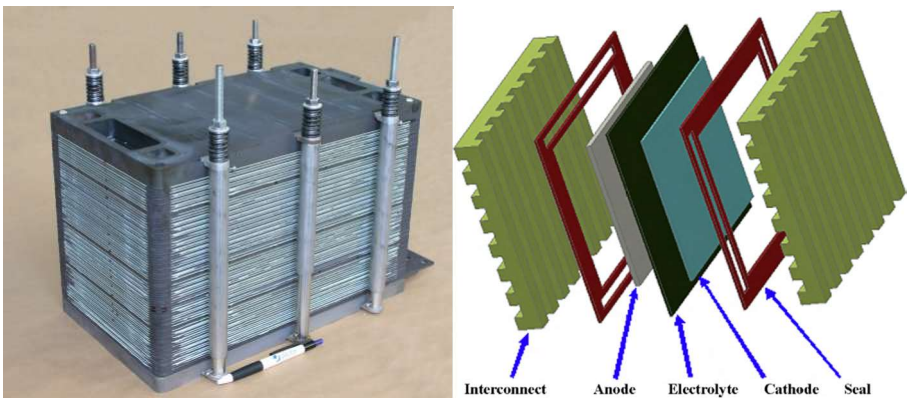

Figure 1.2: a) SOFC planar stack of 5 kW output [13] and b) schematic view of a planar stack [14].

As shown in Figure 1.2, in the stack, each cell is separated from the other by an interconnect, which plays a double role in the system [15]: it is responsible for the electrical connection between the anode of a cell and the cathode of the closest one (and therefore for the power output of the entire stack too), but also for sorting the gasses (air and fuel) involved in the process between anodes and cathodes of adjacent cells, guaranteeing that the two atmosphere do not combine (to this purpose a sealant [16] is also positioned between the cell and the interconnect).

Certainly, before achieving a large-scale commercialization of the SOFC system, many issues need to be solved (as summarized in Figure 1.3); lowering the operating temperature is among the major ones.

Since the ionic conductivity, required at the electrolyte, is a thermally activated process, reaching a reasonable efficiency of the cell has previously made the needed temperature rise up to 1000 °C [17].

Thanks to the efforts directed to the development of lower temperature ionic conductors, as well as new production methods addressed to reducing the electrolyte thickness [18], nowadays SOCF can operate at a temperature between 500 and 800°C [19], which is an advantage for the general stability and durability of the stack components [1], but also for the interconnect improvement.

Figure 1.3 offers an overview of SOCF materials and the related issue for each of them.

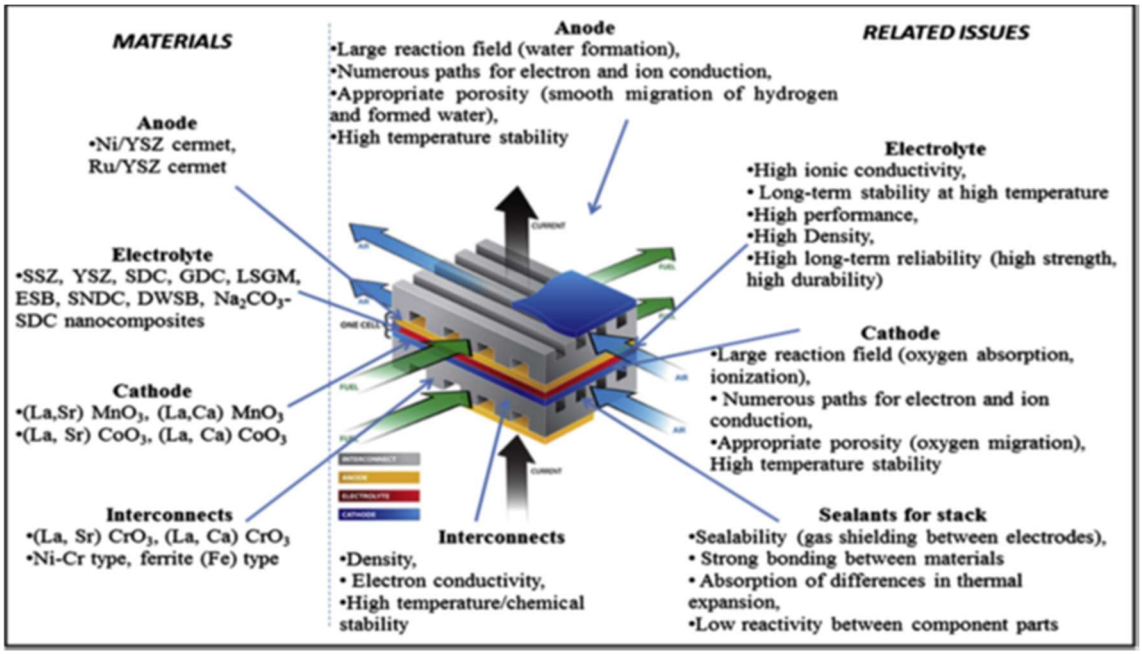

Figure 1.3: Materials and issues of a SOFC stack [1].

Metallic interconnects

As already anticipated, the main functions of the interconnect are to ensure the electrical contact between the cells in the stack and to avoid the reducing and oxidizing atmospheres to mix; in order to meet these requirements, the following conditions, reviewed in [15] and [20], need to be fulfilled:

- High electrical conductivity at the temperature of the cell; the highest area specific resistance has indeed been fixed at 0,1 Ω cm^2 [20];
- Good thermo-chemical stability, in terms of dimension, microstructure and phase transitions at the operating temperatures and in both the reducing and oxidizing atmosphere, mostly because of the relevant oxygen partial pressure gradient between the two sides;

- Low oxygen and hydrogen permeability to prevent the leakage of gasses and the loss in efficiency of the cell. This means that the interconnect material must have high density, maintained for throughout the device service time (fixed at >40000 h [21]);
- A coefficient of thermal expansion (TEC) similar to those of the other components of the cell, from the room temperature till the working one. With reference to the materials commonly used in SOFC, the interconnect TEC should be around $10\times10^{-6}K^{-1}$ ([22], [23]);
- Good chemical compatibility with both the anode and the cathode, with which any reactions should take place, in order to avoid the formation of reacting layers that would affect the yield of the device;
- A thermal conductivity higher of 5 $Wm^{-1}K^{-1}$, necessary to recover the heat and transfer it from the cathode to the anode, where it is used for the fuel reforming;
- Resistance to sulfuration and carburization, considering that sulphur can be present as fuel impurity and also carbon-rich fuel can be exploited instead of pure hydrogen;
- A sufficient high-temperature strength and creep resistance since the interconnect should also act as mechanical support for the entire stack (especially in the planar configuration).

In the past, ceramic materials such as lanthanum chromite of the perovskite family [15] were the only candidates as possible interconnects materials; nevertheless, nowadays, thanks to the research in lowering the operational temperatures of the cells, the most attractive materials are metals, which offer a better compromise to all the listed requirements.
Indeed, compared to the oxides, metals [24]:

- Are cost effective for both the raw materials and the manufacturing process;
- Are more suitable for the mass production;
- Have a better mechanical strength;
- Have higher electrical and thermal conductivity;
- Can be more compliant towards thermo-mechanical stresses, occurring during start-ups and shutdowns (this means that the limits on TEC are less urgent [25]).

A metallic interconnect must also have an acceptable oxidation resistance: this means that, at the operating temperature, it oxidizes forming a protective and conductive oxide layer, which stays stable over time.
Chromia-forming ferritic stainless steels (FSSs) have been proposed as the most suitable class for this application by many authors ([26],[22],[19],[27]) and are nowadays the most widespread material used as interconnects.

Compared to other metallic alloys, the greater advantage of FSS is the formation of a dense and adherent Cr_2O_3 layer on the surface, which results in being more protective as the Cr amount in the alloy increases, and which is an intrinsic semiconductors at high temperature (for this reason FSSs were preferred to alumina or silica forming alloy, which show higher oxidation resistance but much lower conductivity [17]).

However, making use of FSS as interconnect, still two issues persist [20]:

1) High temperature oxidation: over long-time service, the oxidation of the steel causes the thickening of the oxide scale on the surface, which is characterized by a higher electric resistance compared to the metallic alloy, thus resulting in an unacceptable loss of conductivity of the overall interconnect;
2) Cathode poisoning: Cr_2O_3 reacts with water and oxygen molecules in the cathode side of the cell, forming volatile species, mainly $CrO_3(g)$ or $CrO_2(OH)_2(g)$, where Cr is in the 6+ oxidation state. These compounds can not only precipitate on the electrode, reducing the active area available for the oxygen reduction [28], but also migrate to the cathode/electrolyte interface, thus degrading the electrochemical performances of the cell [15].

To overcome these drawbacks, prolong the SOFC life and keep its efficiency high, the use of a protective coating for the steel is the most accepted solution.

Coatings for metallic interconnects: types and application methods

Hence, a protective coating for SOFC interconnect must possess the same requirements of the interconnect (oxidation resistance, electrical conductivity, appropriate CTE, suitability for the large-scale production, etc.); furthermore, it must have a good thermo-mechanical match with the interconnect, reducing its oxidation rate and the Cr evaporation from it.

Many different classes of material have been proposed as suitable candidates: nitrides [29] and reactive elements (La, Ce, Y) [30], but mainly lanthanum based perovskite oxides [31] and spinel oxides.

In particular, the spinels have been preferred to the perovskites by many authors, thanks to their better capability of blocking Cr outwards and oxygen inwards diffusion [20] and to the possibility of sintering and densification at a lower temperatures, thus reducing the steel damaging [17].

Among all the possible spinels available, the $(MnCo)_3O_4$ family has been the most studied one ([22],[32]), mainly thanks to their TEC match with the other components [33] and better adhesion to the steel [34];at the moment they are considered the most promising candidates as interconnect coatings ([19], [35], [36], [37]), Authors in [38] and in [39] concluded that the manganese cobalt spinel coating is advantageous for both the oxidation resistance and electrical conductivity of the interconnect, compared to other oxides families.

However, since the relationship between thickness, morphology and protective properties of the layer is not yet fully understood [40], the best production method to obtain the spinel coting has not been unequivocally identified. Some of the techniques are slurry deposition and spray deposition ([38], [41]), physical vapor deposition [42], thermal spray and thermal oxidation ([43], [44], [45]), plasma spray ([24], [46]), aerosol spray [47], screen printing ([48], [49]).

In [40], $(MnCo)_3O_4$ spinels obtained by three different production methods, sputtering, thermal co-evaporation and electrophoretic deposition (EPD), are tested as effective coating, for 5000 h; in that study, the EPD coating was suggested as the most stable and protective one among the others.

The same result has been achieved in other studies, also thanks to the simple and easy-to-modify set-up of the EPD, compared to other techniques [22].

Many researches focused on the EPD deposition of Mn-Co based spinels with positive results; ([17], [19], [50], [51], [52]). In each of these studies, various sintering methods to make the spinel particles react and form a continuous layer on the steel are proposed.

Anyway, the $(MnCo)_3O_4$ is not the only type of spinel studied as interconnects coatings for SOFC: e.g. also Ni-Co spinel ([53], [54]) , as well as Ni-Fe spinel [55] , Cu-Mn spinel [56], Co alone [57], but generally with less appreciable results; also Cr containing spinel coating were examined (Ni-Cr, Mn-Cr, Co-Cr), but, despite the good thermomechanical match in terms of TEC, they generally showed a low electrical conductivity [22].

Finally, concerning the Mn-Co spinel, the modification of its structure by doping with metallic elements such as Ti [58], Ni [59], Ce [60], but mostly Cu ([33], [59] [61], [62], [63], [64]) and Fe ([35], [65], [66]), is gaining more attention, in order to verify their potential effect on improving both the electrical conductivity, the CTE match and the chromium retention of the coating.

However, in all these studies the doping of the initial Mn-Co spinel was obtained before the actual coating application, following what can be called an “ex-situ” procedure. Some of the methods exploited involved high energy ball milling ([33], [66]) and high temperature solid state reaction [58], sol-gel processes [59] with nitrates ([60], [62]) and acid solutions ([61], [63], [64]) or spray pyrolysis ([35],[65]), generally requiring stages of drying and/or calcination (650-800 °C for 3-10 h).

The feasibility of reaching the “in-situ” doping of the spinel was already studied in [67] concerning the Cu-doping of the manganese cobalt spinel, by the electrophoretic co-deposition of $Mn_{1,5}Co_{1,5}O_4$ and CuO as copper precursor, obtaining good results.

1.2. Aim of the work

The aim of this work is twofold.

The first objective of this study was to investigate the possibility of achieving an "in-situ" Fe-doping of the spinel by electrophoretic co-deposition, using $Mn_{1,5}Co_{1,5}O_4$ and Fe_2O_3 as precursors. The proposed method would allow to obtain a doped spinel with reduction of production times and costs. compared to the techniques proposed so far,

The effect of different amounts of Fe doping and of the sintering process on the coating microstructure and morphology wilt be reviewed and discussed.

On the other hand, the effectiveness of both the undoped and the doped coatings will be evaluated on two types of ferritic stainless steels: the first one is the Crofer 22 APU, an expensive alloy specially developed for SOFC interconnects, whose performances have been studied in many researches; the other one is the AISI 441, a commercial steel, which is gaining interest because its use would lower the cost of the interconnect, but for which still few studies on the long-term behaviour have been conducted.

By studying the oxidation behaviour up to 2000 h aging and measuring the electrical performances up to 3200 h (both conduced at 750 °C), and supplying the results with the electron microscope investigation, two potential oxidation mechanisms will be proposed and the suitability of both the steels as interconnect materials and the spinels as protective coatings will be evaluated.

1.2.1. Thesis outline

The thesis is divided as follows.

In the next part of Chapter 1 the proprieties and the issues of the studied materials are presented. Then, a section is devoted to the theoretical and practical considerations about the methods exploited for the samples preparation (electrophoretic deposition and sintering) and characterization (high temperature oxidation and electrical conductivity).

In Chapter 2, the details concerning the experimental procedures here applied are described.

Results and discussion are therefore proposed in Chapter 3, sorted by type of characterization. The last section of the same chapter (3.4 Oxidation mechanisms) is dedicated to an overall explanation of the partially contrasting results and two oxidation mechanisms are suggested.

Finally, in Chapter 4 the conclusions of the study are briefly set out.

Figure 1.4 shows an overview of the work done for the thesis.

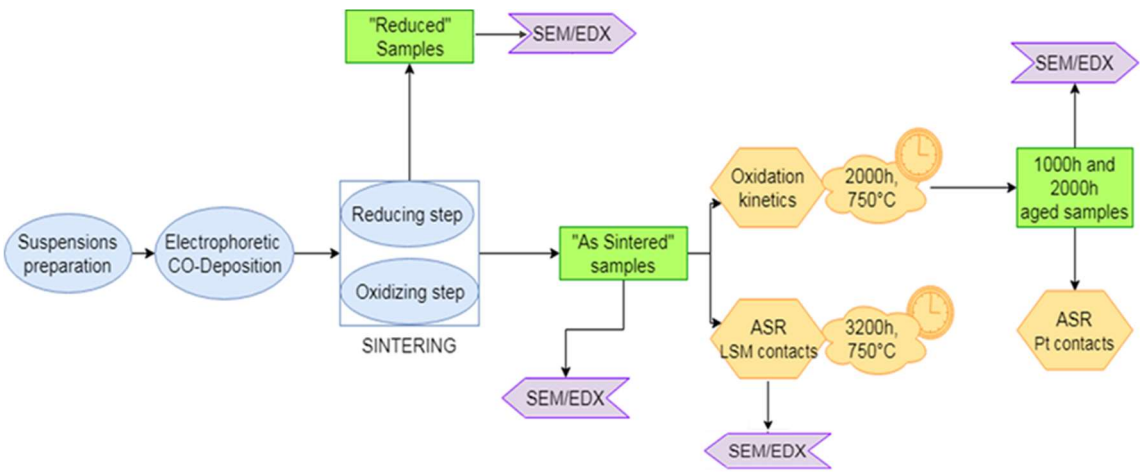

Figure 1.4: Thesis outline.

1.3. Materials

In this section, the main properties of both the coating and interconnect materials used for this work are presented discussed, with references to previous studies and results.

For this study the Mn-Co spinel powder (here named MCO) in the composition of $Mn_{1,5}Co_{1,5}O_4$ was used, both in its un-doped and Fe-doped forms: here, their properties are presented, with some connection with the Cu-doped MCO spinel as well.

Later, the features of the FSSs chosen as interconnects substrates are discussed: the Crofer 22 APU and AISI 441. While the use of the former as interconnect is already established and many studies have already been done, little research has been led on the second and the data on its long-term behaviour are still missing.

Finally, some issues related to the coating and steel jointing, concerning the oxidation behaviour and electrical stability of the system are pointed out.

1.3.1. Manganese cobalt spinel: structure, properties and doping possibilities

The basic spinel formula can be written as AB_2O_4; a spinel unit is made of 8 of this cells, forming a face centered cubic close packing of 32 oxygen anions, where 8/64 tetrahedral and 16/32 octahedral site are occupied by A and B metal cations [68].

A is a divalent cation (A^{II}) such as Mg, Cr, Mn, Fe, Co, Ni, Cu, Zn, Cd, Sn, whereas B is trivalent (B^{III}) cation (like Al, Ga, In, Ti, V, Cr, Mn, Fe, Fe, Co, Ni)

In the normal spinel structure, A is a divalent cation (such as Mg, Cr, Mn, Fe, Co, Ni, Cu, Zn, Cd, Sn), whereas B is a trivalent cation (like Al, Ga, In, Ti, V, Cr, Mn, Fe, Fe, Co, Ni); the divalent cations are positioned at the tetrahedral holes, while the trivalent ions at the octahedral ones, thus the formula of normal spinel can be written as $(A^{II})^{tetr}(B^{III})_2{}^{oct}O_4$ [69].

An example of it is $MgAl_2O_4$, illustrated in Figure 1.5.

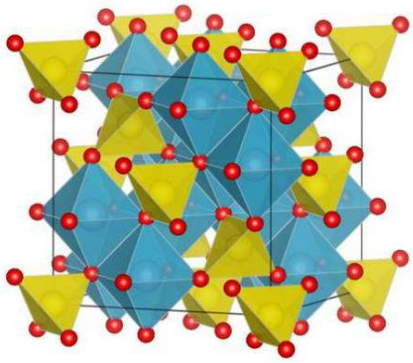

Figure 1.5: Normal spinel structure of $MgAl_2O_4$. Image generated by the VESTA (Visualisation for Electronic and STructual analysis) software from [70].

In a spinel different element can be at both the divalent and trivalent state, and therefore, both divalent and trivalent cations can occupy the tetrahedral or octahedral sites, depending on their relative amount and on the energy interactions between them [71].

Indeed, keeping in mind this possibility, the more rigorous formula about the cation distribution in the spinel structure would be $(D_{1-\delta}T_{\delta})[D_{\delta}T_{2-\delta}]O_4$, where D and T stay respectively for divalent and trivalent cations, δ is the degree of inversion, the round brackets () indicate the tetrahedral position and the squared brackets [] the octahedral ones [72].

When δ is 1, the inverse spinel structure is reached, characterized by having all the tetragonal sites occupied by trivalent ions, as expressed by the formula $(B^{III})^{tet}(A^{II}B^{III})^{oct}O_4$, an example of which is $CoFe_2O_4 = Fe^{III}(Co^{II}Fe^{III})O_4$ [73].

The importance of the cation distribution resides in the particular physical and chemical properties generated by their position in the crystalline structure, so that the magnetic and electric properties could vary even if the nominal composition of the spinel is the same [74]; this feature is of major interest concerning some new application of the spinels in magnetism, superconductivity and optics [17].

This changeable cation distribution is due to the existence of a preference in the occupation of tetrahedral or octahedral sites based on the number of electrons in the d orbital of the metallic cations involved [68], since that defines the energetic state of the ion and, together with its oxidation state the ionic radius of the element.

Considering that in the cubic close-packed structures, the tetrahedral sites are smaller than the octahedral ones (0,225 against 0,414 radius [75]), when varying the relative fractions of the different metals, the normal spinel structure results as being distorted.

In this regard, the phase diagram [76] in Figure 1.6 shows that the $(MnCo)_3O_4$ spinel crystalizes in the cubic or tetragonal phase, depending on the relative fraction of the two metallic elements.

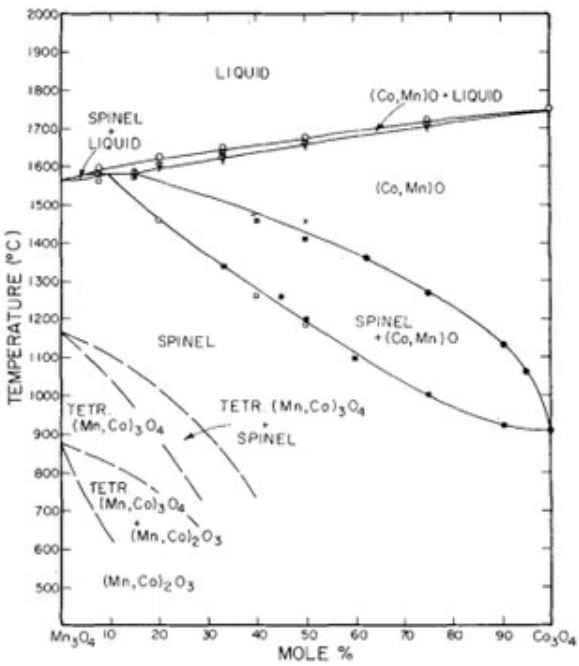

Figure 1.6: Phase diagram of Mn_3O_4-Co_3O_4 by [76].

The Co_3O_4 is a normal spinel with the structure $(Co^{2+})^{tetr}[Co^{3+}]_2{}^{oct}O^{2-}{}_4$.

When Mn is added to the system, it has been reported that the substitution of Co by it takes place in the octahedral sites, thus forming $(Co^{2+})[Co^{3+}{}_{2-x}\ Mn^{3+}{}_x]O^{2-}{}_4$. Indeed, the cation distribution of the $MnCo_2O_4$ (x=1) was seen to follow this trend ([77], [78])

By Mn insertion, lattice distortions and redox reactions among Co and Mn (Co^{3+} and Mn^{3+} → Co^{2+} and Mn^{4+}) can occurred, bringing benefits to the electrical conductivity [79].

At x=2, the complete inversion of the structure takes place forming Mn_2CoO_4, (with Mn^{3+} in octahedral and tetrahedral holes and Co^{2+} in tetrahedral sites), which is stable in the tetragonal phase ([80], [38]).

Anyway, the definition of the cation distribution in the spinel structure is a controversial topic, since it is largely influenced by preparation conditions (mainly temperature, pressure and time), that could cause oxygen excess, cation deficiencies as well as other crystal defects [17].

Concerning the influence of temperature, it was reported that at room temperature the $(MnCo)_3O_4$ spinel is a mixture of cubic ($MnCo_2O_4$) and tetragonal (Mn_2CoO_4) phase ([33], [68]), and that it develops into the single cubic phase at ca. 400 °C ([36], [38]), where still more Mn cation occupy the octahedral sites and Co the tetrahedral ones [37].

Therefore, the $Mn_{1,5}Co_{1,5}O_4$ spinel used in this work, can be considered as a 50:50 mixture of tetragonal Mn_2CoO_4 and cubic $MnCo_2O_4$ at room temperature, entirely reaching the cubic phase above 400 °C.

The cation distribution remains a relevant issue when focusing on the electrical conductivity of the spinel and the possible effects of doping by other metal cations.

With respect to the first, it has been accepted that the conduction is due to the small polaron mechanism, created by interactions of electrons and electron holes with the spinel lattice; since it is a thermally activated process, the spinels can be considered semiconductors, with lower resistance while increasing the temperature [81].

Thus, the law explaining this kind of conductivity is expressed by [82]:

$$\sigma = \frac{\sigma_0}{T} e^{(\frac{-E_A}{k_b T})}$$

Where σ in the electrical conductivity [Scm^{-1}], σ_0 is the pre-exponential factor, E_a is the activation energy, k_b is the Boltzmann's constant and T is the temperature [K]. Since σ should be linear with the temperature, E_A can be calculated from the slope of the straight line.

Many authors agreed on the major contribution of cations in octahedral sites to the conduction, because of their shorter distance between each other compared to those in the tetrahedral holes ([17], [37], [66]), thus, since that position in mainly occupied by Mn cations, thanks to the hopping between Mn^{2+} and Mn^{4+}.

Anyway, since the determination of the cation distribution is really complex (mainly achieved by neutron diffraction data [37]), the electrical conductivity is generally measured on sintered pellets at the desired temperature (in most cases 800 °C), but also in this way, the interpretation of the data is controversial because of their high degree of dispersion.

As reviewed in [17], the conductivity measured for $MnCo_2O_4$ vary from 34 to 90 Scm^{-1}, underlining how the production and sintering method can influence the final value. For examples, in [83], the $MnCo_2O_4$ was measured to be 60 Scm^{-1}, while in [33] 75 Scm^{-1} (both at 800 °C).

The data are scattered also about the $Mn_{1,5}Co_{1,5}O_4$, registering lower values compared to the Co richer spinel ([33], [36]), someone slightly higher [38], but mostly around 50-60 Scm^{-1} (at 800 °C).

In order to verify the effect of the doping on the cation distribution and on conductivity, the researches mostly report on the shift their peaks in the XRD patters and on the gravimetry analysis.

Both [17], [66] and [84] found out that, while added to the spinel, both Fe and Cu preferentially occupy the octahedral site (substituting Mn cations), with opposite effect.

Copper causes a reduction in the lattice parameter of the spinel structure, thus bringing the octahedral sites closer and easing the polaron hopping; the possibility of the participation of Cu^{2+} cations to the conduction is considered. This proves the better conducting behaviour of the Cu-doped coating than the undoped $Mn_{1,5}Co_{1,5}O_4$ already recorded in [67].

By contrast, iron produces an increase of the lattice parameter, that, together with the impossibility of Fe^{3+} cation to participate to the polaron hopping, causes a decrease in conductivity.

In Figure 1.7 the data measured in [17] are reported.

Comp.	E_A [eV]	σ_0	σ (800 °C) [S/cm]
MC	0.53	17.2	89
Cu1	0.50	17.1	114
Cu3	0.44	16.7	142
Cu5	0.41	16.5	168
Fe1	0.53	17.1	77
Fe3	0.53	16.5	47
Fe5	0.53	16.2	31

Figure 1.7: Activation energy, pre-exponential factor and electrical conductivity for undoped $MnCo_2O_4$ (MC) and Cu e Fe doped at different levels (1=0,1; 3=0,3; 5=0,5) measured in [17].

Furthermore, the Cu doping lead also to a decrease of the activation energy, while the Fe-doped spinel showed the same as the undoped MCO.

Considering that, the Mn-Co spinel is in direct contact with the chromia scale, the effects related to the Cr doping have been studied as well.

In this regard, it has been reported that, like Cu and Fe, also Cr preferably takes up the octahedral holes of Mn-Co spinel structure [68], and, since its only possible oxidation state is 3+, its presence drastically reduces the number of available hopping sites [37]. In some way, chromium is acting very similarly to iron as far as the cation distribution is concerned; indeed, Cr as well makes the $(MnCo)_3O_4$ lattice parameter to increase, which is further stretched in the Mn-Co-Cr-Fe spinel [85].

In Figure 1.8 the conductivities of some Cr containing spinels are reported, as reviewed in [17].

Composition	σ(800 °C) [S/cm]	Sintering temp. [°C]	E_A [eV]	Measurement range [°C]
$MnCrFeO_4$	0.3	1250-1550	0.45	227-1027
$MnCoCrO_4$	2.5	1200	0.57	500-900
$Mn_{0.75}Co_{0.75}Cr_{1.5}O_4$	0.45	1200	0.75	500-900
$Mn_{0.5}Co_{0.5}Cr_2O_4$	0.006	1200	1.0	500-900
$MnCr_2O_4$	0.004	1550	1.02	600-1000
$MnCr_2O_4$	0.03	1250-1550	0.89	227-1027
$Mn_{1.7}Cr_{1.3}O_4$	0.14	1550	0.95	600-1000

Figure 1.8: Conductivity, sintering temperature, and activation energy for the conduction of some Mn-Co-Cr-Fe containing spinel, adapted from [17].

Concerning the thermal expansion coefficients, the literature reports results varying in a wide range, so that no clear relationship between the CTE and metallic element doping can be asserted at this point [66].

About the undoped $(MnCo)_3O_4$, [33] reports 13,5 and 9,7 $10^{-6}K^{-1}$ respectively for $MnCo_2O_4$ and $Mn_{1,5}Co_{1,5}O_4$, whereas, for the second one, the CTE measured in [63] was 11,66 $10^{-6}K^{-1}$ and in [37] 10,7 $10^{-6}K^{-1}$, thus generally suggesting a CTE reduction while decreasing the relative amount of Co.

Concerning the Fe addition, in [17] it was recorded a reduction of the CTE for the Fe doped: indeed it shifted from 15,3 $10^{-6}K^{-1}$ of $MnCo_2O_4$ to 14,8, 12,8, 11,2 $10^{-6}K^{-1}$ (from 400 to 800 °C) with increasing levels of iron doping. On the contrary, the Cu doping caused an increasing of it.

The same trend was found in [66]. In [83] it is stated that the Fe containing spinels, showing a TEC in the range of 11-12 $10^{-6}K^{-1}$, have a better match with the steel of the interconnect.

Also the Cr doped $MnCo_2O_4$ exhibit a lower CTE, till reaching the value of $7\times10^{-6}K^{-1}$ [83].

It must be highlighted that the importance of the thermal expansion coefficient is maximum for the switching on and off of the device, and that, as previously stated, the CTE must be close to $10\times10^{-6}K^{-1}$ [22].

1.3.2. Ferritic stainless steels: Crofer 22 APU and AISI 441

The main characteristic of the stainless steels is that they contain chromium as alloying element, which allows the formation on the steel surface of a thin passivating layer of Cr_2O_3, which results more protective toward corrosion while increasing the Cr concentration in the alloy itself.

Compared to the martensitic ones, the ferritic stainless steels contain less carbon (<0,12% compared to 1,2% of the martensitic ones), which brings to lower mechanical properties (strength, hardness), but high corrosion resistance, ensured by a Cr amount typically between 12 and 27% [86]; by contrast, the austenitic stainless steels are characterised by better corrosion resistance together with high weldability and workability, thanks to the Ni addition (up to 35%) which causes a remarkable price increase [87]. Moreover, the austenitic stainless steels have a CTE around $18 \times 10^{-6}K^{-1}$ [88], which is too much for SOFC applications; on the other hand, the FSSs possess a CTE in the range of $11\text{-}13x10^{-6}\,K^{-1}$ [89], closer to the ones of the SOFC unit cell materials (ca. $10x10^{-6}\,K^{-1}$).

Ti, Nb and Zr are used as alloying elements for the FSS to stabilize the ferritic structure and block the formation of chromium carbides, thus limiting the Cr depletion from the alloy; Mo and W are sometimes added to improve the corrosion resistance.

One of the issues related to the use FSS at high temperature is the grain growth, critical from 850 °C, but that can be controlled by larger addition of Cr to the alloy (e.g. the AISI 446 FSS contains 26% of it and can resist up till 1150 °C [86]).

concerning the application for SOFC, the selected FSSs have at least 20% of Chromium [23], but not sufficient to ensure acceptable properties as interconnect material. Two major issues have to be addressed.

The former is the great Cr evaporation at high temperature, which is partially reduced by adding about 0,3-0,5 wt.% of Mn as alloying element: this element is able to form a well adherent Cr-Mn spinel ($MnCr_2O_4$) [90] next to the Cr_2O_3 scale [57] and it has been proven to reduce the Cr evaporation by 60-70% [27]. However, this reduction is still not sufficient to avoid the use of the coating on the steel ([91], [92]).

The second one is the presence of residual silicon as alloy impurity. During performance at high temperature, it can indeed migrate by boundary or bulk diffusion (depending on the operating temperature [12]) toward the steel/oxide scale interface. If its concentration is high enough, Si can there form a continuous silica layer which is not only electrically insulating (the resistivity is the range of $10^{15}\text{-}10^{17}$ Ωcm [93]), but which also exhibit an unsuitable CTE (reported at $0,5x10^{-6}K^{-1}$ in the amorphous state [15] and between 2,9 and $5,8x10^{-6}K^{-1}$ ([94], [95]) if crystalline), thus harming both the conductivity of the interconnect and the adhesion of the Cr_2O_3 scale and the coating.

In an attempt to solve the silica layer issue, two families of FSSs were developed specifically as SOFC interconnects materials.

I. Low Si steels, obtained by expensive vacuum melting processes. Crofer 22 APU (ThyssenKrupp VDM), ZMG232 G10 (Hitachi Metals) belong to this category; they represent the first steels developed for SOFC interconnects and are still the most used ones.
II. Steel with higher silicon concentration and alloyed with Nb, such as Crofer 22 H (ThyssenKrupp VDM), Sanergy HT (Sandvik Materials Technology), which are subjected to more traditional and cheaper production methods.
Nb is indeed supposed to tie up the silicon, while forming Fe_2Nb, known as Laves phase.

Concerning this last point, it is however necessary to point out that the mechanism by which the Nb acts and its effectiveness are still discussed.

Indeed, the Laves phases are reported to place mainly at the grain boundaries [96], and that the Si has some preference for it, thus reducing its grain boundary diffusion and avoiding the formation of the silica layer [97].

Nevertheless, in [12] the partial ineffectiveness of Nb as blocking agent is pointed out, explaining that at high temperature, not only the grain boundary diffusion but also bulk diffusion is playing an important

role. Moreover, it was there found that, if the Fe_2Nb quantity is not enough to bind all the oxygen vacancies at the boundaries, its effect is actually to increase the grain boundary area itself, thus enhancing the Si diffusion.

In Table 1.1, the typical compositions (wt.%) of the mentioned alloys are reported. RE stands for reactive elements.

Table 1.1: Manufacturer supplied compositions of some FSSs designed for SOFC interconnects, as reported in [98].

Steel	Cr	Mn	Si	Mo/W	Nb	Cu	RE	Fe
Crofer 22 APU	22,7	0,48	0,02	-	-	-	0,09La	Bal
ZMG232 G10	23,7	0,28	0,02	1,4W	-	0,93	0,07La/0,28Zr	Bal
Crofer 22 H	22,7	0,42	0,2	1,4W	0,55	-	0,08La	Bal
Sanergy HT	21,2	0,3	0,12	0,96Mo	0,71	-	0,24Zr	Bal

As shown in Table 1.1, in all the discussed steels, some small amount of rare earths, mainly La and Zr, but also Ce and Y, are added: even if the mechanism of their action was not clarified [99], it seems that the addition of this high mass element can modify the oxygen vacancies diffusion, with the effect of improving both the oxidation and the adherence of the oxide scale ([100], [101]).

Since the discussed FSSs are not rid of troubles and the use of a coating is anyhow necessary, some cheaper commercial Fe-Cr alloys suitable for high temperature application have gained attention, as well. Their compositions are given in Table 1.2.

Table 1.2: Compositions of some commercial FSSs evaluated as SOFC interconnects material.

Steel	Ref.	Cr	Mn	Si	Ni	Nb	Al	Ti	Fe
AISI 441	[102]	17,6	0,33	0,47	0,20	0,46	0,045	0,18	Bal
AISI 430	[103]	17,4	0,92	0,85	-	-	-	-	Bal
AISI 439	[104]	17,01	0,18	0,42	0,23	0,17	-	0,15	Bal
AISI 405	[105]	13,9	0,4	0,44	0,24	-	0,25	-	Bal

These steels are advantageous from an economic point of view because, in addition to having greater tolerance on the silicon limit (also compared to the second steels category shown in Table 1.1), they are not alloyed by rare earths and present significantly lower chromium content.

Ti is also added because it is supposed to strengthening the surface of the steel while oxidizing to TiO_2, which is supposed to reduce the wrinkling related to thermal cycling [23].

In conclusion, it is highlighted that the two FSSs studied in this work belong to the two opposed categories previously regarded. While they both contains Mn, they differ mainly for the following points:

- **Crofer 22 APU**: higher Cr amount, alloyed by La.
- **AISI 441**: lower Cr amount, significant Si presence, alloyed by Nb, Ti.

1.3.1. FSS and MCO at high temperature: critical issues

After having discussed the properties of the coating and interconnect materials, it is important to focus on which kind of interaction can occur between them, while in contact and maintained at the SOFC operating temperature for a long time (ideally >40000 h).

Indeed, as it is discussed more in details in Section 3.4, when kept at high temperature, the involved materials are less stable, the diffusivity (which follows the Arrhenius law) of each element is facilitated and the overall reactivity is enhanced.

In this context, the first step is the progressive growth of the Cr_2O_3 scale at the top of the steel, which brings to the Cr depletion of the interconnects, reducing its corrosion resistance, till reaching the breakaway oxidation.

Moreover, the mismatch in the CTE between chromia (9,6 $x10^{-6}$ K^{-1} [15]) and the steel (for Crofer 22 APU it is approximately 12,37$x10^{-6}$ K^{-1} [63]), with thermal cycling causes mechanical stresses at the interface with the possibility of spallation.

The time needed to reach the breakaway oxidation and the spallation of the oxide scale is considered as determining the lifetime of the interconnect itself [17].

The growth of the oxide layer is crucial also concerning the electrical properties, first of all because its conductivity (1-8 $x10^{-2}$ Scm^{-1}, at 800 °C [17]) is much lower than that of the steel itself (ca. 90 $x10^{-2}$ Scm^{-1} [106]) .

Furthermore, while at temperature above 1000° C, Cr_2O_3 is an n-type intrinsic semiconductor ruled by electronic defects, below 1000 °C it is an extrinsic p-type semiconductor, which conductivity is dominated by the presence of crystal defects, impurities (i.e. doping elements) and the oxygen partial pressure [23]: this means that the alloying elements of the steel, mainly Mn, Ti, but also RE, Nb, Si, as well as Fe itself, migrating through the chromium oxide, can have a great impact on its properties (Figure 1.9).

it is reported that titanium has a good miscibility with Cr_2O_3: between 400 and 1000 °C Ti doped chromia in a n-type semiconductor at low p_{O2} and a p-type at near atmospheric pressure [23]). On the contrary, as already assessed in 1.3.2 Si tends to gather under the oxide scale.

Many studies have already proven that Mn during high temperature oxidation of FSS can form both $(Mn,Cr)_3O_4$ nodules at the steel/oxide scale interface ([90], [107], [108]) favoured by thermodynamics, but it can also migrate through the oxide scale and deposits in the outer part of it, forming there the Mn-Cr spinel ([12], [98], [108] [109], [110]). The effect of those mixed spinel layers/areas is not clear, because, on the one hand they could weaken the interfaces due to CTE mismatch, on the other they can influence the cation diffusion during oxidation.

However, even if no explicit results concerning the Cr retention of the $(Mn,Cr)_3O_4$ [27] are available, when a coating is not applied on the steel, among all the mentioned factors, the outward chromium diffusion is still the dominating process [23].

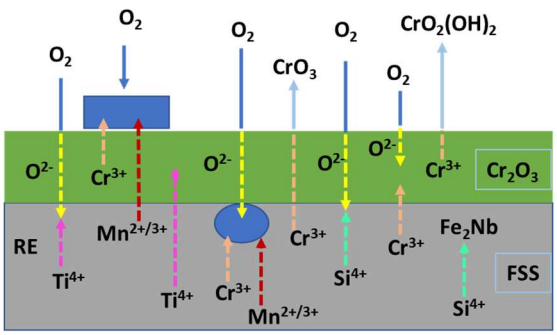

Figure 1.9: High temperature reactions between the FSS and the oxide scale.

When the MCO coating is deposited over the steel, both the thermodynamic and kinetics parameters are in some way modified, since the concentration gradients of each element, as well as the oxygen partial pressure on the scale change.

To this purpose, when a very dense coating is deposited, less oxygen is able to reach the inner oxide scale; the morphology of the porosity (open/close) and the coating thickness (longer migration path) have some influence (see Figure 1.10).

In [35] the authors investigated the effect of the porosity in terms of oxide scale thickness and Cr evaporation, finding out that, while the oxidation rate with the dense coating was four times lower compared to the porous one, the difference in Cr evaporation between the two studied cases was not so relevant. Then, both in [65] and [67], it is verified that the Cu-doped MCO on Crofer 22 APU, although promoting the densification, provides the least protection against oxidation compared to more porous coatings.

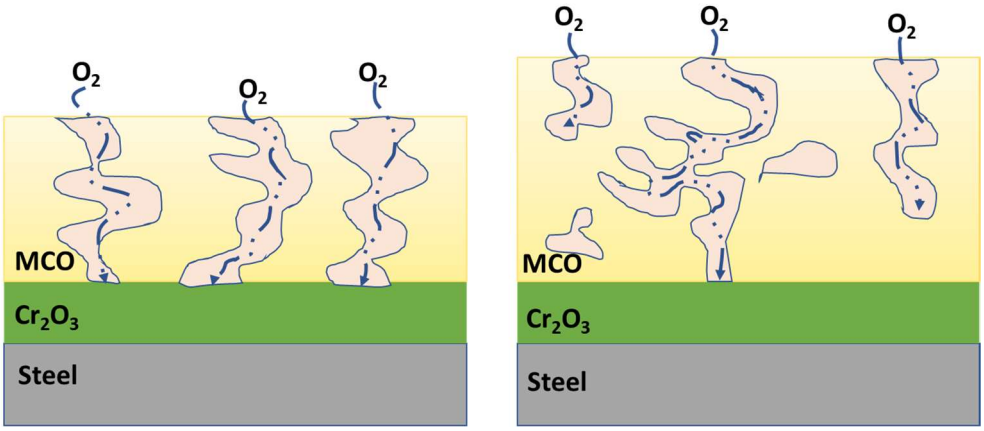

Figure 1.10: Schematization of the possible coating and porosity morphology effects.

The previous considerations suggest that, in addition to the morphology of the coating, there are more intrinsic reasons about the protective effect of the coating.

In this regard, many studies report the major influence of the reactions occurring over time at high temperature between the MCO coating and the chromia scale, bringing to the formation of the so-called reaction layer (RL), obtained by the interfusion of Mn and Co toward the Cr_2O_3 scale and of Cr toward the MCO coating ([37], [58]),

The RL is supposed to reduce both the chromium and the oxygen diffusion, indeed, some authors confirmed that the positive effect of the MCO coating on the reduction of steel oxidation and Cr vaporization actually relies on it ([65], [111]).

However, the long term consequences of the RL growth have not been clarified yet [17], mainly because of two issues.

It is indeed reported that the CTE of the RL decreases with increasing the Cr amount in it, therefore leading to the potential interface cracking and the spallation of the coating [37].

Then, as already discussed in 1.3.1, the conductivity of Cr containing spinels is considerably lower than that of the MCO spinel, i.e. the progressive RL thickening can affect the electric performance of the overall interconnect [112].

From this point of view, the potential effect of the MCO doping by transition metal have not been deeply studied yet.

In Figure 1.11 a schematization of the discussed points is presented.

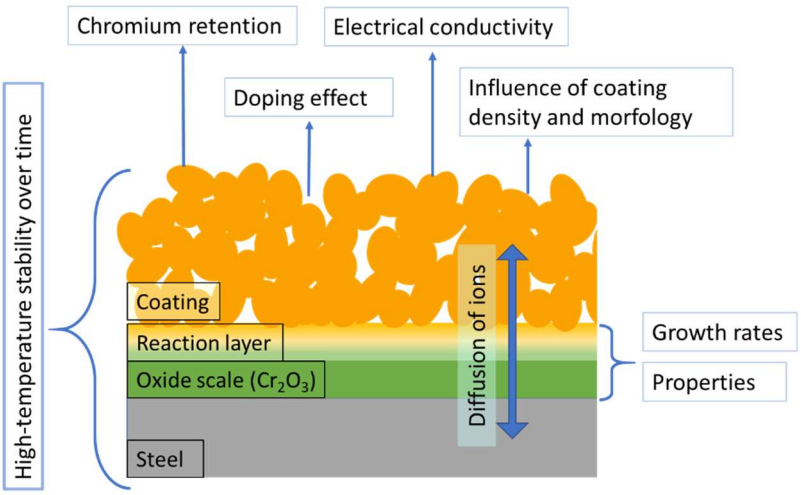

Figure 1.11: Schematization of the issues occurring during interaction between FSS and MCO coating at high temperature.

1.4. Theory and methods

In this section the methods by which the samples were prepared (EPD and sintering) and characterized (oxidation resistance, electrical conductivity) are discussed, with some references to the theories behind them.

1.4.1. Electrophoretic deposition

The electrophoretic deposition (EPD) is a synthesis process that involves the movement and the deposition of charged particles suspended in a liquid solution when an electric field is applied to the system.

The underlying principle on which EPD was first studied by Hamaker [113]: it is based is the ability of solid surfaces to acquire a surface charge, and thus a surface potential energy, when dispersed in a liquid. The effect is maximum for colloidal particles (defined by Levine as having a diameter between 1 and 1000 nm [114]) for which the ratio of surface area and volume is ultimate.

After that, this mechanism has been widely examined and many theories and models were proposed; as discussed in [115], the developing of the electric charge is due to reactions occurring between the atoms and groups on the particles surfaces and the atoms/ions in the liquid, which depends, of course, on the nature on both the solid and the liquid fraction in the suspensions.

The case of greater interest here is that of inorganic oxides (but which can also be applied to polymers and to organic molecules such as proteins): these substances contains on the surface some hydroxyl groups that can dissociate depending on the pH of the solution in which the particles are dipped [116], as shown in the following:

1) High pH, basic solution: -M-OH + OH- ⇆ -M-O- + H2O, negatively charged surface
2) Low pH, acid solution: -M-OH + H+ ⇆ -M-OH_2+, positively charged surface

Therefore, it is possible to plot a graph relating the dependence of the surface charge of the suspended particle, as a function of the pH of the solution (Figure 1.12): the point where the curve crosses the x-

asses is called Zero Charge Point and identifies the value of pH so that the particle does not have any kind of electrical charge on the surface.

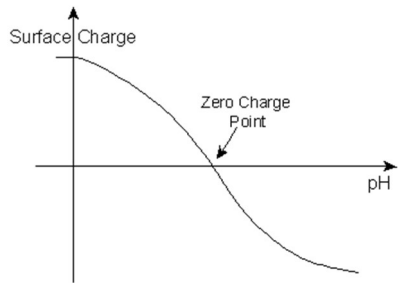

Figure 1.12: Dependence of the surface charge on the suspension pH.

Once the surface charge is established, it will influence he distribution of the ions in the liquid around the particle, leading to the formation of the so called electrical double layer (Figure 1.13), first studied by Helmholtz, Gouy and Chapman and then improved by Stern and Grahame.

As shown in Figure 1.13, the ions of the opposite electrical charge, compared to the one of the particle surface, surround it forming a layer of counter-ions; this first layer (called Stern Layer) is then followed by broader one, called Diffuse Layer, where ions of both charges alternate. The nature and the thickness of the electrical double layer (EDL) rely respectively on the established Van der Waals and electrostatic forces [117].

Since particles of opposite charges repel each other, it is easy to understand how much the stability of these two layers of charges is revealing for that of the overall EPD system [116].

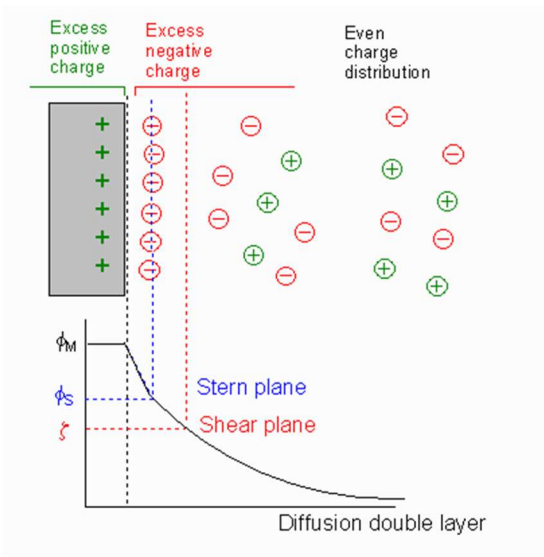

Figure 1.13: Schematization of the electrical double layer.

Given the presence of this charge excess, it is possible to define a potential φ, which is maximum on the surface and tends to zero after the EDL; from an experimental point of view, what is more relevant about this potential is its value at the shear plane (Figure 1.13) between the Stern and diffusion layer: it is defined as Z Potential (ζ) and it is among the mayor parameters affecting the movement of the particles during the EPD process.

Figure 1.14 outlines the EPD principle and highlights some of its characteristics. The set-up is itself quite simple: as already said, the key roles are played by the presence of charged particles surrounded by the EDL and dipped in a solution, so that they reach a stable suspension.

For achieving a deposition, (at least) two electrodes are necessary: when an electric field is applied between them, the particles can move towards the opposite charge electrode.

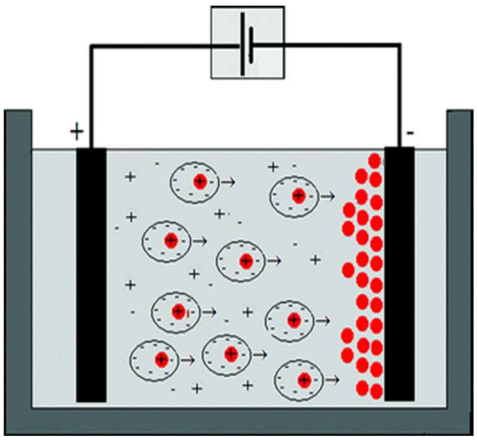

Figure 1.14: Outline of the EPD set-up [118]

Despite the effort from the theoretical point of view, the mechanisms that govern the EPD have not yet been clarified till now [119]; one of the main issues is to understand how the deposition can practically happen and bring to the makeup of a dense and adherent layer on the substrate.

Figure 1.15 offers a schematic representation of the model proposed by Sarkar and Nicholson: when an electrical potential is applied, the EDL of each particle is distorted, becoming thinner toward the opposite charge electrode and thicker on the other side (a); the thinning is even more substantial when the particle is close to the electrode (b), so that, when another particle is approaching, it can penetrate the EDL, thanks to the coulombic attraction and the particles can coagulate (c).

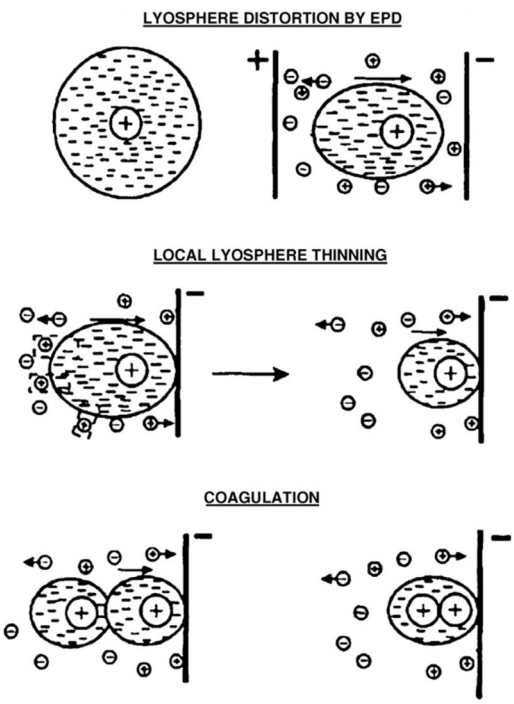

Figure 1.15: EPD sedimentation mechanism [120].

However, apart from the microscopical interpretation of the phenomenon, the factors that rule the process and that have necessarily to be considered during an EPD can be divided between those related to the suspension properties and those to the overall process ([115], [117]).

Starting from the former, one can highlight:

- **Particles size**: although it is not possible to set a defined size limit, a maximum diameter of 20 μm has been fixed in some studies [121]. Bigger particles are indeed more influenced by the gravity and tend easily to sediment when a very high value of surface charged is not reached, and, in any case, to get a homogeneous layer is trickier.
- **Concentration of the solid fraction in the suspension**: it plays a key role especially for co-depositions. Indeed, when more than one powered is involved in the EPD, they can deposit at different rates, thus following their electrophoretic mobility. In this case, the suspension concentration should be high enough so that every colloidal species deposit while transported by the overall flow.
- **Liquid medium**: some researches have been carried out in order to define the influence of the dielectric constant, viscosity and conductivity of the liquid fraction. Generally, organic mediums are preferred, because thanks to their low dielectric constant, the number of free ions in the suspension is low, so that they do not interfere the movement of the particles. Water, besides having an high dielectric constant, can dissociate at the electrodes, forming bubbles that can affect the deposition density, especially when the deposition rate is high [122].
- **Z potential**: it is without doubts the key factor for EPD because it defines the direction of the migration of the particles, the stability of the suspension and the density on the deposited layer. When ζ is high, the suspension results in being stable due to particles repulsion; however, a too strong potential will prevent them to coagulate. On the other hand, if ζ is too low, the particles will coagulate before the deposition, bringing to their precipitation and/or to a porous deposit.
  As already said, the value of the surface potential is mainly due to the interaction between the solid fraction and the liquid one, on the basis of the pH of the solution; thus, the Z Potential could be modified by choosing a different solvent, by adding acids, basis or other additives.

Regarding the characteristics of the process, it is mainly influenced by the following:

- **The applied voltage**: it is necessary to balance it to avoid both the turbulence (if too high) and the absence of the deposition (if too low);
- **The deposition time**;
- **The distance between the electrodes**.

Although some mathematical expression to control the deposition parameters have been proposed ([123], [120]), a model that relates all the points listed is still not available; for this reason, by now a trial-and-error approach is generally pursued when a new EPD suspension must be optimized.

Despite this lack, EPD technique offers many advantages [19]:

- Simple setup
- Rapidity
- Flexibility regarding the modification of the deposition parameters
- Versatility for both the substrate shape and material and the particles size and composition
- Easy control of the coating thickness and morphology
- Low cost

For all these reason the EPD can be considered a suitable technique for the industrial production of advanced ceramic, such as many other materials [124].

1.4.2. Sintering

After being deposited, the ceramic coatings need to be sintered, and this is not a trouble-free passage: it requires high temperatures applied for some hours in air or in an atmosphere.

In this regard, two routes can be chosen: a single-step sinter or a two-step one.

The first option is in one heat treatment in air at a temperature typically between 900 - 1100 °C, for a time long enough to achieve the solid-state reaction among the deposited spinel particles.

The second procedure consists on a first heat treatment in reducing atmosphere (N_2/H_2 or H_2/Ar) followed by a second one in air. During the first step, the MCO particles decompose to metallic Co and MnO, whereas during the second one the spinel phase is formed again [125].

Many studies have been carried out to define the best conditions for the MCO coating sintering

For example, in Figure 1.16, the cross sections of an MCO coating obtained by EPD are shown after the single-step sinter only in air, at three different temperatures by Bobruk et al. [50]: at 1100 °C high densification is reached, nevertheless together with cracks between the MCO, the thick oxide scale and the steel; on the contrary, both at 900 °C and 1000 °C the coating presents still open pores and little densification occurred.

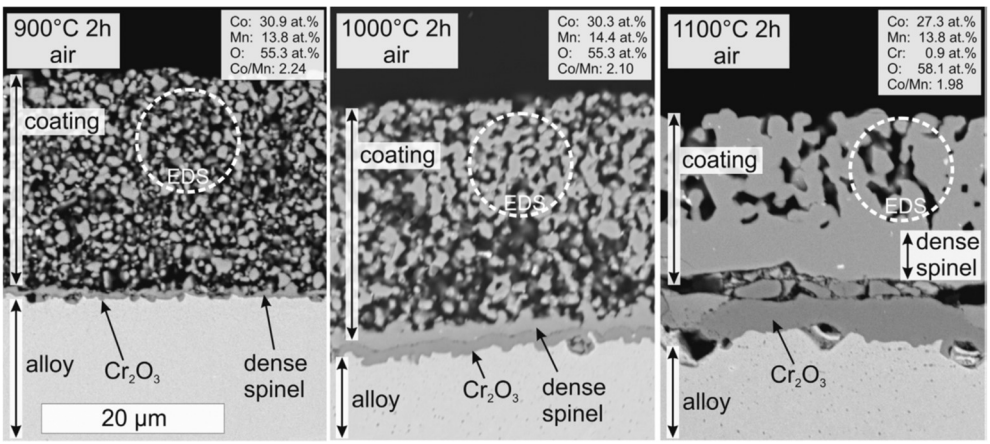

Figure 1.16: Cross section SEM image of MCO EPD coating on Crofer 22 APU, sintered by a single-step heat treatment in air at a) 900 °C b) at 1000 °C and c) at 1100 °C, from [50].

In [47] it is pointed out that, thanks to the reducing step, the MCO coating resulted in being much more dense and protective towards the interconnect oxidation, concluding that the higher cost due the addition of this heat treatment is legitimates by the better performances of the coating.

In [50] it was found that this densification effects at the end of the sinter is caused by the coarsening of the metallic Co particles during the reducing step, identifying the reduction at 1000°C in H_2/Ar and the re-oxidation at 900 °C (both for 2 h) as the best sintering option for the MCO sintering.

Moreover, while in [50] no reaction at the steel/coating interface after the reduction was recorded, in [125], already after the first heat treatment conduced at 850° C for 4 h in most H_2 atmosphere, a Fe- rich layer of $MnCr_2O_4$ was detected between the chromia scale and the reduced spinel, imputable to the iron diffusion caused by the long stay at high temperature.

Thus, many authors concluded that the two step route seems to be the most promising one ([48], [35], [66]), because on the one hand the coarsening of the metallic Co was proven to have a strong influence on the final coating density [50], on the other, the first heat treatment in reducing atmosphere is more protective for the steel, which forms a much thinner oxide scale, thus advantageous for the electrical conductivity [52].

Considering what discussed, in this work a reduction followed by a re-oxidation approach was chosen.

1.4.3. High temperature oxidation

Unless otherwise noted, the theory of this section was taken from the book *High temperature oxidation and corrosion of metals* by D.J. Young [126].

When a metal comes in contact with oxygen, the general reaction that can occur between them is:

$$\frac{x}{y}M_{(s)} + \frac{1}{2}O_{2(g)} \rightarrow \frac{1}{y}M_xO_{y\,(s)}$$

This reaction of the oxide formation is spontaneous only if the change in the Gibbs energy is less than zero, which depends on the temperature, the partial pressure of gasses and the activity of the solids involved in it.

Practically, to verify the thermodynamic possibility for the oxidation (or reduction) of a metal, one can make use of the Ellingham-Richardson diagram [127], reported in Figure 1.17.

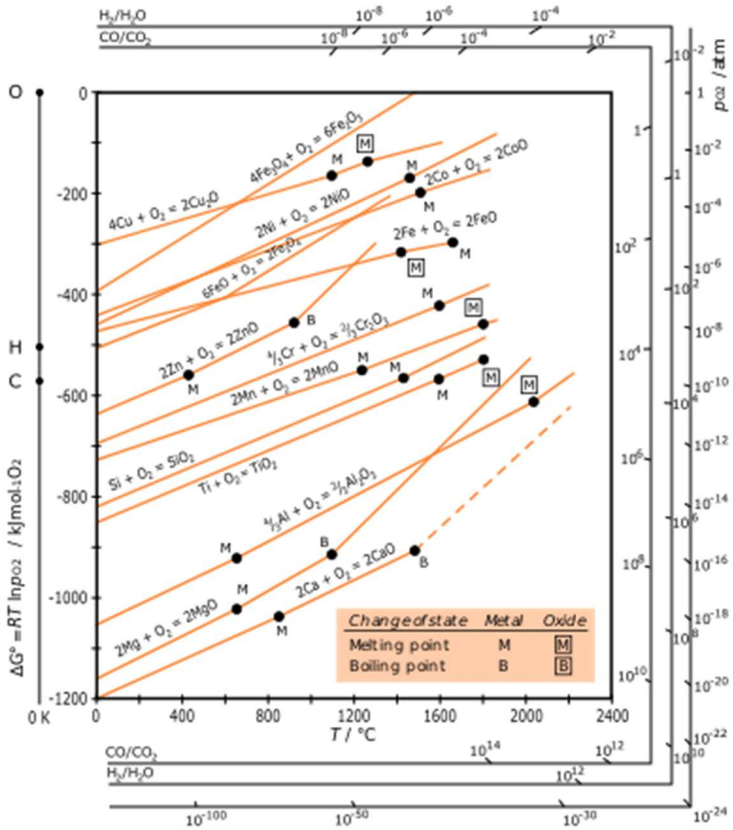

Figure 1.17: Ellingam-Richardson diagram for some metal-oxide reactions [128].

Apart from the thermodynamics point of view, while investigating the long-term behaviour of an interconnects, what is important to consider is the kinetics of the oxide scale formation. Indeed, as underlined in [17], the oxidation reaction is actually made of at least three steps, i.e. oxygen adsorption, oxide nucleation and oxide scale growth: the last one is much slower, therefore it is the rate limiting step for the oxidation.

The general way to express the oxide growth from a kinetic point of view is:

$$\frac{d\xi}{dt} = f(t)$$

where ξ is a measure of the extent of the reaction, t is the time and $f(t)$ is the function that explains the time-dependency of ξ.

In theory, ξ can be replaced by the moles consumption during the reaction of both the metal and oxygen; experimentally, there are two ways for that.

One possibility could be to determine the oxidation kinetics measuring the oxide scale thickness over time (e.g. by microscopy) and replace it to the ξ in the formula; however, this would be too wasteful.

An easier way to do that, is to measure the mass gain over time, which is related to the oxygen uptake due to metal cations oxidation [99]. This assumption can be considered valid only if no other processes that cause a change in weight, such as evaporation or spallation, occur.

Experimentally, measuring the weight of the samples at defined time intervals and plotting the data, different kinds of kinetics can be found, e.g. linear, parabolic, cubic, logarithmic.

The linear oxidation kinetics can be expressed by:

$$\frac{\Delta m}{A} = k_{l,m} \cdot t + C$$

Where, Δm is the mass change, A is the surface area, t is the time, $k_{l,m}$ [$gcm^{-2}s^{-1}$] is the linear oxidation rate in term of mass gain and C is the integration constant. The linear oxidation takes place when the grown oxide scale is porous and/or discontinuous (i.e. non protective) [17], as shown in Figure 1.18: in this case, the rate determining reactions are those at the gas/metal and gas/oxide interfaces.

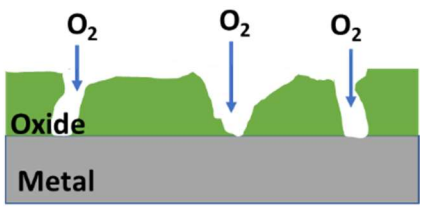

Figure 1.18: Schematization of a non-protective oxide scale.

On the other hand, the parabolic kinetic, is expressed by:

$$\left(\frac{\Delta m}{A}\right)^2 = 2k_{p,m} \cdot t + C$$

where $k_{p,m}$ [$g^2cm^{-4}s^{-1}$] is the parabolic oxidation rate in terms of mass gain, which better fits to the growing of a dense and continuous (i.e. protective) oxide scale. According to the law, when plotting the mass gain over time is parabolic unit, a straight line is obtained: the slope is actually the $k_{p,m}$[1].

In order to convert the oxidation rate in term of mass gain to the one related to the oxide scale thickness, the following equation needs to be applied:

$$k_{p,t} = k_{p,m} \left(\frac{V_{M_xO_y}}{16 \cdot y}\right)^2$$

where $k_{p,t}$ [cm^2s^{-1}] is the parabolic oxidation rate in terms of the oxide scale thickness, $V_{M_xO_y}$ is the molar volume of the oxide, y are the oxygen moles in the oxide

The $k_{p,t}$ can then be inserted to the parabolic kinetic law, in order to calculate the oxide scale thickness:

$$\frac{d\xi}{dt} = \frac{k_{p,\xi}}{\xi} \rightarrow \xi^2 = 2k_{p,\xi} \cdot t + C$$

[1] The convention is to consider the factor 2 as a part of the k_p.

where ξ can be substituted by both t for the thickness and m for the mass gain.

The parabolic oxidation was first described by Wagner [129], who identified the lattice diffusion of electrons and ions inside the oxide scale as the rate limiting process (Figure 1.19). This hypothesis is true if the thermodynamic equilibrium is reached at the interfaces (thus, not during the first oxide formation); the diffusion is then driven by the difference in the oxygen partial pressure among the outer interface and the inner one [17].

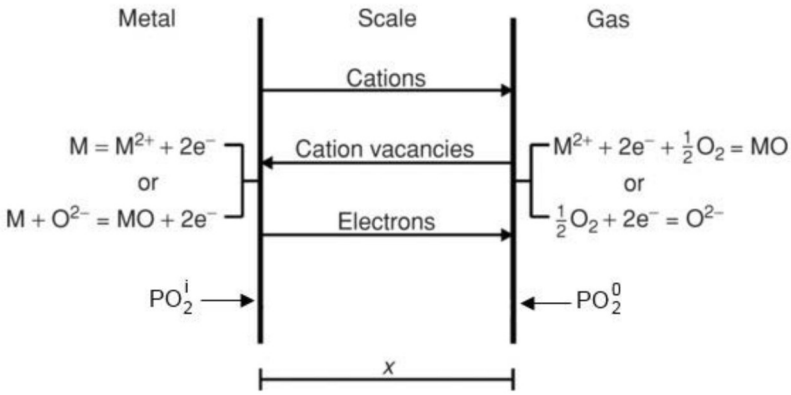

Figure 1.19: Schematization of the Wagner's diffusion model of parabolic oxidation [130].

At temperature above 700 °C, the FSSs oxidation has been proved to fairly fit the parabolic oxidation (see Figure 1.9 in 1.3.1), where the outward Cr diffusion, preferentially through grain boundaries, defects and microcracks, is generally considered the main rate determining diffusion mechanism [131].

A major drawback related to the evaluation of the oxidation by mass gain measurements is the Cr evaporation, that could modify the oxidation kinetics.

In this regard, in [91] the authors compared the mass gain and the Cr evaporation for Crofer 22 APU and Sanergy HT at different temperatures, finding out that at lower temperatures the relative effect of the chromium volatilization became more significant and that the higher Mn concentration in Crofer 22 APU considerably reduced it.

This is also confirmed in [98], where, comparing the behaviour of FSSs developed for SOFC interconnects, Crofer 22 APU was discovered to be the one showing the highest mass gain, but the lowest Cr evaporation.

Moreover in [35] it is pointed out that by applying the MCO coating on Crofer 22 APU both the mass gain and the Cr evaporation are drastically reduced. Then, in [65] the Fe-doping of MCO was proved to slightly reduced the mass gain

Therefore, it is here assumed that the mass gain measurements of Crofer 22 APU can be well approximated to the oxygen uptake due to the oxide scale thickening.

Few studies have been done on the AISI 441 oxidation behaviour and the results are generally contrasting. In [92] the authors found out the Cr release of bare AISI 441 is quite similar to the one of bare Crofer 22 APU, they also pointed out that this feature got worse when a MCO coating is applied on the first steel. On the other hand, in [102] it is concluded that the oxidation resistance of MCO coated AISI 441 is considerably improved compared to the bare one.

For both the steels, definitive results on the effect of Fe doping on MCO concerning neither the oxidation kinetics nor the Cr evaporation are available.

1.4.4. Electrical conductivity of interconnects

The evaluation of the electrical behaviour of an interconnect and its variation over the long-term presents some challenges. The different interactions between the steel and the coating mean that the electrical conductivity of the separate materials cannot simply be summed up together. Besides, it should be remembered that the growth of the oxide scale and of the reaction layer can substantially affect the electrical performances of the stack, both considering the resistance value and the degradation rate.

Therefore, the electrical characterization of the interconnect is mostly based on the measurement of the area specific resistance (ASR) [Ωcm^2], which offers the possibility to compare the properties of different interconnects, without the need to calculate the effect of each involved layer [132].

The ASR value is actually the sum of different factors, as expressed by:

$$ASR_{interconnect} = \rho_{spinel} * \tau_{spinel} + \rho_{chromia} * \tau_{chrom} + \rho_{reaction\ layer} * \tau_{reaction\ layer}$$

where, ρ is the specific resistivity and τ is thickness of each scale.

Since the resistivity of the steel is much lower than those of the scales, it is neglected in the formula.

The ASR is experimentally measured by a four-point set-up, shown in Figure 1.20; when an electric current is fixed to the system, the ASR can be calculated by measuring the voltage drop through the interconnect (ΔV):

$$ASR = \frac{\Delta V_{interconnect}}{I} \cdot A_{contact}$$

where I is the applied current and A is the contact area whose resistance is measured. The formula has to be divided by a factor of 2 for getting the resistance of only one of the surfaces.

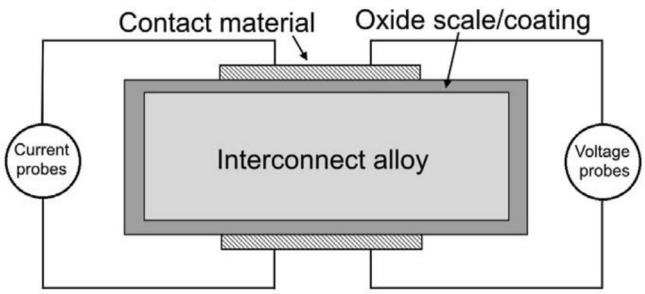

Figure 1.20: Illustration of the four-point set-up for ASR measurements [17].

The major issue regarding the ASR evaluation is the selection and definition of the contact materials [132].

Contact materials can be made of noble metals ([30], [133], [132]), or of materials typically used as SOFC cathodes, i.e. LSM ($La_{1-x}Sr_xMnO_3$) or LSC (LaSrCoO) ([19], [40], [65], [67], [134]).

In the first case the contacts are not supposed to react with the interconnect, thus providing a more theoretical ASR value; in the second, a more realistic evolution of the interconnect resistance can be deduced due to interaction between the sample and the contacts themselves ([17], [132]).

Since for both types of contacts, there is a wide variety of materials and production methods, it is not advantageous to compare ASR values from different researches, even if they have been conducted at the same temperature: the results are indeed much affected by the experimental procedure chosen and they generally show great scattering of data.

Another way to classify the ASR is by performing an "in-situ" or an "ex-situ" characterization, as defined in [132]; the first one refers to a continuous ASR measurement, while the second one to the discontinuous evaluation of it, following regular oxidation phases during which it is also possible to measure the mass gain.

The interest toward the ex-situ ASR is explained in the following. Since the oxide scale growth is considered to be the greatest factor determining the ASR value, it can be easily supposed that oxide scale thickening and ASR evolution exhibit similar time-dependent behaviour [133]: for this reason, it is important to link the ASR data with those of oxidation kinetics and microscopic analyses.

Considering that the conduction of the coating, of the oxide scale and of the RL as well is a temperature activated process following the Arrhenius equation, measuring the ASR during a step wise cooling allows to determine the temperature dependence of the ASR [65], as expressed by:

$$\frac{ASR}{T} = Ae^{\left(\frac{E_A}{kT}\right)}$$

where A is a pre-exponential factor [$\Omega cm^{-2}K^{-1}$], E_A is the activation energy [$kJmol^{-1}$], k is the Boltzmann's constant [eVK^{-1}] and T is the temperature [K].

In this work the ASR of the coated alloys was determined by two methods.

The first is the in-situ ASR with LSM contacts (here called ASR_LSM); the second is the ex-situ characterization using platinum contacts (named ASR_Pt), proposed in [132].

The results obtained by the two different approaches are compared.

2. Experimental procedures

2.1. Samples preparation

EPD

In this work, the EPD suspensions were prepared using a solution containing 60 vol.% of ethanol and 40 vol.% of deionized water, to which spinel $Mn_{1,5}Co_{1,5}O_4$ (Fuel cells materials, d_{50}=0,67 µm) and iron oxide Fe_2O_3 (Alpha Aesar, d_{50}< 0,50 µm) powders were added in different amounts, to reach a fixed concentration of 37,5 gL^{-1}. This formula was already tested in previous works for both MCO deposition ([19], [40]) and MCO/CuO co-deposition [67] and was therefore maintained without making further changes.

As discussed in section 1.3.1, $Mn_{1,5}Co_{1,5}O_4$ at room temperature is a mixture of $MnCo_2O_4$ and Mn_2CoO_4, ideally in the amount of 50:50.

Three different suspensions were prepared, containing none or different amount of iron oxide, but maintaining unchanged the concentration of the solid powders.

The first one, labelled as MCO, contains 0 wt.% of Fe_2O_3, the second one 5 wt.%, thus labelled 5FeMCO, and the third one 10 wt.% of Fe_2O_3, consequently labelled 10FeMCO. The Table 2.1 shows in detail the names and the compositions of the of the powder mixture for the EPD.

Table 2.1: EPD suspensions compositions.

Name	Wt.% MCO	Wt.% Fe_2O_3	Theoretical composition
MCO	100%	-	$Mn_{1,5}Co_{1,5}O_4$
5FeMCO	95%	5%	$Mn_{1,43}Co_{1,43}Fe_{0,14}O_4$
10FeMCO	90%	10%	$Mn_{1,35}Co_{1,35}Fe_{0,3}O_4$

For 5FeMCO and 10FeMCO samples the deposition process is better defined as a co-deposition.

Assuming that $Mn_{1,5}Co_{1,5}O_4$ and Fe_2O_3 deposited homogeneously and completely sintered, it was possible to calculate the theoretical composition of the doped coating after the in-situ formation of the spinel structure, as written in Table 2.1.

The steel compositions provided by the manufacturers are reported in Table 2.2.

Table 2.2: Steels compositions.

Steel	Manufacturer	Cr wt.%	Mn wt.%	Si wt.%	Nb wt.%	Ti wt.%	Ni wt.%	Al wt.%	La wt.%	Fe wt.%
Crofer 22 APU	ThyssenKrupp	23,00	0,45	<0,05	-	0,06	-	<0,05	0,1	bal
AISI 441	Sandvik	17,53	0,40	0,59	0,41	0,17	0,15	0,07	-	bal

Two different kind of samples were deposited (Figure 2.1): for oxidation resistance 2x2 cm coupons with a 3 mm hole at one corner; for area specific resistance, 2x6 cm coupons with 6 mm hole at both sides and a platinum wire (0,3 mm diameter) previously flattened and welded at the shorter edge.

Before the deposition, the samples were sonicated for 10 minutes in acetone, followed by 10 minutes in ethanol.

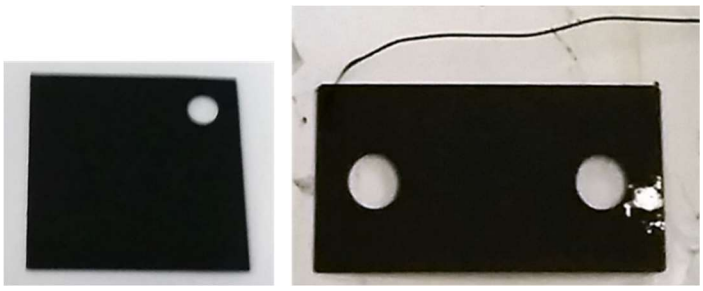

Figure 2.1: Steel coupons after the deposition;
at the left, for oxidation resistance, at the right, for ASR.

During the depositions, great attention was given to the suspensions stabilization and homogenization: for each experiment powders were added to the liquid solution, the suspension was mixed for 10 seconds by sonication in an ultrasonic bath and 10 seconds onto the magnetic stirrer, both for 3 times. Moreover, while not used for the EPD deposition, the suspension was always kept on the magnetic stirrer and before each utilization, the suspension was sonicated in the ultrasonic bath for few seconds. These procedures were adopted in order to avoid the sedimentation and/or aggregation of the powders in the suspensions and were considered necessary for achieving a good quality deposition.

I should be pointed out that each suspension was used during the day in which it was prepared; therefore, it is not possible to define the influence of a longer period of time on its stability, nor if it is possible to reactivate it after not being stirred for some time.

Figure 2.2 shows the EPD instruments used for this work.

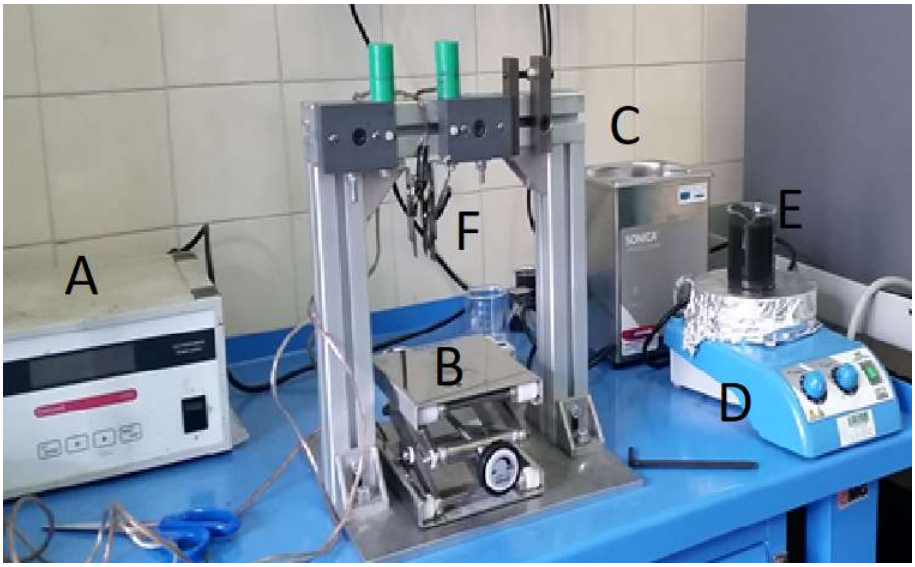

Figure 2.2: Set-up used for the EPD: A) Power supplier, B) Holder, C) Ultrasonic bath,
D) Magnetic stirrer, E) Becher, F) Counter electrodes.

EPD processing parameters can be summarised as follows:

- a constant voltage of 50 V for 20 seconds was applied, as already proposed in a previous study as being the best parameters for this kind of suspension [19]
- a three-electrode setup was chosen: in this case, two substrates of Crofer 22 APU (about 2x4 cm) were used as counter electrodes and the steel sample to coat was placed in the middle, at 1 cm distance from both others.

With these deposition parameters the final coating thickness is expected to be 10-15 µm.

As shown in Figure 2.3, the space between the three electrodes is very narrow, therefore, in order to avoid contacts among them and consequent circuit shortcuts, some isolating tape was used to cover part of the metal pieces.

This type of deposition is named cathodic, since the particles into the suspension are positively charged and they were deposited on the steel sample connected to the negative pole of the power supplier, thus acting as the cathode, whereas the counter electrodes were connected to the positive pole, then acting as anodes.

Furthermore, during the deposition it is relevant to observe the values of the current, even if the instrument control is on the applied voltage: indeed, this number could give a quick idea of the progress of the deposition. For example, if it is zero, a short circuit is likely happening, or, if it is too low, it is possible that the particles are not properly dispersed.

In this case, a current of 5-6 mA was registered for the oxidation resistance samples and 10-12 mA for the ASR samples (this difference is easily justified by the fact that the latter are twice the size of the former).

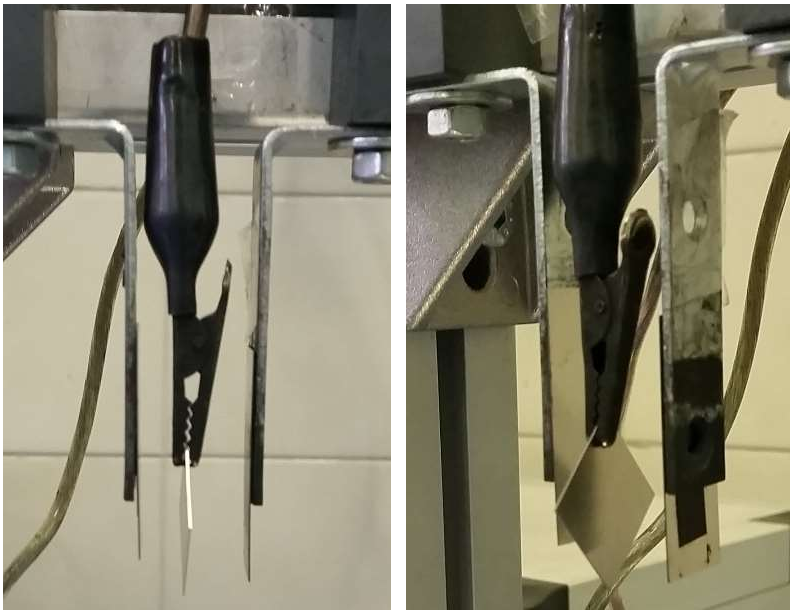

Figure 2.3: Close-up of the EPD instrument.

After the deposition, the samples were dried for at least 10 minutes before being removed from the EPD holder and being leaned on an alumina support, where they were let dry for about 24 hours, before the sinter.

In total, 48 samples were deposited, divided as shown in Table 2.3. Please note, twice the number of the 10FeMCO coated samples was prepared.

Table 2.3: Schematization of the deposited samples types.

Suspension	Crofer 22 APU		AISI 441	
	OR	ASR	OR	ASR
MCO	5	1	5	1
MCO5F	5	1	5	1
MCO10F	10	2	10	2
Tot samples	20	4	20	4

Sintering

In order to obtain a densification of the deposited coatings on the steel substrate, after drying at room temperature the coated samples were sintered following a two-steps route (see Chapter 1, Section 4.3).

Two different set of parameters were chosen.

Regarding the first one (Table 2.4) the reducing step was performed at 900°C for 2 hours in Ar/H_2 (4/5 vol.%) in a tubular oven; it was followed by the oxidizing step in air, at 900°C for 2 hours in a chamber furnace. MCO, 5FeMCO and half of the 10FeMCO samples were sintered this way, allowing to evaluate the effect of the Fe-doping.

On the other hand, in order to assess the influence of a different heat treatment at the same doping level, the second half of the MCO10F coatings was reduced at 1000°C, while maintaining unchanged all the others sintering parameters. From now on, these samples will be labelled as 10FeMCO_R1000 (Table 2.5)

Table 2.4: Parameters for the A type sintering.

	Samples	Sintering parameters	Temperature	Atmosphere	Time
Sint_A	**MCO, 5FeMCO, 10FeMCO (both steels)**	**Reduction**	900 °C	Ar/H_2 (5%)	2h
		Oxidation	900 °C	Air	2h

Table 2.5: Parameters for the B type sintering.

	Samples	Sintering parameters	Temperature	Atmosphere	Time
Sint_B	**10FeMCO_R1000 (both steels)**	**Reduction**	1000 °C	Ar/H_2 (5%)	2h
		Oxidation	900 °C	Air	2h

2.2.Characterization

2.2.1. Oxidation and gravimetric measurements

Five samples for each kind of coating, for both Crofer 22 APU and AISI 441, were produced for the study of the oxidation kinetics. Each sample was numbered from 1 to 5; the fifth of each kind was chosen as reference sample, thus it was not inserted in the furnace and it was used for XRD and FE-SEM/EDX characterization.

The oxidation behaviour of the thirty-two remaining samples was studied, using the chamber furnace, whose internal view is shown in the Figure 2.4Figure 2.4: a) internal top view of the chamber.

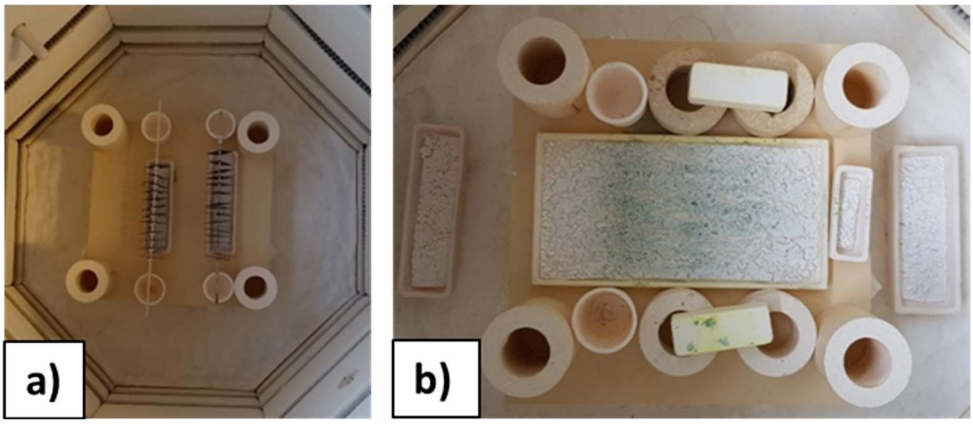

Figure 2.4: a) internal top view of the chamber; b) strontium carbonate powder after oxidation.

As it can be seen in Figure 2.4, the furnace is insulated by alumina and the internal struts used to hold the samples are made of the same material; a thermocouple is placed on one side of the chamber wall.

Some alumina boats filled with strontium carbonate powder were put into the furnace (Figure 2.4 b)in the zone under the samples, and replaced regularly. This powder changes colour from white to yellow/green when contaminated by volatile products generated at high temperature: thus, it was used to check if some leakage was taking place and if it was generally varying over time.

Coated samples were hung vertically, thanks to alumina rods inserted in the 3 mm diameter hole in the corner of every steel coupons (Figure 2.5).

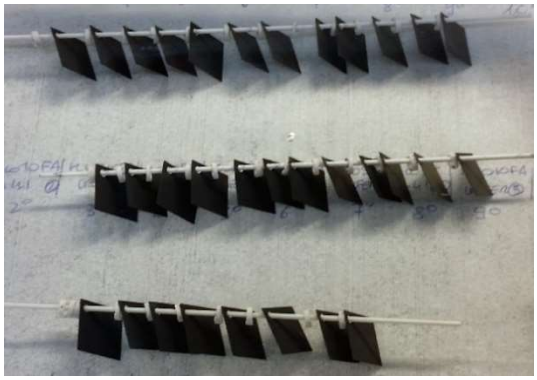

Figure 2.5: Coated samples on alumina rods.

The oxidation behaviour was thus studied at 750 °C, in static air (in the chamber there was no forced air flow and the moisture level was not measured) for a total time of 2000 h.

Every 250 h, the furnace was cooled till room temperature in order to weight the samples (by a XS205 Mettler Toledo weight scale, 10-5 g of accuracy): for this reason, it is good to highlight that the oxidation was studied under cyclic conditions, that can therefore be easily influenced by the effects of CTE mismatch between the layers.

The heating and cooling ramp were fixed at 120 °C/h.

After 1000 h (corresponding to four thermal cycles), one samples for each kind was extracted from the furnace and used for XRD, FE-SEM and to perform the ASR measurement with Pt contacts; therefore, the mass gain values were obtained on an average of three to four samples.

Figure 2.6 offers a sketch of the specimens' order into the oxidation furnace and what they were used for.

It can be noted that in order to prevent any kind of furnace charging effect, the samples were alternated considering both the substrate material and the coating compositions.

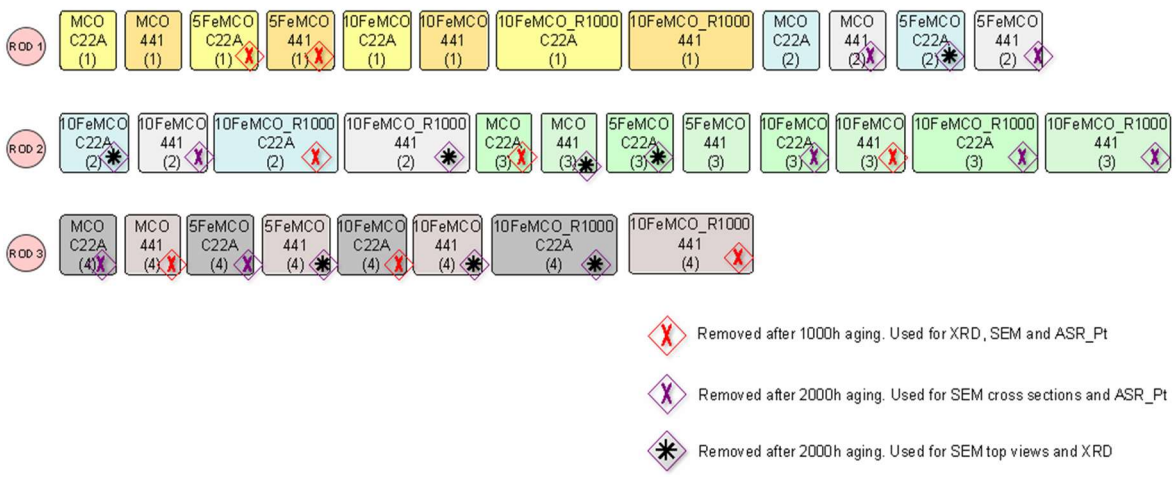

Figure 2.6: Sketch of the specimens' order in the oxidation furnace and what they were used for.

It is relevant to note that starting from 750 h at 750 °C, the AISI 441 samples revealed a colour alteration on the surface, visible at the naked eyes; this behaviour was almost not observed for all Crofer 22 APU samples. As shown in Figure 2.7, a darker shadow appeared and grew over time, staring from the opposite side compared to where the coupons were hung (so the bottom corner).

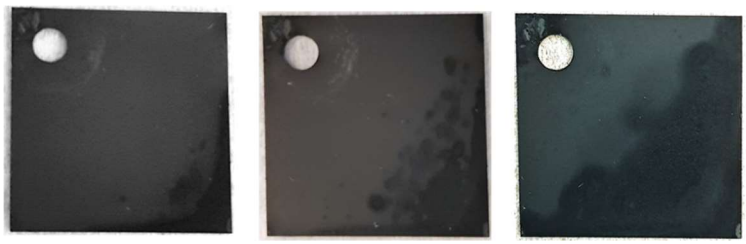

Figure 2.7: Shadows on 10FeMCO_R1000_441 after 750, 1000 and 2000 h at 750 °C.

The shapes and the position of those areas seem to suggest that some evaporation and condensation process took place during the oxidation and, since they were present only on coated AISI 441; it could be hypothesized that these surfaces are somehow more reactive towards the atmosphere inside the furnace.

The results concerning the oxidation test are presented in Section 3.2 , where also the gravimetric measurements of bare Crofer 22 APU and bare AISI 441, concurrently tested at DTU, are considered as references.

2.2.2. Area specific resistance

In this work two approaches were chosen to electrically characterize the coated steel behaviour.

The main one, is the measurement of the area specific resistance by using LSM contacts, which can be defined an "in-situ" characterization.

The second one is an "ex-situ" characterization, based on the use of Pt contacts; this method was proposed in [132] and all the experimental procedures here adopted followed that kind of approach.

ASR with LSM contacts

The sintered 2x6 cm coupons for ASR were placed in a stack, as shown in Figure 2.8: this kind of set-up allowed to test them all together, by a series connection.

The samples were ordered on the basis of the coating, alternating the two steels.

At the top and at the bottom of the stack, two gold foils (0,3 mm) were disposed, to distribute the electric current during the measurement.

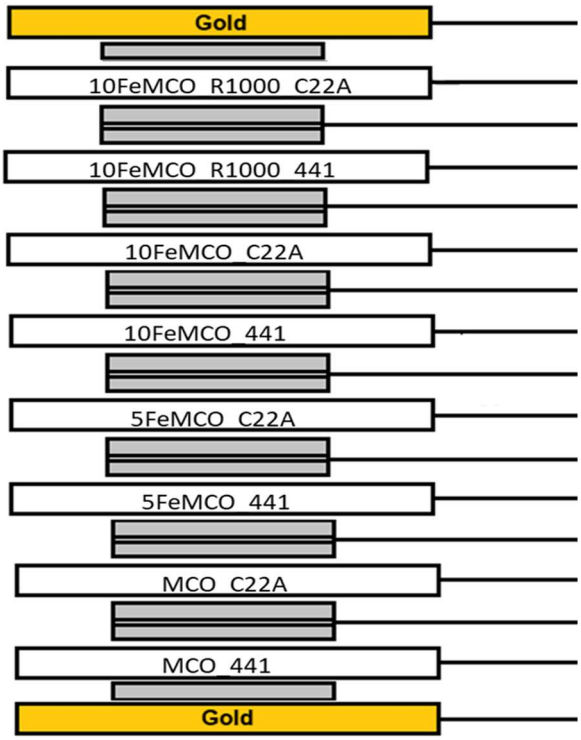

Figure 2.8: Schematization of the ASR set-up, with samples order.

As it can be noted from Figure 2.8, the samples were separated from each other by two contact plates, between which a platinum wire was positioned that allowed to measure the voltage drop between the two faces of the sample.

20x20x1 mm porous LSM ($La_{0,85}Sr_{0,1}Mn_{1,1}O_3$) plates produced by slip casting and spray coated by 50-60 µm layer of LSM (0,89 wt.%) and Co_3O_4 (11 wt.%) to improve the surface area (as described elsewhere [17], [134]), were used as contacts.

In Figure 2.9, a picture of the samples arrangement in the measurement stack is proposed; they were kept in place by two short alumina rods fitted into the two holes on the sides, whereas the LSM place were place only in the middle.

Some alumina spacers are used to avoid undesired contacts between samples/wire that could cause electrical short circuit and modify the resistance values.

At the top, an 8 kg weight was positioned to improve the contact area and to prevent the specimen from sliding.

Figure 2.9: Arrangement of the samples in the ASR stack.

Both the platinum wired welded on the samples and that place between the LSM contacts were numbered and connects to the corresponding at on the controller of the rig.

Each wire was covered by insulating ceramic fibres by Nextel in order to avoid possible contacts (Figure 2.10 a).

The clam shell furnace utilized for the test can be seen in Figure 2.10 b.

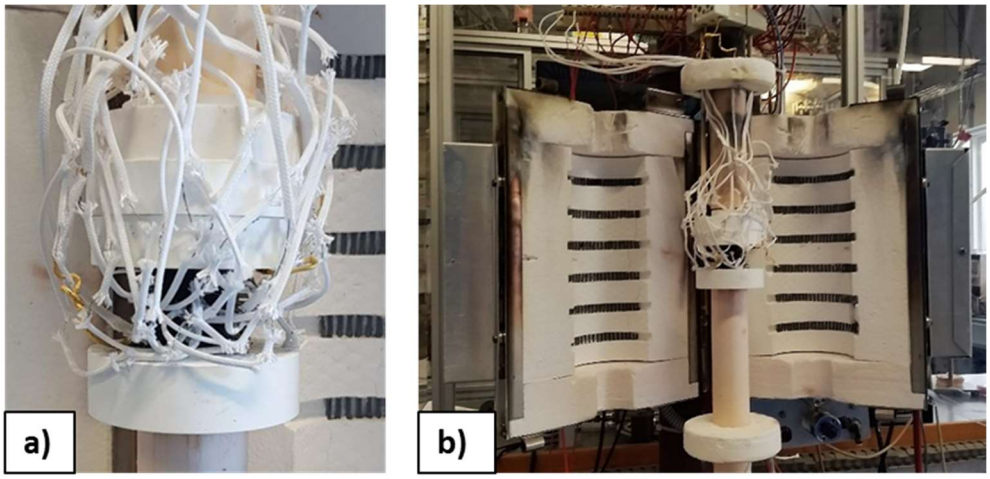

Figure 2.10: a) stack placed inside the rig and b) view of the open furnace.

Two thermocouples, in addition to the one of the furnace, were placed next to the samples (approximately one at the top and one at the bottom of the stack) to monitor the temperature. The temperature values differed by 8 °C at 750 °C.

The furnace was heated up to 750 °C and a current of 2 A, corresponding to 0,5 Acm^{-2} was applied.

The voltage drop was measured for 3200 h, at constant temperature of 750°C in ageing conditions in static air.

For each sample two voltage drops were recorded by an external resistor, labelled as ΔV_1 and ΔV_2, as it is shown in Figure 2.11,.

Since the two ΔV were measured across different interfaces (the former, between the LSM-coating-oxide scale, the second, steel-oxide-scale-coating-LSM) they were both monitored to check any dependence of the electrical resistance on the current direction.

At the end of the test, it was confirmed that no significant variation among the ΔV_1 and ΔV_2 occurred for all the samples.

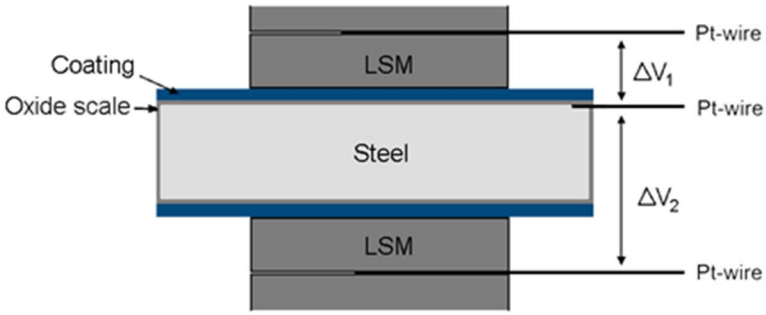

Figure 2.11: Illustration of the interfaces over which the voltage drops were measured [17].

The area specific resistance of each contact was measured according to:

$$ASR = \frac{\Delta V}{I} \times A$$

where ΔV is the voltage drop, I is the current and A is the contact area, defined by the LSM plates (4 cm^2).

Considering the specification of the external resistor, the equation was them modified in:

$$ASR = R_{ext} \times \frac{V_{sample} \times A}{V_{ext}}$$

where R_{ext} corresponds to 0,012 Ω and V_{ext} was overall voltage constantly measured by the external system.

It is worth to note that calculating the resistance in this way, the final ASR values are to be considered relative only to one of the samples (i.e. half of the interconnect resistance).

After 3200 h the rig started to cool down because of an unintentional and unexpected shutdown.

Anyway, it was possible to calculate the activation energies for the electrical conduction; these data, together with the ASR results will be presented in section 3.3.

At the end of the cooling of the rig all the wires were cut and the stack was taken out of the furnace; after checking that no colour alteration and no spallation occurred (Figure 2.12), it was embedded into epoxy resin for the subsequent SEM/EDX characterization (presented in Section 3.3.1).

Figure 2.12: ASR stack at the end of the measurement.

ASR with Pt contacts

For the measurement of the ASR using platinum contacts one coupon for each studied case from the oxidation resistance test after both 1000 and 2000 h aging were used. They were all cut as shown in Figure 2.13 in order to obtain squares of 1x1 cm.

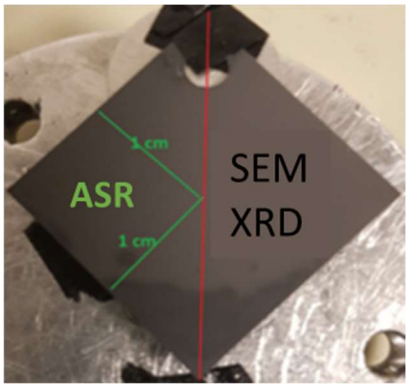

Figure 2.13: Cut of the 1000 and 2000 h aged samples for ASR_Pt measurement.

In order to get a well-defined contact area some steel coupons with a 6 mm hole (corresponding to a contact area of 0,28 cm^2) were used as masks for the platinum sputtering, which was performed with a BAL-TEC SDC 005 applying a current of 30 mA for 120 s, in order achieve a platinum layer of ca. 10 nm (Figure 2.14 a). The sputtering was repeated for the both sides of each sample.

Subsequently, the sputtered circles were hand painted with a platinum paste provided by Ferro, using a fine brush. The Pt paste was let dry, placing the coupons on a hot plate, before painting the other side; then they were all placed in the oven at 200 °C for 2 h, in order to complete the drying.

For the resistance measurement, the samples were then placed in a measurement rig with four slots (Figure 2.14 b), connected to a Solartron SI 1260 impendence analyser.

The frequency was set between 0,1 and 1 Hz; therefore, the test can be considered as being quasi-DC and the imaginary part of the impedance can be neglected.

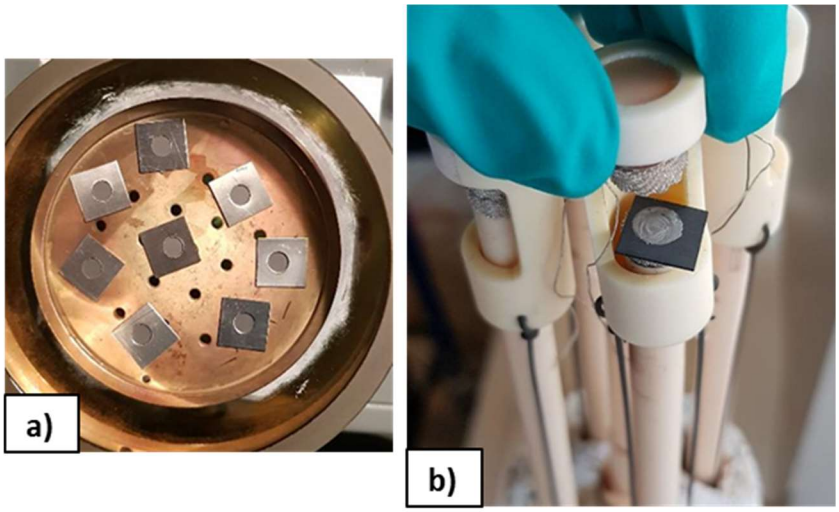

Figure 2.14: a) specimens covered by the masks, in the sputtering machine;
b) close-up of the sample after the Pt brushing, in the measurement rig.

The rig was heated up to 750 °C. The electrical resistance was measured during the cooling every 50 °C till reaching 350 °C; twelve values were collected for each sample at every temperature.

The heating and cooling ramp were set at 120 °C/h.

Even if the resistance was recorded till 350 °C, the activation energies were calculated in the 750-600 °C T range, were the ASR dependence on the temperature was still linear, as presented in Section 3.3.

3. Results and discussion

3.1. Microstructural investigation of the reduced and as sintered samples

The microstructure of the coatings after both the reducing and re-oxidizing steps was evaluated by a field emission scanning electron microscope (FE-SEM) Zeiss merlin equipped with an energy dispersive X-Ray analyser (EDX) by Bruker. The crystalline phases have been studied by X-Ray diffraction (XRD) with the Bruker D8 instrument.

Figure 3.1 compares the XRD patterns of the undoped MCO and of 10FeMCO. As it can be clearly seen, there is no residual Fe_2O_3, which entirely decomposed and formed the intermetallic compound $Co_{0,7}Fe_{0,3}$.

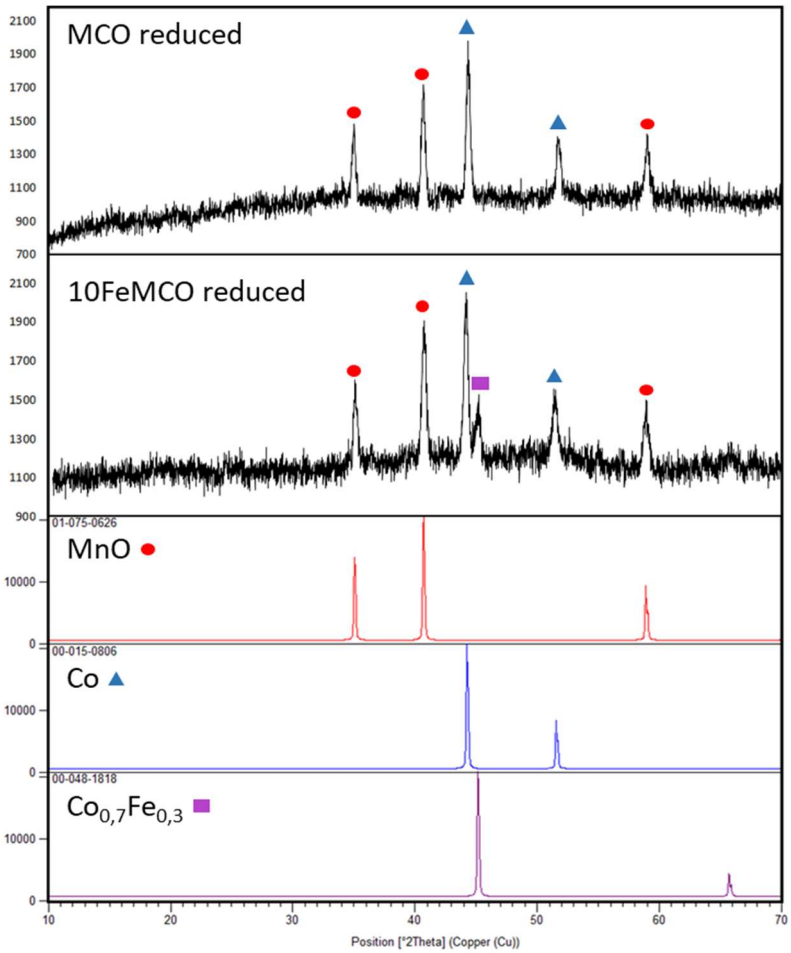

Figure 3.1: Comparison of the XRD patterns of MCO and 10FeMO after the reducing step.

In Figure 3.2 and Figure 3.3 FE-SEM cross section images at different magnitudes of the reduced samples and the interfaces with the substrate of Crofer 22 APU are presented.

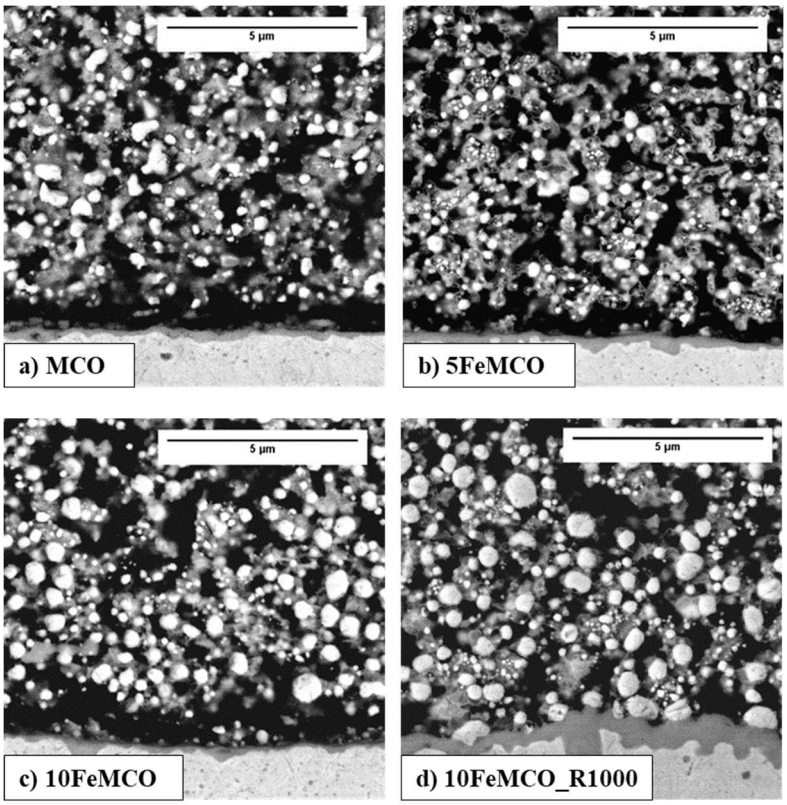

Figure 3.2: SEM cross section AsB images of the reduced samples: a) MCO, b) 5FeMCO c) 10FeMCO, d) 10FeMCO_R1000.

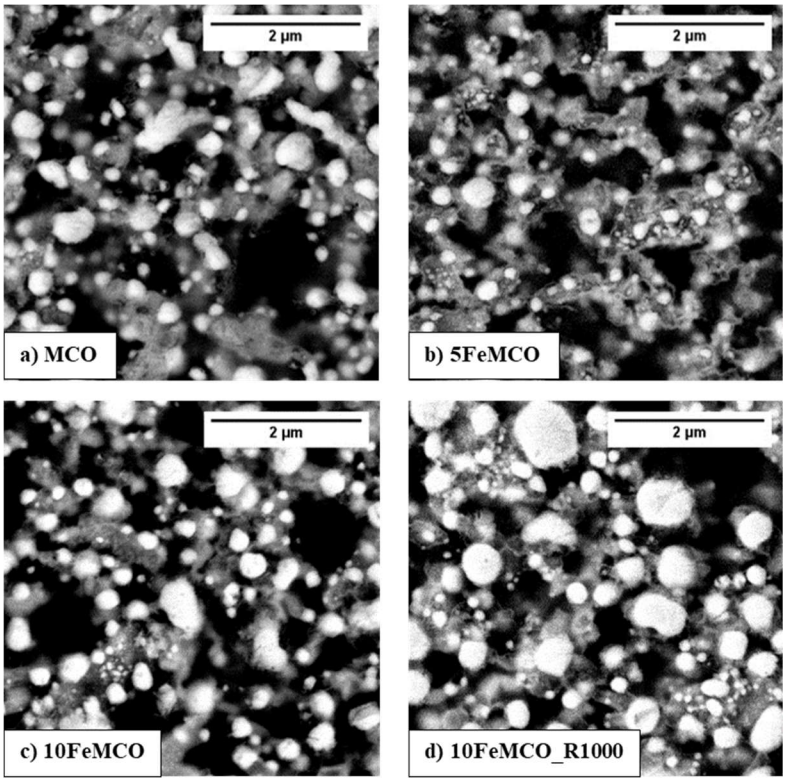

Figure 3.3: SEM cross section AsB images of the reduced samples: a) MCO, b) 5FeMCO c) 10FeMCO, d) 10FeMCO_R1000

Comparing the four images in Figure 3.2 and Figure 3.3, some qualitative considerations can be done.

The brightest regions are metallic particles of Co and probably $Co_{0,7}Fe_{0,3}$ reduced from the prior oxide powders; otherwise, the grey areas are made of the unreduced MnO.

The shape and the dimension of metallic particles in the MCO coating are not regular and their amount is not homogeneous through the coating (e.g. in Figure 3.2 a, to the left they are bigger and more numerous than to the right).

The effect of a non-constant distribution of the metallic particles in the reduced state is not negligible. Since the cubic ($MnCo_2O_3$) and the tetragonal (Mn_2CoO_3) spinels require a different Co/Mn ratio to be obtained, it follows that the areas richer in Co will be cubic while in other areas tetragonal phases are present. This point will be discussed also later concerning the as sintered samples.

Even if it was not possible to define an accurate particles distribution, by comparing the MCO to the 5FeMCO coating some differences can be observed: metal particles are overall better distributed throug the coating, meaning that the dimensional distribution is narrow, the shape is more regular and the diameter on an average is smaller.

Furthermore, in 5FeMCO many bright spots, which are not detected in the undoped coating, are visible (Figure 3.3 b),; because of their nanometric dimension (too small to be detected and analysed by EDS), the composition is by now unknown, even if it is conceivable that they are made of the $Co_{0,7}Fe_{0,3}$ intermetallic compound.

By adding 10% of Fe (Figure 3.2 and Figure 3.3 c), together with the overall coarsening of the metal dots, the dual distribution is still present: indeed, among the larger spherical particles, some smaller ones are seen.

This effect related to particles coarsening is enhanced by performing the reducing step at 1000°C instead of 900°C.

In Figure 3.2 and Figure 3.3 d, a more evident mismatch between the two distributions can be verified, since the higher temperature brought to the coarsening of metallic Co and to the formation of even more grown, and well dispersed, spheres.

The 10FeMCO_R1000 sample is the only one that showed some reaction with the substrate (where a thicker oxide scale can also be observed compared to the other samples).

After the re-oxidizing step of the sintering, the spinel structure was formed again. In Figure 3.4 the XRD pattern of the re-oxidized 10FeMCO is reported: the peaks of both the cubic and tetragonal phases are detected, showing a shift toward lower 2θ.

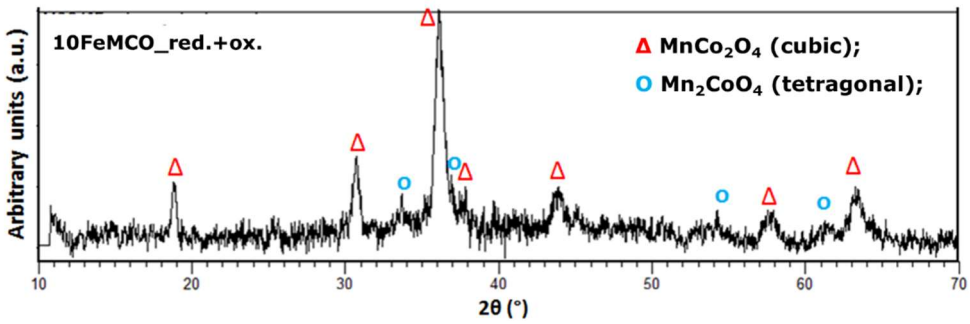

Figure 3.4: XRD pattern of 10FeMCO at the end of the sinter.

After the two-step sintering, one sample for each kind of coating/steel was analysed by FE-SEM and EDS: their cross-section images are presented in Figure 3.5. As expected, the thickness for all these coating is ca. 10-15 µm.

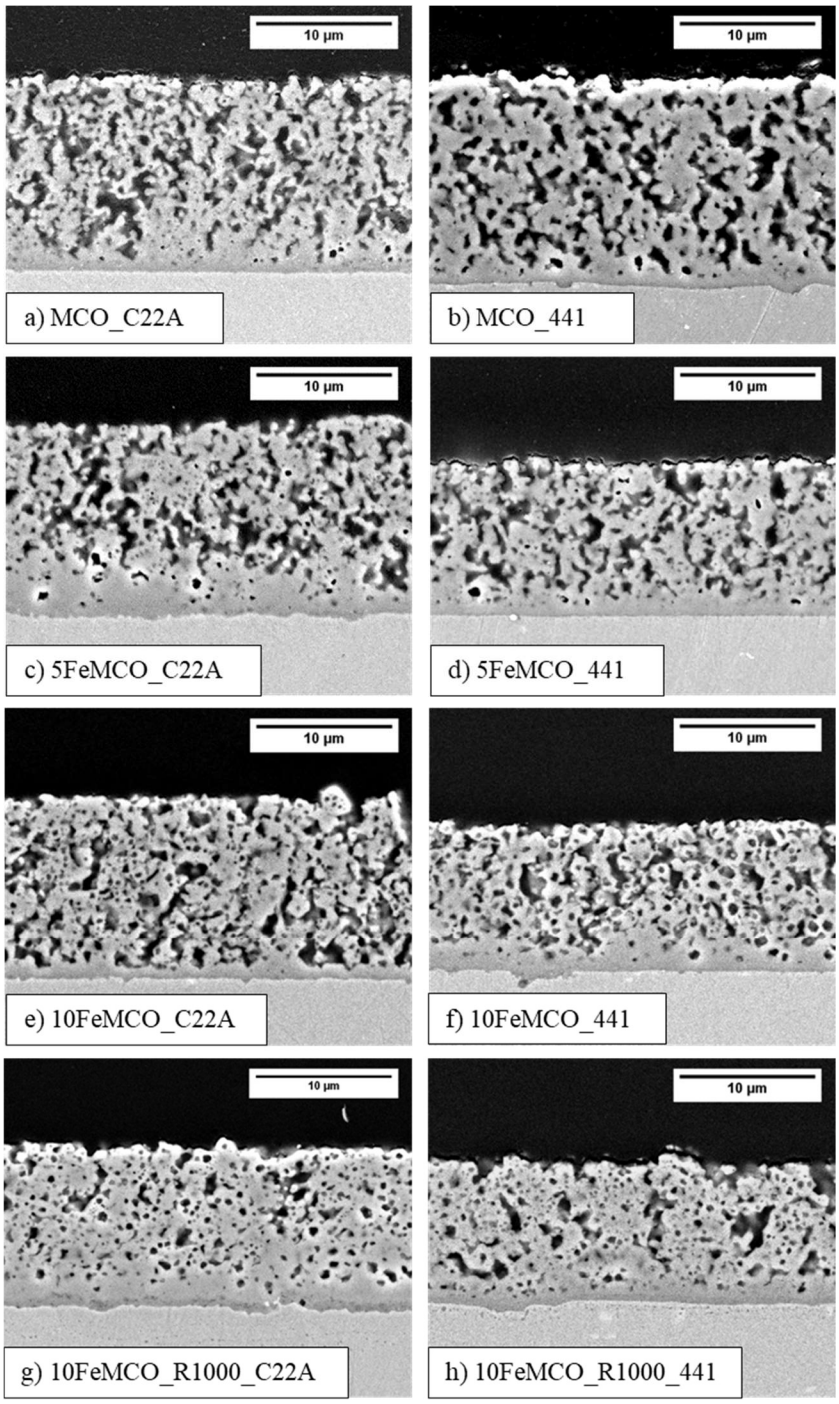

Figure 3.5: SEM cross section HE-SE2 images of the "as sintered" samples: a) MCO_C22A, b) MCO_441, c) MCO5F_C22A, d) MCO5F_441, e) 10FeMCO_C22A, f) 10fEMCO_441, g) 10FeMCO_R1000_C22A, h) 10FeMCO_R1000_441.

Since the HE-SE2 detector was used, in Figure 3.5 the chromia layer is not visible.

After sintering no relevant differences between the Crofer 22 APU and AISI 441 behavior can be highlighted.

Starting from the undoped coatings, it can be seen that the porosity is open and continues almost till the steel interface; in the 5FeMCO, a denser layer was formed at the bottom part.

Compared to those, the 10FeMCO seems to show more close porosity, at least with less communicating pores. This effect is for sure enhanced in the 10FeMCO_R1000 coating, where both close porosity and higher densification are appreciable, proving what already stated in [50], about the Co coarsening.

Anyway, in order to better evaluate the porosity of the coatings, it was calculated using the IMAGEJ image processing software, taking into account threes images from different zones of each sample.

The pictures width was between 35 and 65 µm and the considered area was the one between the coating/steel interface in the inner part and, concerning the external part of the coating, the approximate average between the peaks and the valleys on the surface.

This image processing method is itself characterized by a certain level of inaccuracy with respect to the porosity values obtained and some systematic error has to be considered; therefore, the porosities calculated cannot be regarded as absolute values, but only for verifying the presence of trends between the different samples.

The obtained values are shown in Table 3.1, together with the standard deviations related to them, as well as an evaluation of the doping and the sintering effect.

Table 3.1: porosity values calculated for each studied case.

Steel	**Sample**	Average porosity %	Std. Dev. 3 images	Doping /sintering effect on porosity
AISI 441	MCO	34,5%	1,0%	-
	5FeMCO	31,2%	1,37%	-3,3%
	10FeMCO	29,3%	4,19%	-5,2%
	10FeMCO_R1000	19,8%	2,96%	-14,7%
Crofer 22 APU	MCO	27,5%	6,75%	-
	5FeMCO	26,5%	5,74%	-1%
	10FeMCO	24,6%	3,45%	-2,9%
	10FeMCO_R1000	18,0%	2,88%	-9,5%

Looking at the last column in Table 3.1 it is possible to make out two different trends: on the one hand, all the coatings on Crofer 22 APU seem to be a bit denser than those on AISI 441, on the other hand, the addition of Fe (comparing the 5% and 10% doped coating to the undoped one) seems to slightly improve the densification.

Nevertheless, since the standard deviations generally overlap the porosity reduction due to the Fe doping, this conclusion is untimely; indeed, in [65] the inefficacy of iron doping in improving the densification, at least after the sintering, was already proved.

The processing of the reducing step at 1000 °C instead of 900°C seems to have more influence on densification after sintering.

In Figure 3.6, the densification trends for each coating on both steels are reported.

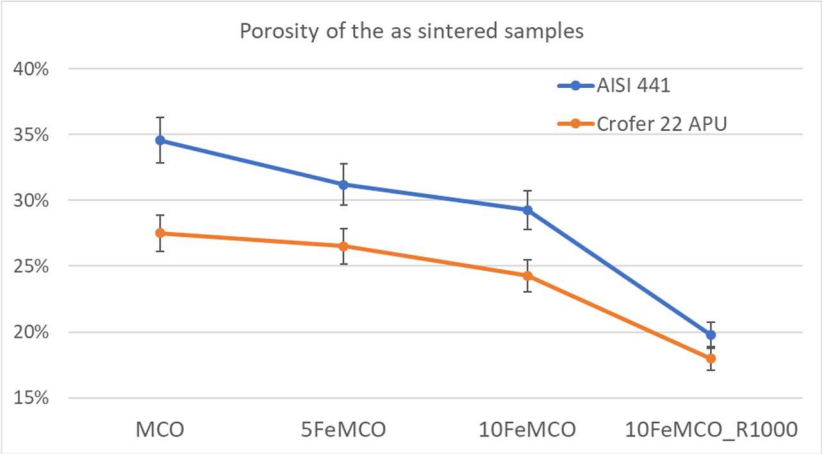

Figure 3.6: Porosity values for all the studied cases.

A detailed element distribution through the coating and at the interface with the steel was investigated by EDS line scan analysis.

The EDS line scan of MCO_441 sample after the two-step sintering is reported in Figure 3.7. A crack at the interface between the steel and the coatings visible, THE presence of the crack made impossible to measure the oxide scale thickness after the heat treatment but suggested that the reactions occurred probably during the sintering were not sufficient to produce a strong interface.

A remarkable fluctuation of the Co and Mn signal can be observed, thus confirming the presence of both the cubic and the tetragonal spinel.

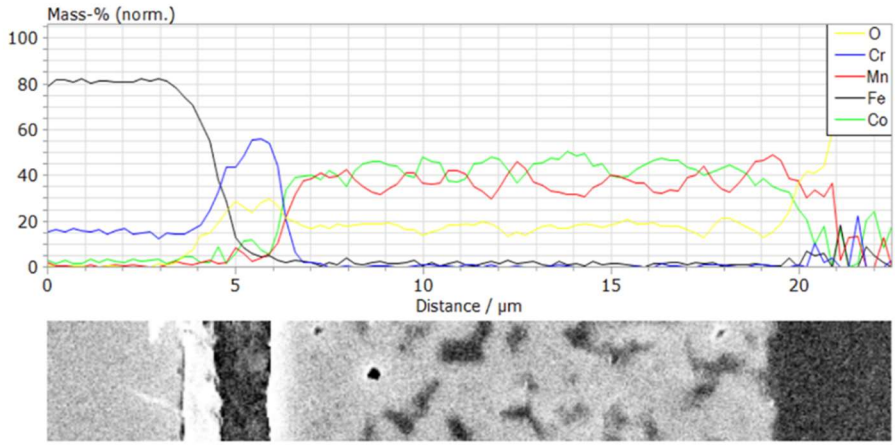

Figure 3.7: EDS line analysis on MCO_441 after the sinter.

In Figure 3.8, then, a comparison between the EDS line scans of 10FeMCO and 10FeMCO_R1000 on Crofer 22 APU is proposed; as anticipated while discussing the morphology of the reduced coating, the higher temperature of the reducing step caused a broader oxidation of the steel substrate.

Furthermore, comparing Figure 3.7 and Figure 3.8, one can also check that, by the Fe addition to the spinel, the Mn and Co lines inside the coating are much more stable, suggesting that the Fe-doping promoted the formation of smaller grains of the cubic and the tetragonal phases.

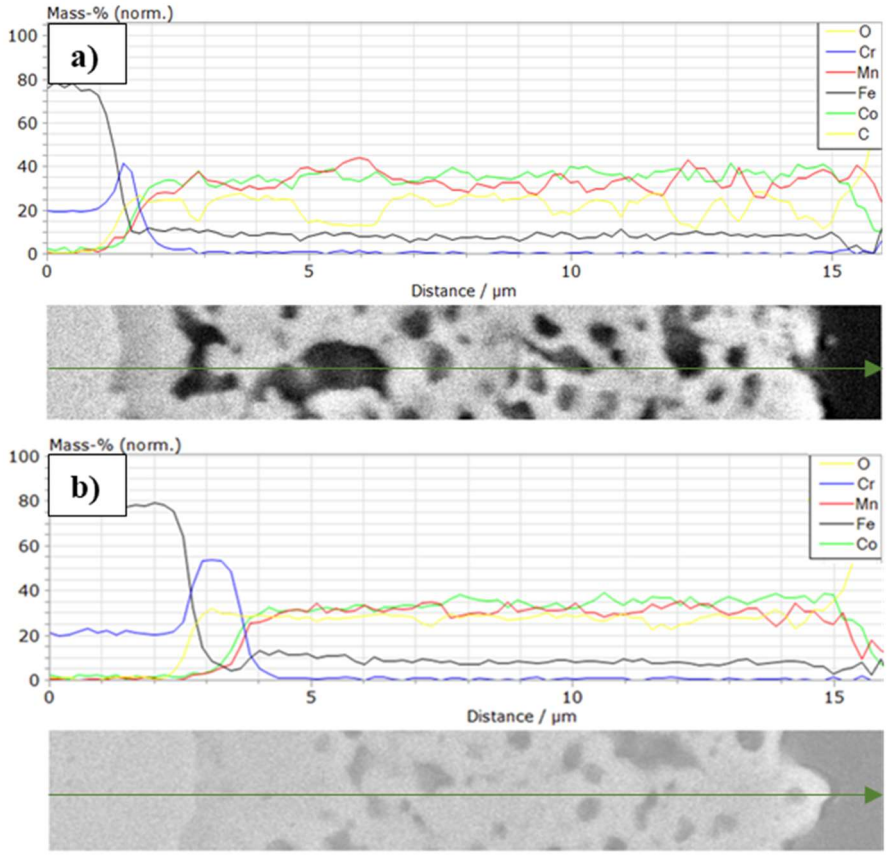

Figure 3.8: EDS line scans on a) 10FeMCO_C22A and b) 10FeMCO_R1000_C22A, both after the sinter.

3.2. Oxidation kinetics

Figure 3.9 shows the mass gain per unit of area [mg cm^{-2}] over time, for both coated AISI 441 (triangles) and Crofer 22 APU (squares); different colours refer to different coatings.

Each point is the average value between three to four weighted samples.

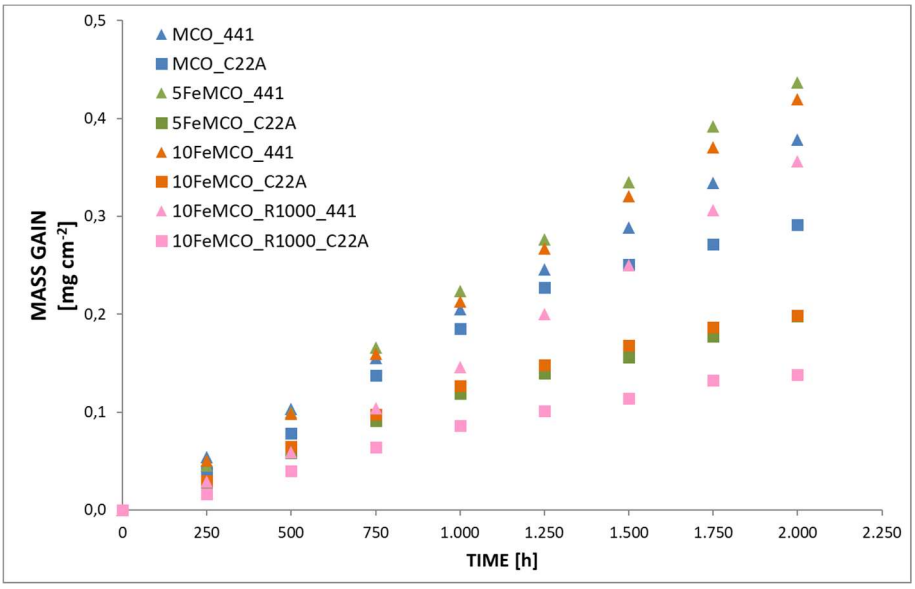

Figure 3.9: Mass gain of MCO (blue), 5FeMCO (green), 10FeMCO (orange) and 10FeMCO_R1000 (pink) on Crofer 22 APU (squares) and AISI 441 (triangles) (750°C, air)

From data reported in Figure 3.9, we can see that all the Crofer 22 APU coated samples showed a lower mass gain than those of AISI 441, demonstrating a better oxidation behaviour (i.e. limited oxide scale growth).

Furthermore, it is also underlined that the mass gain of the different coatings is not following the same trend comparing the two substrates, hence suggesting that the oxidation behaviour of the steel/coating system is not due to the sum of the effects of single elements, but there is an interaction between the two of them that influenced the oxidation results.

Table 3.2 shows an overview of the final mass gain values. It is apparent from this table that, as expected, the bare steels showed higher mass gain compared to the coated ones with the same substrate.

Furthermore, the lower mass gain was obtained for the 10FeMCO sample reduced at 1000°C on Crofer 22 APU; the same coating represents the best case for the AISI 441 too, but its value is very similar to the undoped MCO, which on Crofer 22 APU is the worst case.

For both steels, 5FeMCO and 10FeMCO coatings are characterized by a very similar mass gain, even if for the Crofer 22 APU it is half of the AISI 441 ones.

Table 3.2: Mass gain values of the coated steels (750°C, air, 2000h).

Mass gain after 2000h at 750°C in air [mg cm^{-2}]					
Steel/coating	MCO	5FeMCO	10FeMCO	10FeMCO_R1000	Bare
Crofer 22 APU	0,29	0,20	0,20	0,14	0,41
AISI 441	0,38	0,44	0,42	0,36	0,45[2]

It is difficult to compare these values of mass gain with those from literature, due to differences in test parameters (temperature, aging time, atmosphere), but generally they are in the same range of the results already found.

[2] This value was obtained by extrapolation; the last measured mass gain for bare AISI 441 was 0,35 mg cm^{-2}, after 1250 h at 750 °C.

As already discussed in the Introduction, when the rate limiting step for the oxidation is the diffusion of anions (O^{2-}) or cations (M^{n+}), the mass gain should follow a parabolic shape, according to the parabolic kinetics expression:

$$\left(\frac{\Delta m}{A}\right)^2 = 2k_{p,m} \cdot t + C$$

Therefore, a straight line is obtained by plotting the mass gain in parabolic unit versus time.

Figure 3.10 shows data for Crofer 22 APU samples. The red dots are related to the bare Crofer 22 APU mass gain.

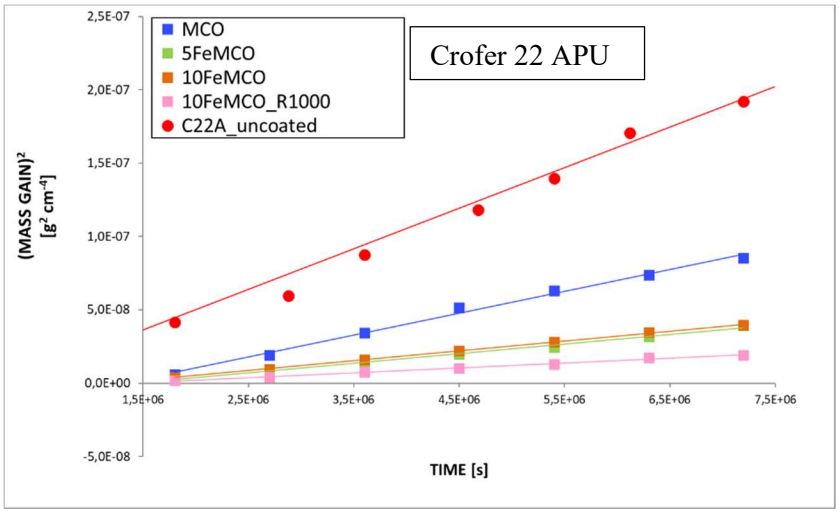

Figure 3.10: Parabolic mass gain per unit of area versus time of coated and bare Crofer22APU (750°C, air).

Since the fit to the parabolic equation was high for all Crofer 22 APU samples, it was possible to calculate the corrosion rate $k_{p,m}$ [g^2 cm^{-4} s^{-1}], which is simply the slope of these straight lines[3], with quite high accuracy.

The values of $k_{p,m}$ (from 500 to 2000 h) are summarised in Table 3.3; calculations were made in order to ignore the contribution of initial transient phenomena (due to the formation of the first oxide layer) and taking into account only the steady state of the oxide scale growing.

Table 3.3: $k_{p,m}$ values for Crofer 22 APU samples

Oxidation rates $k_{p,m}$ [g^2 cm^{-4} s^{-1} 10^{-15}]					
Crofer 22 APU	Bare	MCO	5FeMCO	10FeMCO	10FeMCO_R1000
	26,9	14,5	6,6	6,6	3,3

Comparing the first two columns in Table 3.3, it can be noted that the corrosion rate of the MCO coated steel is almost half the value of the uncoated one. Furthermore, the application of Fe-doped coatings progressively reduced the corrosion rate till a factor of ~10.

In particular, reducing the deposited 10FeMCO at 1000°C instead of 900°C lead to decrease of the oxidation rate from 6,6 to 3,3 $10^{-15}g^2$ cm^{-4} s^{-1}. This improvement is partly due to the lower porosity level

[3] For simplicity, the slope of the straight lines was considered, not dividing by the factor 2, as required by the parabolic law.

achieved thanks to the heat treatment at the higher temperature, which is in line with what was found by the authors in [35]. However, it is likely that the Fe-doping as well has some effect on it.

Anyway, these findings suggest that, considering the oxidation rate, an interconnect made of Crofer 22 APU coated by 10FeMCO_R1000 could work for more than 8 times longer than the uncoated one.

Results for the samples with AISI 441 as substrate (see Figure 3.11) show a different behaviour.

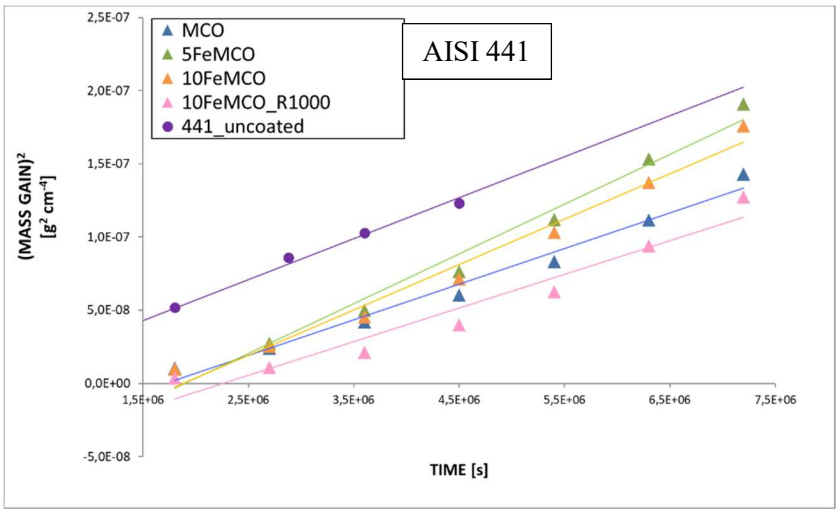

Figure 3.11: Parabolic mass gain per unit of area versus time of coated, bare and preoxidized (2 h, 900 °C) AISI 441 samples.

Furthermore, in Figure 3.11, the trend lines are not really fitting the experimental data ($0{,}94 \leq R^2 \leq 0{,}97$), proving that in this case the oxidation is not completely parabolic. This means that, apart from the diffusion of cations and anions between the steel, the oxide scale and the coating, another process could be responsible for the mass gain of the AISI 441 samples.

It was therefore observed that the data were better fitter by two segments, one between 500 and 1250 h, and the other from 1250 and 2000h: therefore, the $k_{p,m}$ values were calculate for AISI 441 samples as well, splitting the two periods of time, as they are reported in Table 3.4.

Table 3.4: Kp values for AISI 441 bare and coated samples.

Oxidation rates K_p [g^2 cm^{-4} s^{-1} *10^{-15}]					
AISI 441	Bare	MCO	5FeMCO	10FeMCO	10FeMCO_R1000
500-1250 h	26,2	18,5	24,6	22,8	13,4
1250-2000 h		30,6	42,7	38,5	32,5
AVERAGE	26,2	24,6	33,7	30,6	23,0

Surprisingly, the oxidation rates of MCO and 10FeMCO_R1000 are only slightly lower than those of the bare steel; whereas those of 5% and 10% doped coatings are actually higher, indicating that the Fe presence could even worsen the steel performance.

As already said, according to the parabolic law, the rate of oxide scale thickening over time should gradually decrease, i.e. the $k_{p,m}$ should be almost constant (it is obtained plotting the data in parabolic unit). In this case, the $k_{p,m}$ values for AISI 441 samples increased over time (as shown in Table 3.4): it can be concluded that, apart from the ions diffusion, at least one other process occurred that deflected the parabolic trend.

This was better understood thanks to the microscopy characterization, as presented afterwards.

3.2.1. Microstructural investigation of the 1000 and 2000 h aged samples

FE-SEM top view images of the 1000 h aged samples are presented in Figure 3.12.

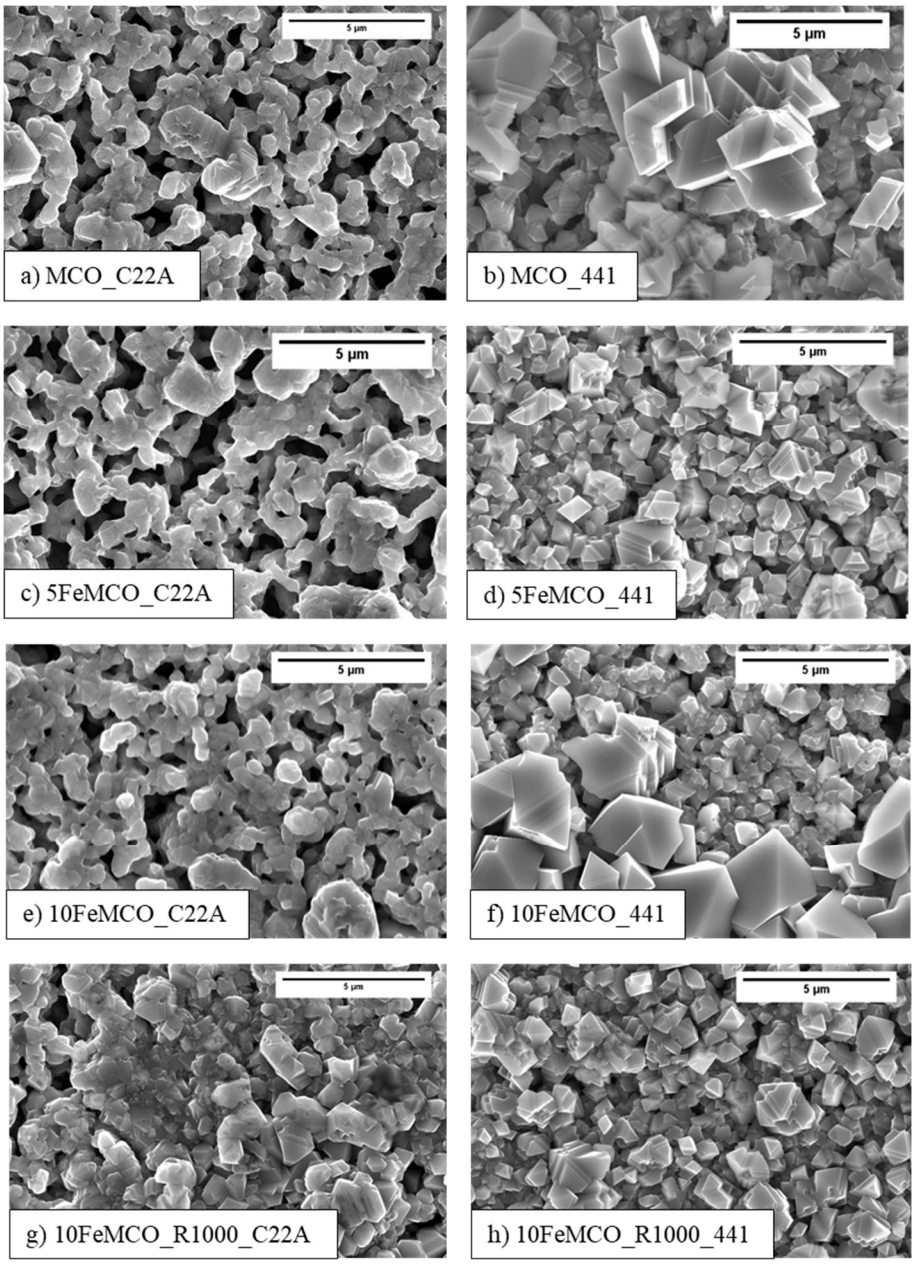

Figure 3.12: FE-SEM top view images of the 1000 h aged samples, InLens detector: a) MCO_C22A, b) MCO_441, c) 5FeMCO_C22A, d) 5FeMCO_441, e) 10FeMCO_C22A, f) 10fEMCO_441, g) 10FeMCO_R1000_C22A, h) 10FeMCO_R1000_441.

Concerning the Crofer 22 APU (Figure 3.12, left column) it is apparent that the surfaces of MCO and 5FeMCO are similar, presenting quite a high porosity, whereas the coatings doped with 10% of Fe appear to be denser, especially considering the one reduced at higher temperature (i.e. 10FeMCO_R1000_C22A).

Anyway, the surface morphologies were generally heterogeneous , so that all the coatings on Crofer 22 APU showed some areas of high density (similar to Figure 3.12 g) together with some more porous ones (similar to Figure 3.12 a and c).

It was possible to estimate the surface porosity for the coatings on Crofer 22 APU, by the same method already explained for the as sintered samples. The results are presented in Table 3.5: what is interesting about the data in this table is the effect on densification of Fe doping.

Table 3.5: Surface porosity of coatings on Crofer 22 APU

Steel	Coating	Average porosity %	Doping/sintering effect
Crofer 22 APU	MCO	17,6%	-
	5FeMCO	9,2%	-8,4%
	10FeMCO	5,2%	-12,4%
	10FeMCO_R1000	3,6%	-14%

Considering the AISI 441 samples, at the right column of Figure 3.12, the difference in morphology is evident: the surfaces of all samples are covered by crystals of different dimension and, even in areas where the coating is still visible; porosity is practically absent (for this reasons, calculating the surface porosity of AISI 441 samples was considered meaningless).

These crystals were detected mainly in the lower part of the samples, compared to where they were hung in the furnace: as already shown in Section 2.1, the same areas presented some darker shadows.

As an example, in Figure 3.13, two images of the 5FeMCO coating on AISI 441 are proposed: one a is from the centre (a), the other one is from the lower corner of the coupon (b).

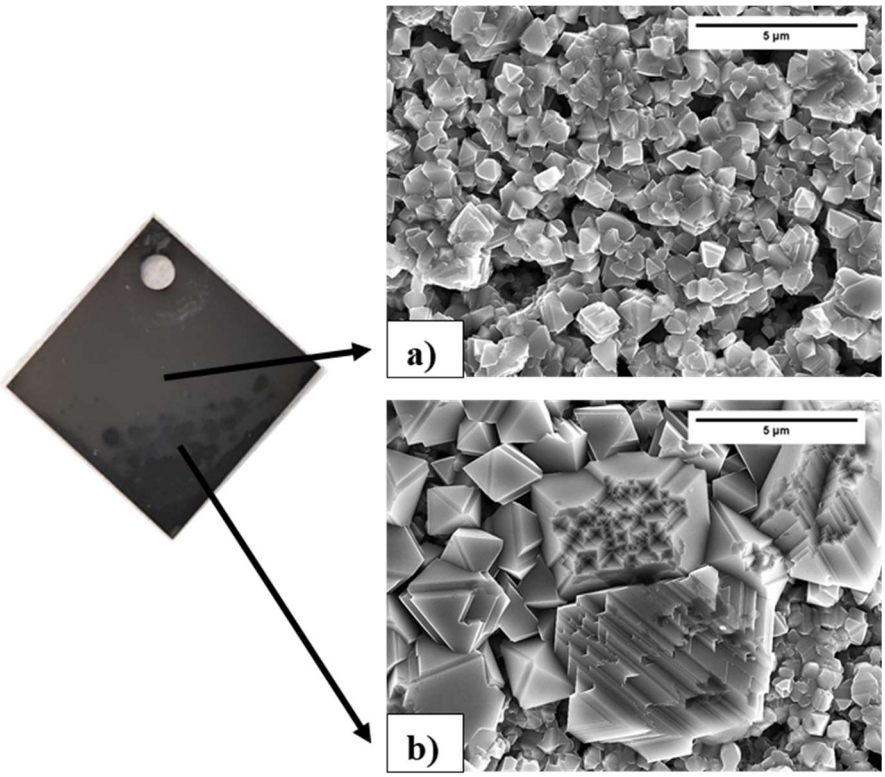

Figure 3.13: FE-SEM top view of 5FeMCO on AISI 441.
a) centre of the sample; b) lower corner. InLens detector.

EDS analysis on Figure 3.13 b, revealed that the crystals grown on the surface contains 25 wt.% (norm.) of chromium (Co= 22 wt.%, Fe= 2 wt.%, Mn= 20 wt.%, O= 31 wt.%).

EDS maps of 10FeMCO on AISI 441 (same area of Figure 3.12 f) are reported in Figure 3.14; the transition between the coating and the Cr rich spinel can be seen.

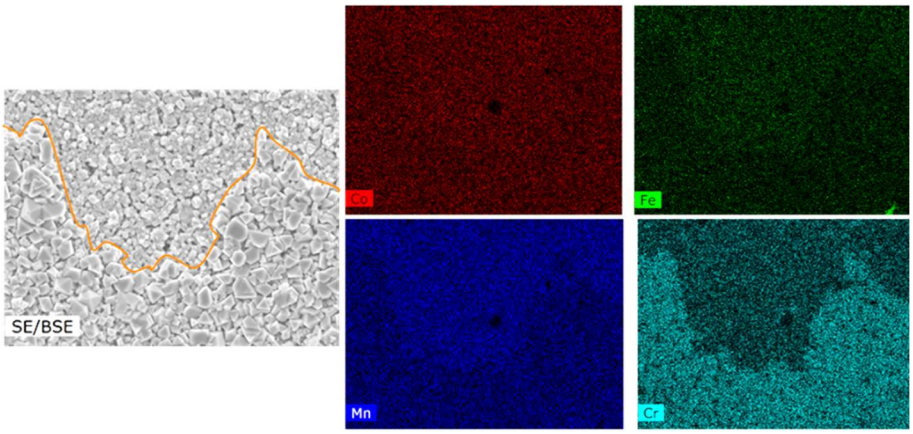

Figure 3.14**:** EDS map 10FeMCO coating on AISI 441.
The orange line highlights the transition between the coating and the Cr rich area.

Considering the composition and the shape of those crystals, they are identifiable as mixed spinel, due to the reaction between the coating and chromium.

The cross sections of the same 1000 h aged samples are presented in Figure 3.15 (Please note the different magnification for the MCO coating on AISI 441 (b).

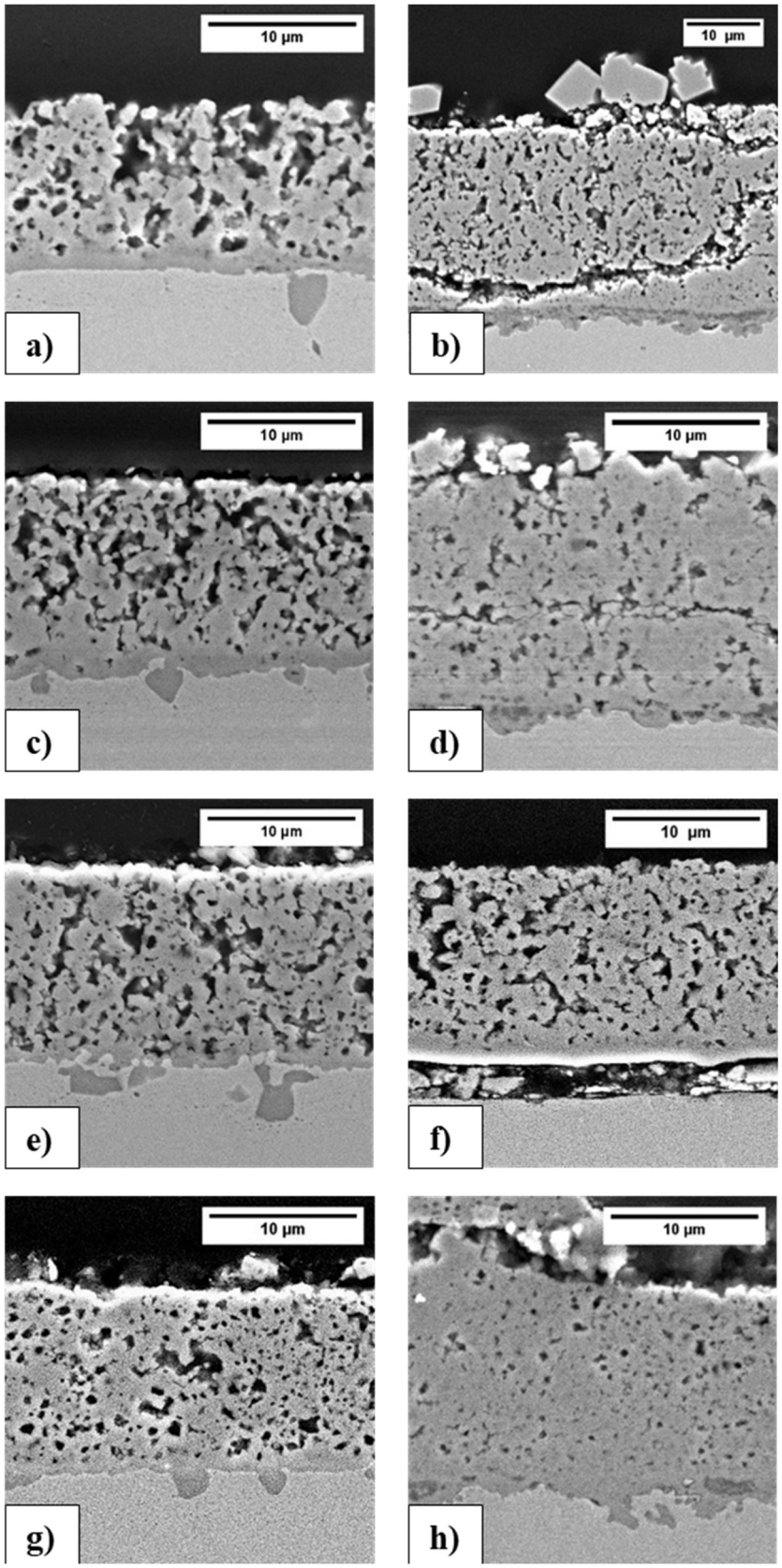

Figure 3.15: FE-SEM cross section images of the 1000 h aged samples, HE-SE2:
a) MCO_C22A, b) MCO_441, c) 5FeMCO_C22A, d) 5FeMCO_441, e) 10FeMCO_C22A, f) 10fEMCO_441, g) 10FeMCO_R1000_C22A, h) 10FeMCO_R1000_441.

Comparing these images to those of the as sintered samples (Section 3.1), it is clear that the densification increased significantly during the first 1000 h at 750 °C; Table 3.6 presents the porosity results obtained by the same method explained for the as sintered samples.

Table 3.6: Porosity and doping/sintering effect on densification after 1000 h aging at 750 °C.

Steel	Sample	Porosity av. %	Std. Dev. 3 images	Doping /sintering effect on porosity	Compared to as sintered
AISI 441	MCO	11,3%	3,6%	-	-22%
	5FeMCO	12,5%	1,7%	-1,2%	-19%
	10FeMCO	13,0%	2,4%	-1,7%	-18%
	10FeMCO_R1000	2,8%	0,2%	-8,5%	-17%
Crofer 22 APU	MCO	16,3%	3,0%	-	-21%
	5FeMCO	21,8%	4,0%	+5,5%	-7%
	10FeMCO	9,3%	1,9%	-7,0%	-14%
	10FeMCO_R1000	5,8%	3,0%	-10,5%	-8%

As it can be noted from the last column, compared to the as sintered cases, the porosity decreased by ca. 7-22%, variably for each sample.

Considering the porosity, the greater effect was recorded for the 10FeMCO_R1000 on AISI 441, whereas the 5FeMCO on Crofer 22 APU less densification was obtained, so that its porosity is higher than the undoped coating.

It was found quite challenging to link both the densification and the doping effect in order to have a trend, so only the effect of the higher reducing temperature can be remarked.

Some differences can be observed considering Figure 3.15 a and b, both showing the undoped coating on the two substrates,

The MCO coating on Crofer 22 APU exhibits a good adhesion with the steel and no cracks occurred at the interface. Moreover, the presence of some Mn-Cr spinels (average composition: Cr= 40-45 wt.%, Mn= 20-25 wt.%, O=30-35 wt.%) inside the steel (as the one that can be seen at the lower right) proves the efficacy of the alloy composition toward the retention of Cr diffusion into the coating. These two properties were verified for the doped coatings on Crofer 22 APU as well (see Figure 3.15 c, e and g).

Considering the MCO coating on AISI 441 (Figure 3.15 b), it is possible to observe the same crystals, already highlighted in Figure 3.12 b, on the surface.

Many cracks starting from the interface coating/steel and propagating throughout the coating are present; this was detected also in 5FeMCO and 10FeMCO on AISI 441 (Figure 3.15 d and f) but not for 10FeMCO_R1000.

Those cracks are likely due to mechanical stresses occurred during thermal cycling; however, since no spallation was seen, they probably propagated during the polishing of the epoxy cylinder for the SEM preparation. In any case, their presence suggests the weakness of the coating/AISI 441 interface, somehow improved by the higher temperature in the reducing step (indeed the 10FeMCO_R1000 coating, in Figure 3.15 h, apart from not having cracks, showed an interface similar to the ones on Crofer 22 APU).

Comparing the two steels (left and right columns in Figure 3.15) something can be noted about the kind of porosity: for Crofer 22 APU pores are generally bigger and open, whereas for AISI 441 they tend to be smaller, close, but in a greater number.

It was possible to estimate the thickness of the oxide scale to ca. 0,5 µm for coatings on Crofer 22 APU and 1÷1,5 µm for AISI 441; no significant variation depending on the Fe-doping was recorded. These values were obtained on the basis on EDS line scans results on each sample, comparing three different images.

Almost no reaction layer was identified, for both the substrates, even if it is good to remember that this kind of measurement cannot be of a high precision, due to the interaction volume of the X-Rays.

Since the chromium retention capability is among the indispensable properties of protective coatings for a FSS interconnect, one of the major issues, on which the EDS analysis was focused, was the evaluation of the origin of the Cr-rich spinels on the surface of the coatings on AISI 441. It was very important to check if the remarkable chromium amount came from the samples themselves.

Figure 3.16 shows an EDS line scan of the cross section of MCO_441 after aging, which is also a good example for the behaviour of the Fe-doped samples joined with the same steel. The chromium amount is coloured in blue.

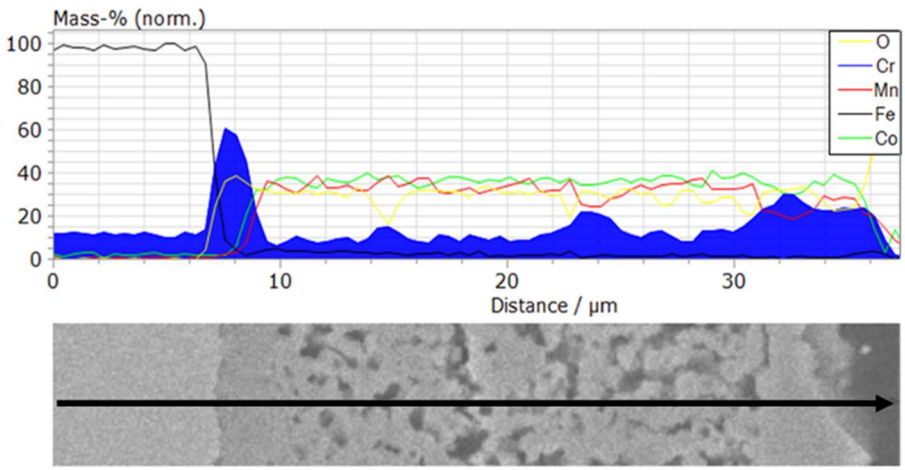

Figure 3.16: EDS line scan of the cross section of MCO on AISI 441, aged for 1000 h

As shown in Figure 3.16, the Cr profile is increasing going from the coating to the surface, till reaching concentration higher than the one inside the steel: since a diffusion profile from the inside toward the surface would have been the opposite, this was taken as a proof that the Cr was not diffusing trough the oxide scale and the coating.

Furthermore, it is worth pointing out that the migration of such a high quantity of chromium would certainly have caused a “destructive” oxidation of the steel coupons.

In some areas of coated Crofer 22 APU chromium was detected, as well: in Table 3.7, EDS points composition of 5FeMCO is reported. Concerning the coating, the higher amount of it is at point 5 (where also more Fe was recorded), just on the surface. Point 1 points out the Cr-Mn spinel, whereas point 2 is likely to underline the reaction layer.

Table 3.7: EDS points composition on 1000 h aged 5FeMCO_C22A.

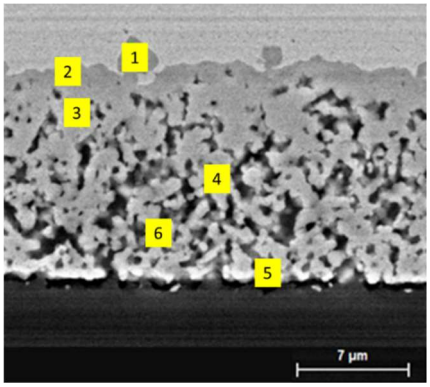

Point	O wt.%	Cr wt.%	Mn wt.%	Co wt.%	Fe wt.%
1	30,9	41,0	22,8	0,8	2,0
2	29,4	25,8	15,5	22,7	5,2
3	27,0	1,1	32,4	30,3	7,5
4	27,4	1,0	34,5	28,0	7,4
5	18,7	3,2	32,0	36,4	8,3
6	27,1	2,5	28,2	33,3	7,4

The presence of chromium could be explained as following. In the furnace, together with the coated samples, there were also some Crofer and AISI 441 uncoated sample; besides, the furnace was used for a long time for testing of many different steels and coatings, without being properly cleaned. For these reasons, a Cr contamination of the furnace atmosphere determined the condensation on the coatings surface, the inward diffusion and reaction of this element with the coatings.

Anyway Cr was not present in every area of the coatings on AISI 441; e.g. in Figure 3.17 the EDS line scan of 10FeMCO_441 shows that the Cr amount in the coating is very low (a low quantity of it can be due to the polishing procedure).

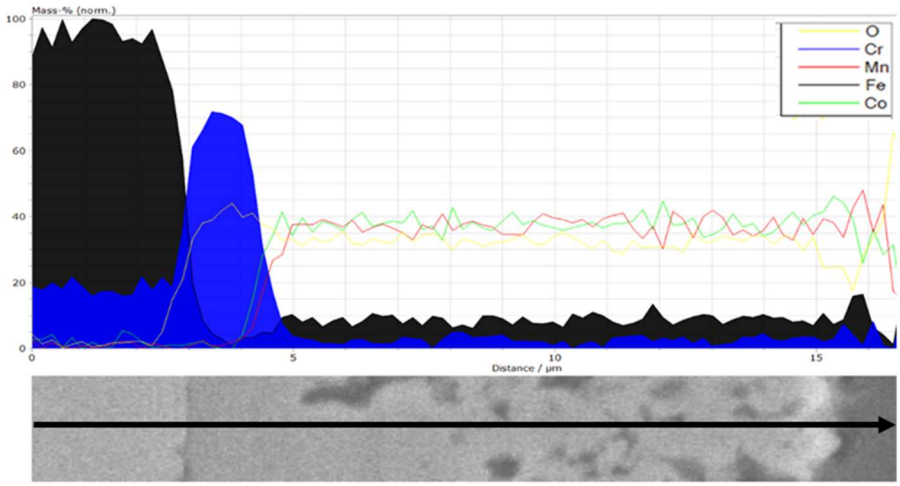

Figure 3.17: EDS line scan of the cross section of 10FeMCO_441, aged for 1000 h.

Always from Figure 3.17, one can see the oxide scale of ca. 1,5 µm, a very thin reaction layer (at around 4,5 µm on the x-axis, where the green Co signal is higher before the one on Mn) and the Fe line stable at 8-10 wt.%.

As a comparison, in Figure 3.18 the EDS line scan on 10FeMCO_R1000_C22A coating is presented; it is a good example for the behaviour of all the studied coatings on Crofer 22 APU.

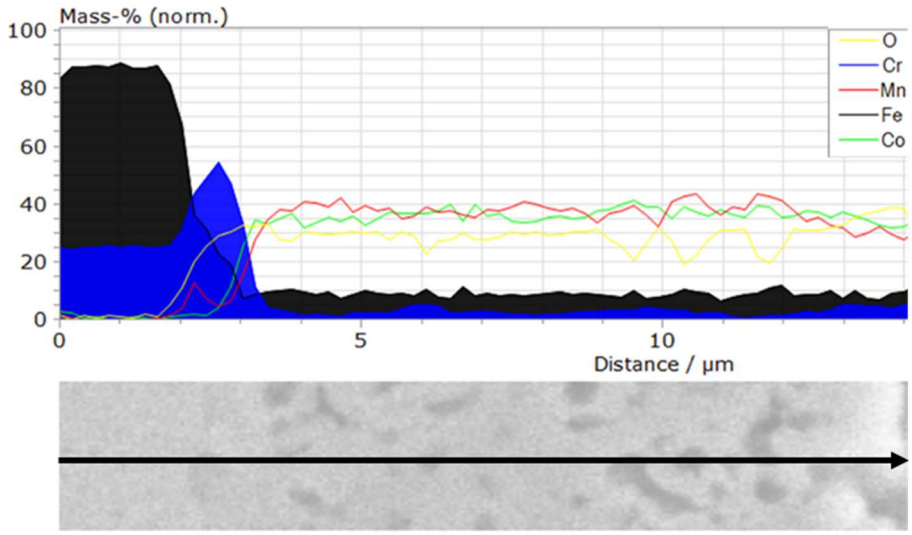

Figure 3.18: EDS line scan of the cross section of 10FeMCO_R1000 on Crofer 22 APU, aged for 1000 h.

Figure 3.18 shows at least four interesting points: first, the Mn-Cr spinel below the steel surface (Mn is the red line), followed by an approximated oxide scale of 0,5 µm and by a thin reaction layer (similar to Figure 3.17), and finally, the Fe amount constant at around 10 wt.% through the whole coating.

Figure 3.19 is an EDS map on 10FeMCO_C22A, in which all the topics already discussed can be verified. Here, the Cr amount inside coating is 1-2 wt.%, whereas Fe is at 9-10 wt.%

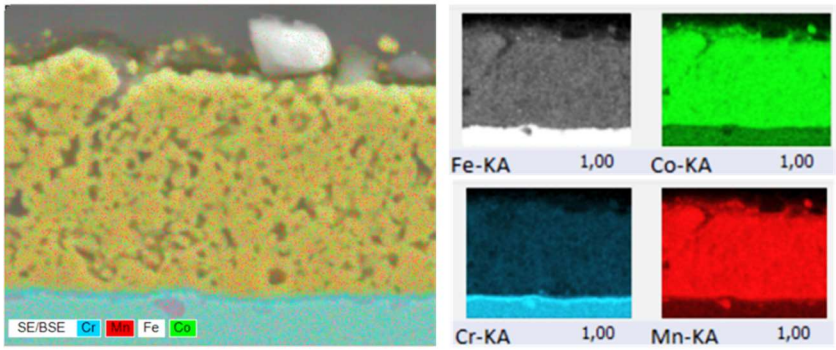

Figure 3.19: EDS map of 10FeMCO on Crofer 22 APU after 1000 h aging

Moving to the 2000 h aged samples, the top views of each of them are proposed in Figure 3.20.

Please note the different magnification for the MCO coating on AISI 441 (b).

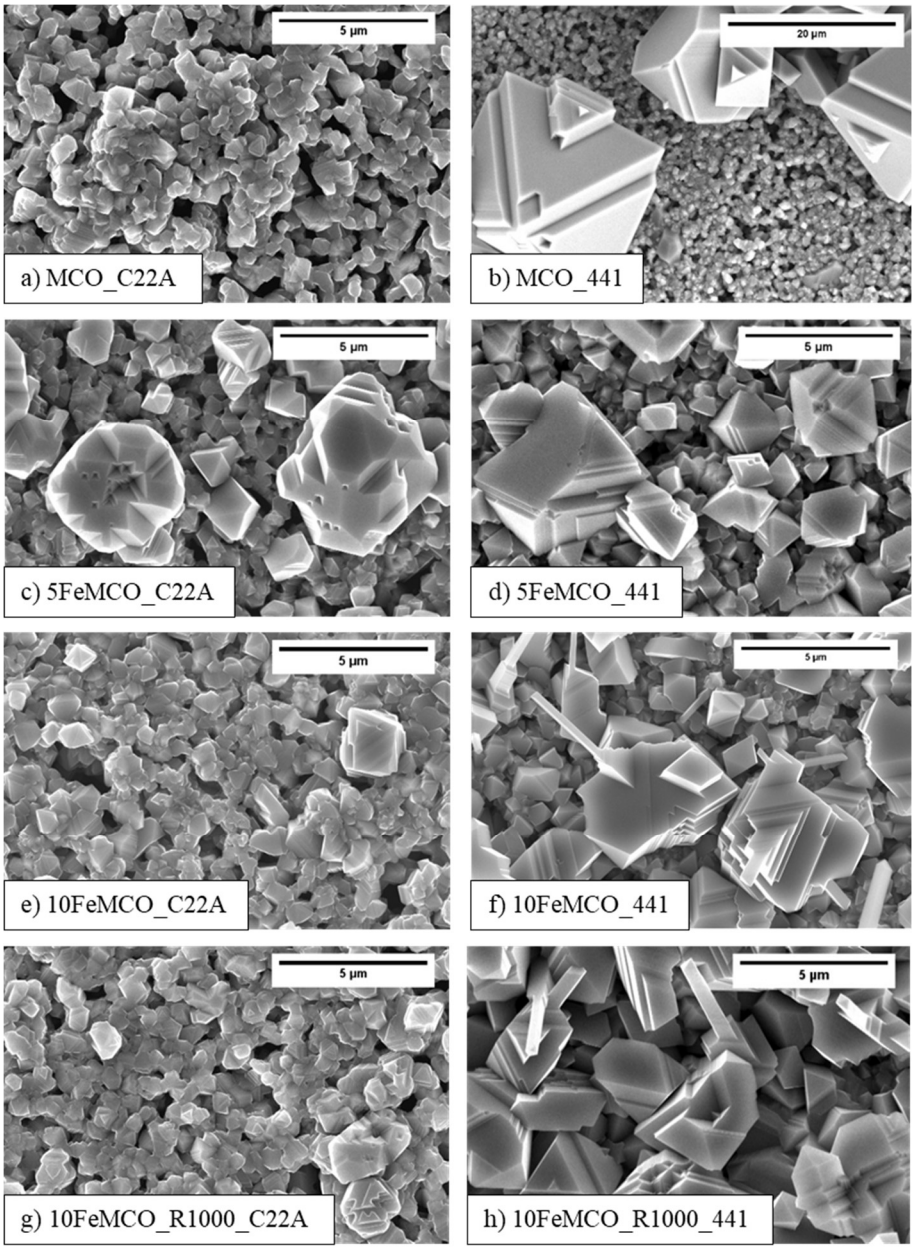

Figure 3.20 : FE-SEM top view images of the 2000 h aged samples, InLens detector: a) MCO_C22A, b) MCO_441, c) 5FeMCO_C22A, d) 5FeMCO_441, e) 10FeMCO_C22A, f) 10fEMCO_441, g) 10FeMCO_R1000_C22A, h) 10FeMCO_R1000_441.

After 2000 h at 750 °C, the different behaviours between the coated steels became even more clear.

All the coatings surfaces on Crofer 22 APU did not change much compared to after 1000 h of oxidation, except for the 5FeMCO (Figure 3.20 c), on which some roundish crystals appeared (with a composition in wt.% of: Cr=10-11, Mn=25-26, Co=28-29, Fe=5-6).

As previously done, the surface porosity was calculated for the Crofer 22 APU samples and reported in Table 3.8: since the variation from 1000 h aging is negligible, considering the surface morphology, it can be concluded that the coatings on this steel are stable even in the Cr-rich atmosphere inside the furnace.

Table 3.8: Surface porosity and doping/sintering effect of 2000 h aged Crofer 22 APU samples. Comparison with 1000 h aged samples.

Steel	Coating	Average porosity %	Doping/sintering effect	Compared to 1000 h aging
Crofer 22 APU	MCO	16,7%	-	-0,9%
	5FeMCO	9,6%	-7,1%	+0,4%
	10FeMCO	7,1%	-9,6%	+1,9%
	10FeMCO_R1000	4,5%	-12,2%	+0,9%

The situation looks different when considering the coated AISI 441 samples.

Considering MCO_441 (Figure 3.20 b), it can be highlighted that the overall surface is covered by ca. 30 µm crystals (composition wt.%: Cr=19-22, Mn=22-26, Co=26-32), forming clusters (Figure 3.21 a) which are considered the responsible for the shimmering effect seen only on this kind of samples (Figure 3.21).

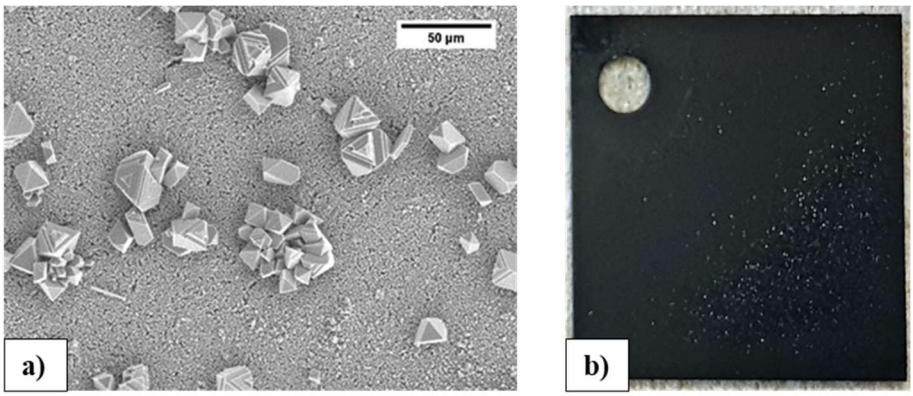

Figure 3.21: MCO_441 2000 h aged: a) SEM top view and
b) photo of the samples showing the shining effect

The 5FeMCO_441 is, then, covered by structures of the same shape, but with a maximum dimension of 5 µm.

As shown in Table 3.9, the Cr amount on the crystals is higher than on the coating; however, also on this one, Cr is ca. 8 wt.%: this could be due to condensation phenomena, during the cooling of the furnace of the chromium volatile compounds.

Table 3.9: EDS points compositions (wt.%)on 5FeMCO_441 surface after 2000h aging.

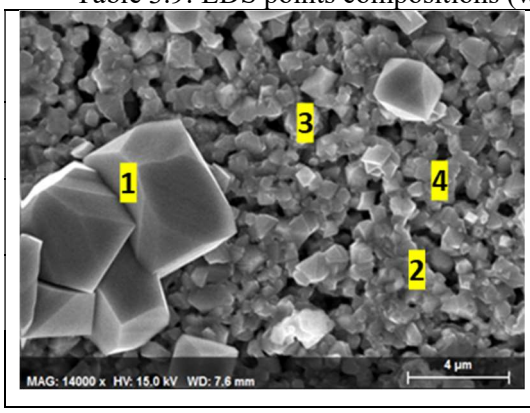

Point	O wt.%	Cr wt.%	Mn wt.%	Co wt.%	Fe wt.%
1	19,42	11,39	33,02	32,63	3,53
2	30,55	8,29	27,97	29,27	3,51
3	29,85	8,38	27,83	30,10	3,75
4	28,62	7,89	29,82	29,70	3,84

The most interesting cases are the one of 10FeMCO coating (Figure 3.20 a and b): here the superficial oxides have a more elongated shape, displayed in Figure 3.22.

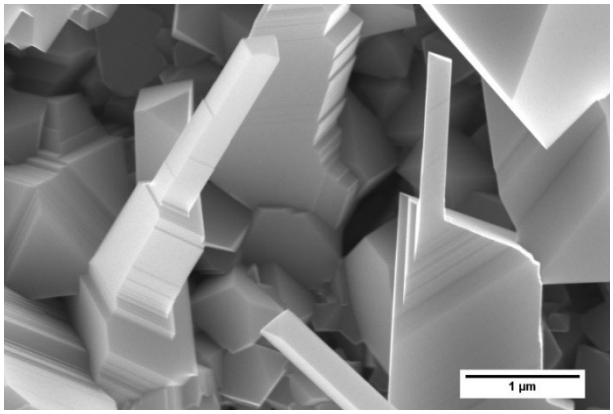

Figure 3.22: FE-SEM top view micrograph of 10FeMCO on AISI 441 after 1000 h aging.

The EDS investigation demonstrated that the Cr concentration on the coatings doped with 10% of Fe seems to be higher compared to MCO and 5FeMCO (whose values have been already reported): looking at Table 3.10, the chromium amount increased till 28 wt.%.

Table 3.10: EDS points on 10FeMCO_R1000 surface after 2000 h aging.

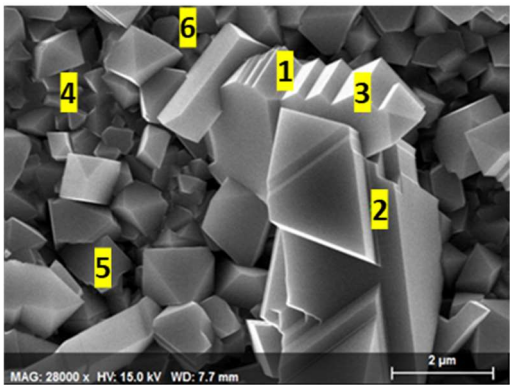

Point	O wt.%	Cr wt.%	Mn wt.%	Co wt.%	Fe wt.%	Ti wt.%
1	8,58	28,46	29,16	26,87	5,82	1,11
2	32,33	18,69	20,70	23,36	4,66	0,26
3	26,63	20,66	22,66	24,85	4,82	0,38
4	23,66	16,53	27,52	25,54	6,07	0,68
5	21,44	23,10	23,35	26,11	5,40	0,60
6	1,07	28,27	35,18	27,43	6,41	1,64

The comprehension of such a remarkable gap is currently a non-clear subject; since these two samples were one next to the other in the furnace, this cannot be due to a furnace charge effect.

Comparing 5FeMCO (Table 3.9) and 10FeMCO (Table 3.10), at least two points need to be highlighted: in the former, the Fe amount in the surface is always less than 4 wt.% and no titanium was detected; on the other hand, in 10FeMCO sample iron is included between 4,6 and 6,4 wt.%. Ti was detected as well and it is present in a greater quantity exactly were more Cr was recorded (the same trend seems to be valid also for Fe).

In Figure 3.23, FE-SEM cross section images of the same samples aged for 2000 h are reported.

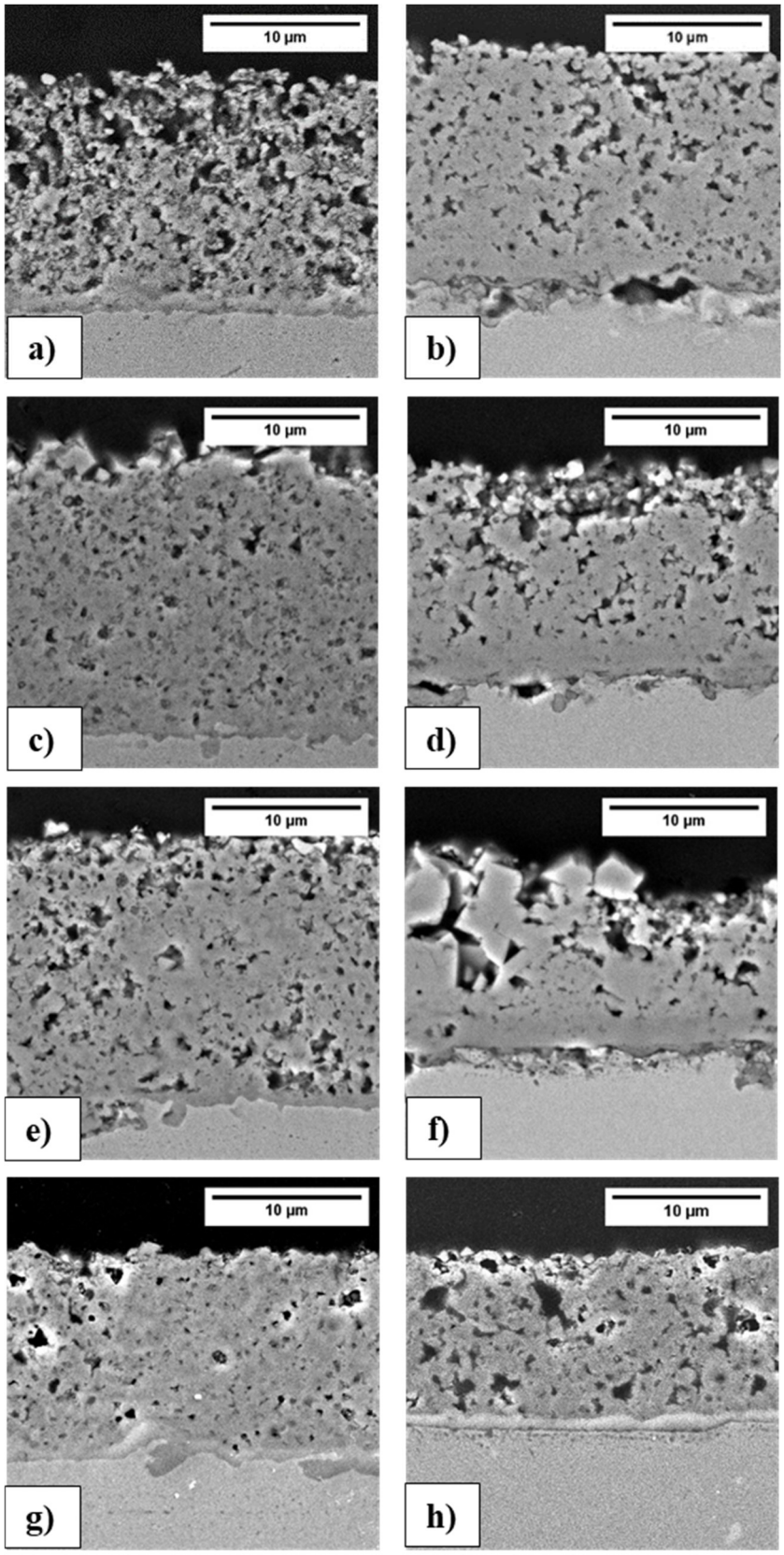

Figure 3.23: FE-SEM cross section images of the 2000 h aged samples, HE-SE2:
a) MCO_C22A, b) MCO_441, c) 5FeMCO_C22A, d) 5FeMCO_441, e) 10FeMCO_C22A, f) 10fEMCO_441, g) 10FeMCO_R1000_C22A, h) 10FeMCO_R1000_441.

Looking at the Crofer 22 APU samples (Figure 3.23 left column), one can note that the pores seem to be closed, especially for the doped samples, meaning that during the second phase of oxidation they reacted with the atmosphere, even if almost no Cr-rich oxides were seen on the surfaces.

This is also confirmed by the further decrease in porosity, compared to 1000 h aged samples (shown in the last column of Table 3.11).

Comparing cross section images between 1000 h (Figure 3.15) and 2000 h (Figure 3.23), it can be concluded that Crofer 22 APU samples looked quite similar to AISI 441 ones (even if these still showed a different interaction with the steel, as already described).

The uniformity in the behaviour of the coated steels is also proved Table 3.11: the final average porosity is almost the same for every couple of coatings and the trend related to the doping and sintering effect is very similar too.

In the last column in Table 3.11 it is highlighted that the densification of the undoped MCO and of the 10FeMCO_R1000 practically did not change compared to 1000 h aging, whereas the 5FeMCO and the 10FeMCO still reacted considerably.

Table 3.11: Porosity and doping/sintering effect on densification after 2000 h aging at 750 °C.

Steel	Coating	Av. porosity %	Std. Dev. 3 images	Doping /sintering effect on porosity	Compared to 1000 h aged
AISI 441	MCO	11,1%	4,7%	-	-0%
	5FeMCO	9,1%	4,2%	-2,0%	-3%
	10FeMCO	4,3%	0,5%	-6,8%	-9%
	10FeMCO_R1000	3,0%	1,6%	-8,1%	-0%
Crofer 22 APU	MCO	10,4%	3,3%	-	-6%
	5FeMCO	7,0%	3,5%	-3,4%	-15%
	10FeMCO	5,4%	1,2%	-5,0%	-4%
	10FeMCO_R1000	3,8%	0,6%	-6,6%	-2%

The two EDS line scans proposed in Figure 3.24, both related to the undoped MCO coating, are representative for the oxidation behaviour of the two steels.

For Crofer 22 APU (Figure 3.24 a) an oxide scale of less than 0,5 µm and a probable reaction layer of less than 1 µm are identified: even if it is difficult to measure the thickness of the two phases, the reaction layer can be identified by the higher Co signal in the Cr scale compared to the one of Mn.

Conversely, the Cr oxide on AISI 441 (Figure 3.24 b) measures ca. 2 µm and no reaction occurred between it and the coating.

The Fe and Cr amount inside the coating are negligible, even if the Cr signal is a bit higher for the 441 sample, both in the middle and at the surface of the coating.

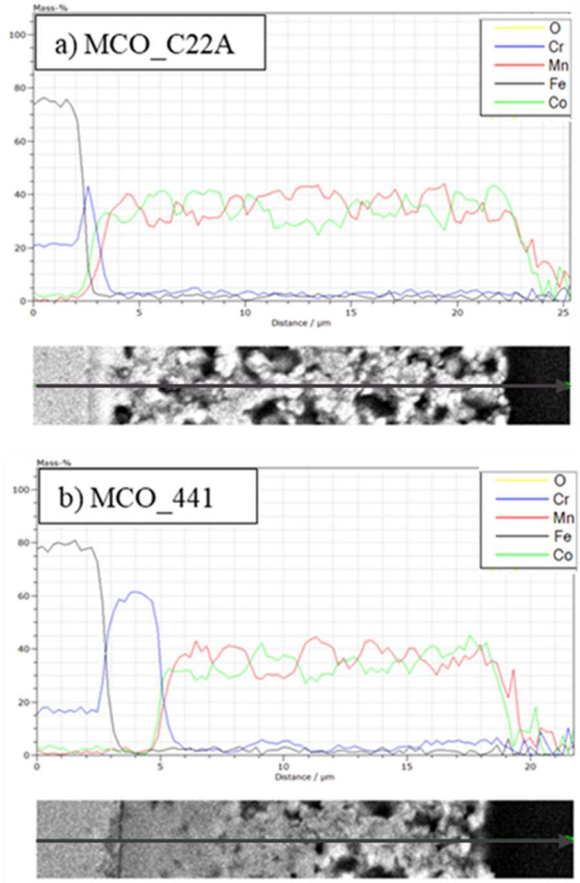

Figure 3.24: EDS line scans of 2000 h aged MCO coating on a) Crofer 22 APU and b) AISI 441.

As already remarked for the as sintered samples, in Figure 3.24 the Mn and Co lines exhibit fluctuation of the signals, which is likely to reproduce the one of the cubic and tetragonal spinels.

This effect is not present in Figure 3.25, which shows an example of the cross sections composition of the 10% Fe doped coatings on both steels.

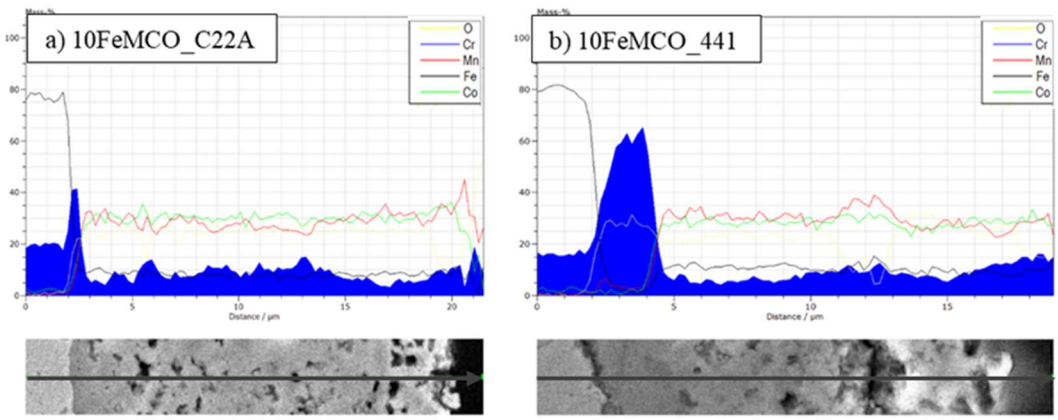

Figure 3.25: EDS line scans of 2000 h aged 10FeMCO coating on a) Crofer 22 APU and b) AISI 441.

As depicted in Figure 3.25 a, Crofer 22 APU formed an oxide scale of 0,5 µm (comparable to the one already discussed for the MCO coating in Figure 3.24) but no reaction layer; in the central part of the coating chromium was detected, reaching the maximum concentration (ca. 15 wt.%) in two points

corresponding to some pores, as pointed out by the arrows: this could suggest that the element entered the porosities from the surface and deposited there.

On the contrary, the AISI 441 formed a 2 µm oxide scale, but the Cr profile reaches the peak toward surface, where formed the spinels reacting with the coating (see Figure 3.20).

Moreover, the Fe line for Crofer 22 APU is stable, not overcoming the 10% set by the EPD suspension, while it is going up till 13-15 wt.% for AISI 441, probably because of some diffusion phenomena occurred during oxidation.

Finally, comparing Figure 3.24 and Figure 3.25, one can note that the oxide scale thickness in not really depending on the doped/undoped coating, but it is much more related to the substrate properties; however the characterization of the ARS_LSM samples, aged for 3200 h will shed light on these mechanism or will give a clear picture of the phenomenon.

For completeness of information, Figure 3.26 is presenting the EDS evidences for the 5FeMCO coating.

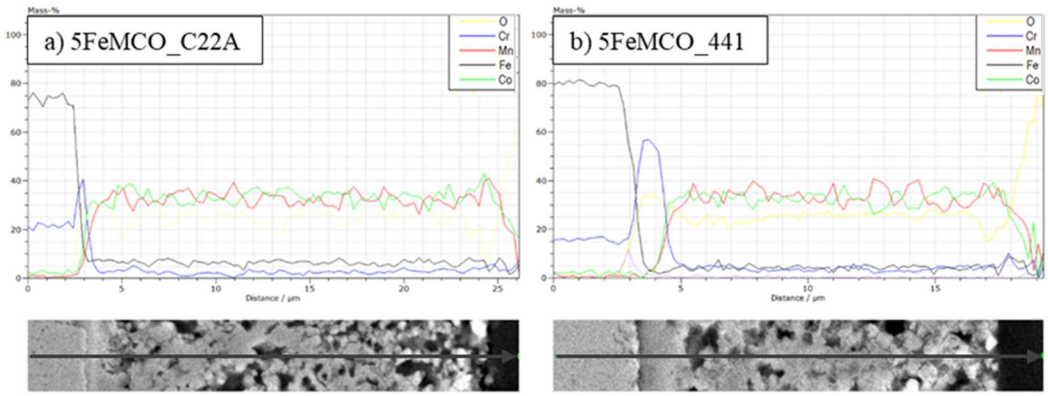

Figure 3.26: EDS line scans of 2000 h aged 5FeMCO coating on a) Crofer 22 APU and b) AISI 441.

Figure 3.26 highlights the different amount of chromium in the Crofer 22 APU samples, the narrow fluctuation of the Mn and Co signal (the behaviour of 5FeMCO is placed in the middle between MCO and 10FeMCO), and, most of all, the peak of Ti oxide under the oxide scale in the AISI 441 sample.

All discussed data in this section can be summarised as follows:

- A chromium contamination of the furnace atmosphere took place; it partly modified the mass gain and porosity measurements, as well as the oxidation mechanisms;
- Surfaces of Crofer 22 APU coated samples did not react markedly with Cr, which was detected only in some parts inside the coatings, since it entered and migrated through the porosity;
- On the AISI 441 surface Cr-Mn-Co-Fe mixed spinel were detected. The different dimensions and shapes of those crystals suggested that there was a kind of selectivity on the reaction mechanisms depending on the coatings composition. The growth of these surface species is responsible for the deviation from the parabolic oxidation behaviour of AISI 441 specimens;
- Not considering the Cr contamination, the mass gain values would have been lower than the measured ones, especially for the AISI 441 samples;
- The oxide scale growing seems not to be related to the coating doping. For Crofer 22 APU it measured ca. 0,5 µm after 1000 h and 0,8 µm after 2000 h, whereas for AISI 441 it went from 1,5 µm to 2 µm;
- There are some signs of the initial formation of the RL by Co diffusion toward the Cr oxide scale for samples of coated Crofer 22 APU.

3.2.2. Surface reactivity and chromium absorption

Considering the results from the microscopy investigation, it is clear that the coated Crofer 22 APU and AISI 441, although showing quite the same level of porosity, had a different interaction with the atmosphere. Indeed, AISI 441 samples contained not only much chromium through the coating, but were also covered by Cr-spinels, in different dimensions and shapes depending on the kind of coating.

Few studies already reported on the oxidation behaviour of AISI 441.

In [51] the authors found a deviation from the parabolic oxidation for the MCO coated steel.

Moreover in [92], they stated that the chromium evaporation from the MCO coated AISI 441 was higher than from bare one, speculating about the potential effect of manganese cobalt spinel toward oxygen adsorption and reduction.

In this regard, the possible reactions would be:

$$\frac{1}{2}O_{2(ads)} + H_2O + 2e^- \rightarrow 2OH^-$$

$$\frac{1}{2}Cr_2O_{3(s)} + \frac{1}{4}O_{2(g)} \rightarrow CrO_2^{2+} + 2e^-$$

Some researches about MCO as a catalyst have already been presented in [135] and [136].

In this study, the MCO_441 showed few but large (ca. 30 µm) Cr-spinels on the surface. By contrast, on the Fe doped coatings, many smaller (ca. 5 µm) crystals were seen.

This evidence could suggest that Fe promotes the nucleation instead of the growth of those species. To support this hypothesis, in [33], they already found that by increasing the amount of Fe-doping of MCO the BET area increases as well.

Even if it is not clear how the Fe acts, it could be supposed that the Fe addition in the spinel structure causes defects such as lattice distortions, lattice defects, oxygen vacancies, which represents sites with enhanced reactivity. As shown in the EDS analysis, it seems that the Fe-doping has some effect in the reduction of the size of the cubic/tetragonal grains of the coating: this inevitably leads to the increase of the grain boundary area, where defects can accumulate, and which constitutes a favoured path for ions diffusion.

In this regard, the Fe-Mn-Co spinels have already been studied for they catalytic activity toward oxygen reduction ([137], [138], [80]).

Apart from the iron in the spinel, the other elements in the AISI 441 alloy (Ti, Si, Al), diffusing outward, could have some effects on the coating reactivity as well.

On the other hand, the same reactivity was not observed on the Crofer 22 APU, even coupled with the Fe-doped coating. This was read as the sign that the composition of this alloy (higher Cr and Mn amount, La, narrow tolerance on impurities) ensures better stability and limits the migration of ionic species from the inside.

In any case, the surface reactivity toward the formation of the Cr-spinels could also be considered an advantage: if the coating is proved to capture the volatile Cr-species, this could reduce the issue of the cathode poisoning.

3.3.ASR: comparison between the “in situ” and “ex situ” methods

ASR_LSM

Figure 3.27 and Figure 3.28 show the ASR behaviour for the Crofer 22 APU and AISI 441 samples respectively, up to 3200 h at 750° C under a current density of 0,5 Acm^{-2}.

Since no significant difference among the two measurements of the two surfaces of each sample was recorded (i.e. there is no signal that the ASR has been influenced by the direction of the current), the average ASR value between the two of them is proposed (apart from MCO_441 where one connection was accidentally detached).

It is reminded that no thermal cycling was performed.

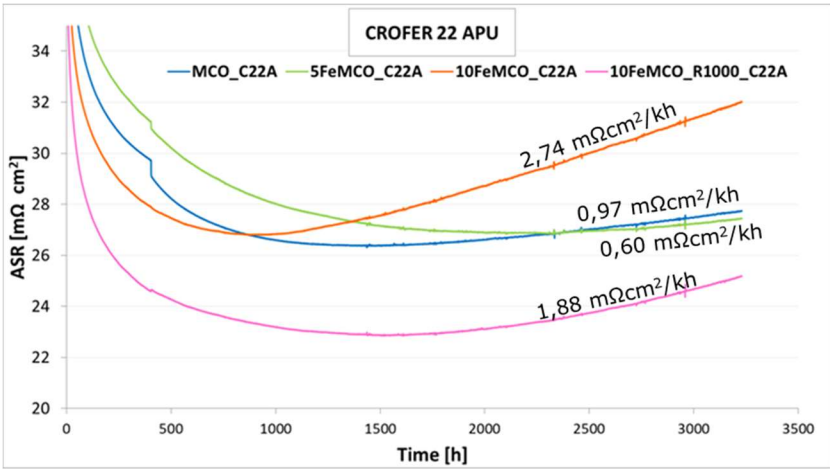

Figure 3.27: ASR_LSM for coated Crofer 22 APU samples, measured at 750 °C for 3200 h under a current density of 0,5 Acm^{-2}.

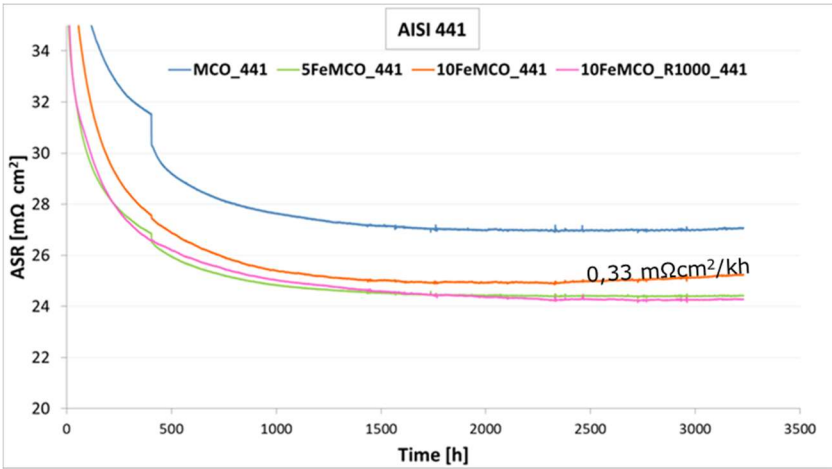

Figure 3.28: ASR_LSM for coated AISI 441 samples, measured at 750 °C for 3200 h under a current density of 0,5 Acm^{-2}.

In both Figure 3.27 and Figure 3.28, the first part of each line, approximately till 1000 °C aging, shows a decreasing trend of resistance, due to the sintering of the LSM plates used as contacts.

The hop visible at around 400 h for almost every samples is due to thermal adjustment of the furnace.

The ASR values at the end of the 3200 hours aging are reported in Table 3.12.

Table 3.12: ASR_LSM values after 3200 h at 750 °C in air.

ASR after 3200 h [mΩ cm^2]				
	MCO	5FeMCO	10FeMCO	10FeMCO_R1000
Crofer 22 APU	≈27,8	≈27,5	≈32,0	≈25,2
AISI 441	≈27,0	≈24,5	≈25,3	≈24,3

As it ca be seen all the values are in the same range, fluctuating from 24,3 to 32,0 mΩcm^2 and no direct conclusion of the effect of the Fe-doping, as well as the different behaviour of the two steels can be done at this point, or from these data.

It is quite tricky to compare these results with those of the literature because of the mismatch regarding the temperature calibration and the method of the test, as well as the substrate and coating materials. Moreover, even if when the experiment is run at the same conditions, the greater effect of the LSM sintering cause a relevant scattering of data.

In [134] the authors found out that the ASR of MCO coating (30-50 µm thick) on Crofer 22 APU, after 5000 h at 750 °C, was between 15 and 20 mΩcm^2 ;they also measured a very close ASR value of the bare Crofer 22 APU. In [19] the authors verify that after 2500 h at 800 °C the MCO coated Crofer 22 APU showed an ASR of 20 mΩcm^2, the uncoated steel of 30 mΩcm^2, instead.

Concerning the Fe doping, in [65] it was checked that after 4370 h at 800 °C, there was no significant difference in the ASR considering the undoped and Fe-doped MCO (ca. 15 mΩcm^2), but the one of the bare Crofer 22 APU was 50 mΩcm^2.

On the basis of literature results, it can therefore be assumed that the values found in our work are reasonable.

Figure 3.27: ASR_LSM for coated Crofer 22 APU samples, Figure 3.27 and Figure 3.28 highlight that the main difference between the two steels behaviour is that starting from 1000-1500 h, all the Crofer 22 APU started increasing, while those of ASI 441 remained stable till the end of the test.

From the slope of the curves, it was therefore possible to calculate the linear degradation rate, intended as the increase in area specific resistance over 1000 h [mΩcm^2/kh]; their values are reported in Table 3.13, together with the estimation of the ASR values after 40 000 h, obtained by making an extrapolation of the linear degradation rates.

Table 3.13: Degradation rate and extrapolated ASR at 40 000 h values for Crofer 22 APU samples.

Crofer 22 APU	**MCO**	**5FeMCO**	**10FeMCO**	**10FeMCO_R1000**
Linear degradation rate [mΩcm^2/kh].	0,97	0,60	1,88	2,74
ASR at 40 000 h [mΩcm^2]	63,5	49,6	101,2	126,0

From Table 3.13, it could therefore be deduced that after 40 000 h, the coatings doped with 10 wt.% of Fe would excess the upper limit for the interconnect of 100 mΩcm^2.

However, it must be specified that the data of ASR at 40 000 are to be considered the worst-case scenario: in fact, the strength of the interconnect, directly connected to the thickening of the oxide scale, has already been proved to be parabolic or sub-parabolic [65], i.e. at some point, the degradation rate should decrease till reaching a new steady state.

Moreover, assuming that the ASR of AISI 441 samples would always remain stable is an unrealistic assumption. Indeed these samples may subsequently be affected by degradation mechanisms with kinetics not yet activated, but, mostly, the AISI 441 has already proved to be very sensitive to thermal cycling due to the weak steel/coating interface and the different CTE of the present layers [102]; concerning this point, please refer to the microstructural analysis in 3.3.1.

In Table 3.14 the activation energies for the conduction, calculated in the linear regime (between 750-450 °C) are reported.

Table 3.14: Activation energy [kJ mol^{-1}] calculated between 750 and 450 °C, from ASR_LSM samples after 3200 h at 750 °C in air.

Activation energy, E_A [kJ mol^{-1}]				
	MCO	5FeMCO	10FeMCO	10FeMCO_R1000
Crofer 22 APU	66	62	65	64
AISI 441	62	61	58	58

The activation energies are quite similar as for the ASR values, and no clear trends can be deduced by them. Anyway, in [65] very close E_A where obtained, both regarding the undoped MCO and the Fe-doped cases.

Since the measured ASR is a function of the oxide scale and RL thickness, please refer to Section 3.3.1 for the results concerning the microstructural evolution of the discussed samples.

ASR_Pt

In Figure 3.29 and Figure 3.30 the results obtained by ASR_Pt (points, squares, triangles) are overlapped by those of ASR_LSM, respectively for Crofer 22 APU and AISI 441. The dotes refer to the bare steels (the bare AISI 441 samples was preoxidized for 2 hour at 900 °C before aging).

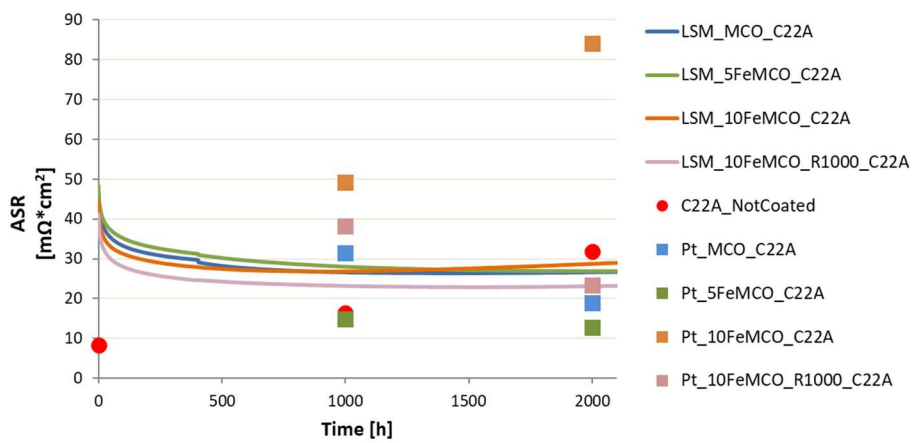

Figure 3.29: Comparison between ASR_LSM (lines) and ASR_Pt (squares and circles), measured on 1000 and 2000 h aged samples of Crofer 22 APU (750 °C, 0,5 Acm^{-2}).

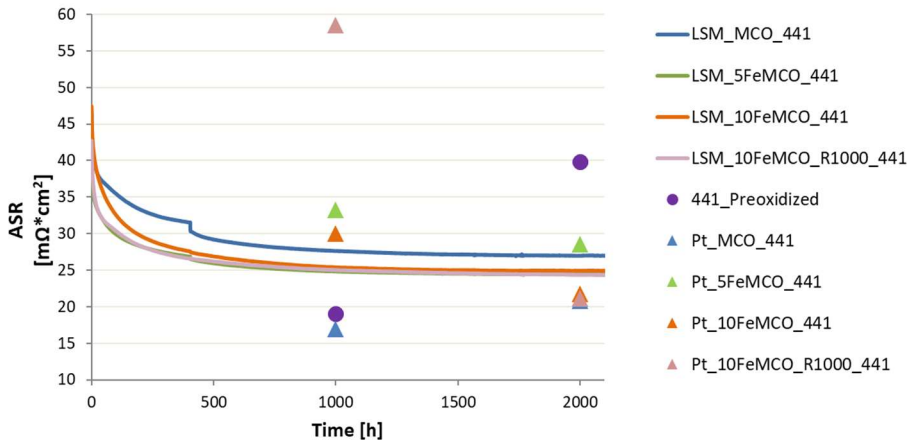

Figure 3.30:Comparison between ASR_LSM (lines) and ASR_Pt (squares and circles), measured on 1000 and 2000 h aged samples of AISI 441.

Looking at the results, it is clear that both finding a trend over the kinds of coatings and an obvious relation between the two different methods is tough.

As expected, the bare steels used as references both show an increasing ASR between 1000 and 2000 h aging, in line with the thickening of the oxide scale.

By contrast, all the data of the coated samples exhibited quite a high scattering, even if the values of the 2000 h aged samples are generally closer to the ones obtained in ASR_LSM.

In order to get an accurate comparison between the two methods, many factors should be taken into account.

- First of all, the contribution of the LSM contact to the ASR: to calculate it, simply subtracting its it hypothetical ASR value is not sufficient, because, as already explained, during the aging at high temperature LSM and coating react.
- Secondly, many issues are caused by the definition of the contact area: in fact, as shown in Section 3.2.1, the growth of crystals, as well as the difference in surface porosity have meant that the difference between real and nominal area was very marked.
- It should be kept in mind that the electric resistance of the Cr-containing spinels is higher than that of the MCO. Moreover, the results can easily be affected by experimental errors, due to samples misalignment in the rig.

In Table 3.15 the activation energies calculated during the cooling of the ASR_Pt rig are presented; for these calculations the linear range was recorded only till 600 °C.

Table 3.15: Activation energies calculated from ASR_Pt, between 750 and 600 °C.

Activation energy, E_A [kJ mol^{-1}]				
Steel	**Coating**	**1000 h**	**2000 h**	**Δ**
CROFER 22 APU	MCO	33,2	30,4	-8,8%
	5FeMCO	48,6	50,5	+3,8%
	10FeMCO	43,8	38,5	-12,9%
	10FeMCO_R1000	48,3	43,3	-10,9%
AISI 441	MCO	35,2	37,6	+6,6%
	5FeMCO	42,2	31,2	-30,0%
	10FeMCO	42,3	32,5	-26,2%
	10FeMCO_R1000	46,4	42,0	-10,0%

Also, in this case there is quite a high scatter between the results, without a regular trend.

Moreover, the values are lower than those measured by ARS_LSM maybe because of the lack, in this case, of the LSM contribution to them.

In Figure 3.31 the ASR_Pt values are plotted by the mass gain measured for each sample.

Only the bare steels showed the trend suggested in [132] about the increasing of the two parameters over time; for all the coated samples (in semi-transparent colour) the information is conflicting.

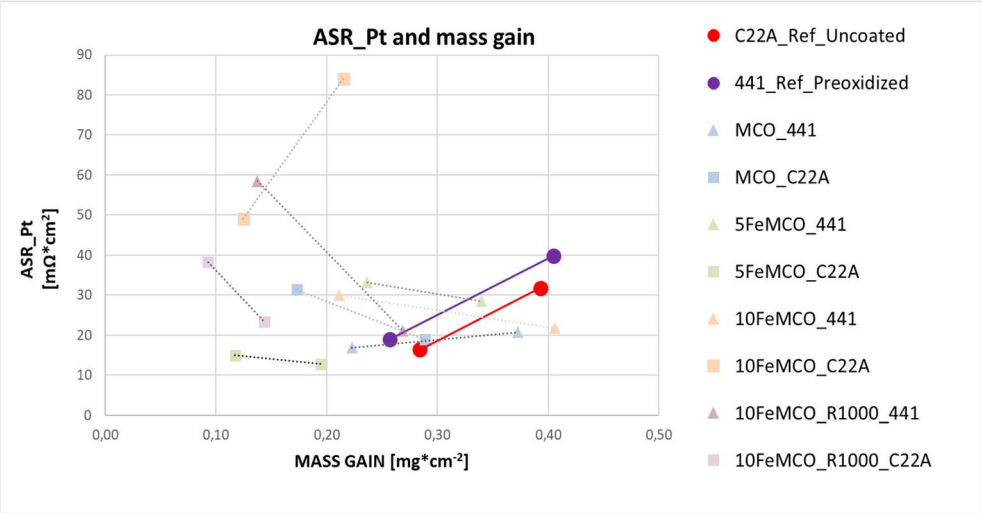

Figure 3.31: ASR_Pt measured at 750 °C and mass gain of 1000 and 2000 h aged samples.

Considering all the discusses points, this "ex-situ" ASR measurement is not believed to be a suitable characterization method for the coated samples, unless a very large number of samples are tested, in order to derive a statistic.

However, it could prove to be an advantageous approach when evaluating the conductivity or electrical insulation of a new material in an approximate way.

3.3.1. Microstructural investigation of the 3200 h aged samples

Figure 3.32 is showing the FE-SEM cross section images of each studied coating/steel couple, after 3200 h at 750°C in air of ASR_LSM measurement (backscattered electrons). In Figure 3.32 a and b, the LSM plates used as contacts can be seen, too.

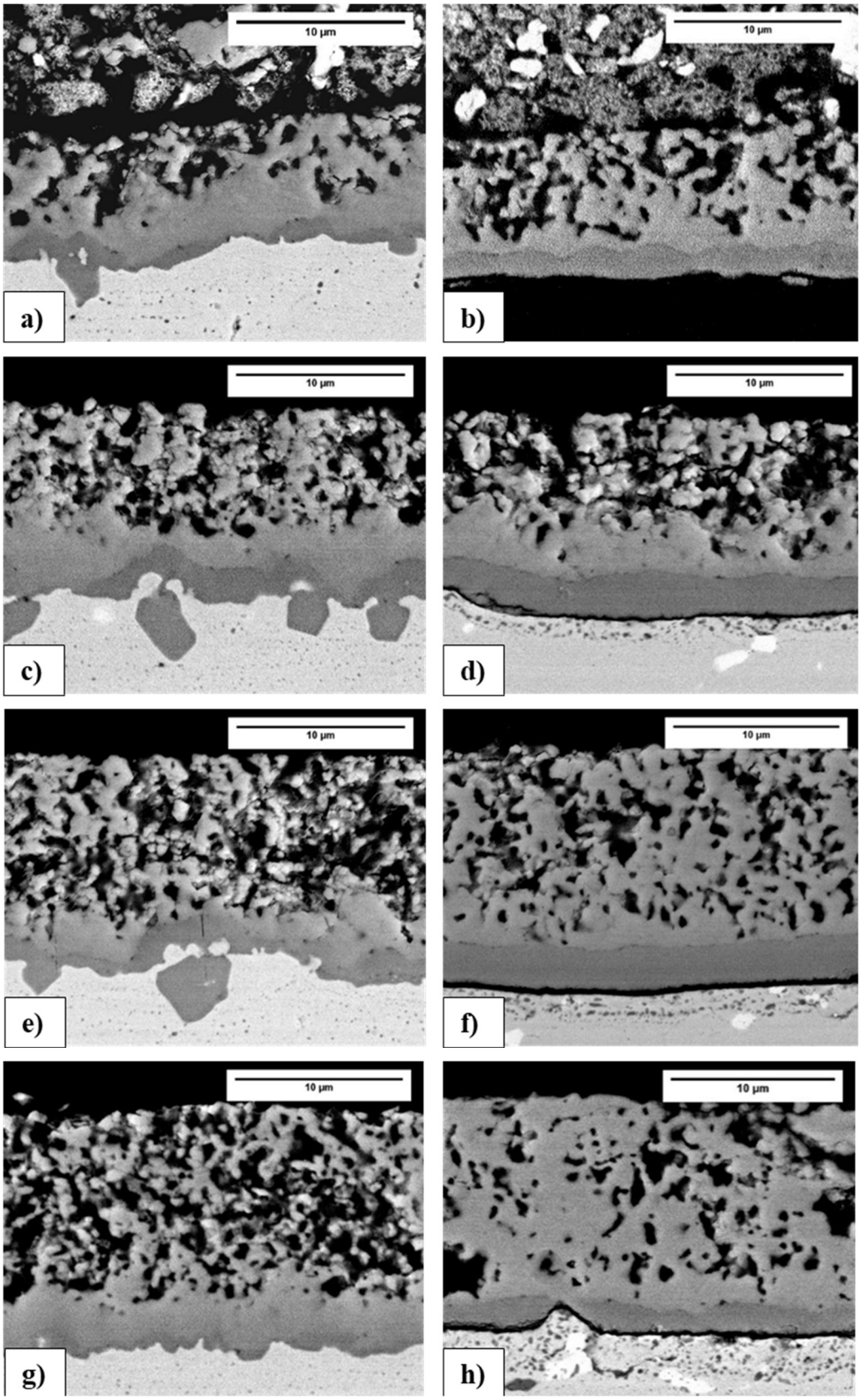

Figure 3.32: FE-SEM cross section images of ASR_LSM samples, after 3200 h at 750°C (air, 0,5 Acm^{-2}): a) MCO_C22A, b) MCO_441, c) 5FeMCO_C22A, d) 5FeMCO_441, e) 10FeMCO_C22A, f) 10fEMCO_441, g) 10FeMCO_R1000_C22A, h) 10FeMCO_R1000_441.

All the coatings on Crofer 22 APU exhibited a good interface with the substrate, meaning that no delamination occurred; contrariwise the samples of AISI 441 showed cracks, indeed in Figure 3.32 b, the MCO coating is completely separated from the steel.

This kind of cracks are likely to be due to thermal stress, occurred at the interface during the cooling of the furnace.

Furthermore, the morphology of the separation line between the coating and the steel is quite the distinct for Crofer 22 APU and AISI 441: in the first case it is uneven, with many Mn-Cr oxides formations under the surface, in the second, in it a straight line. Then, the area next to the surface of AII 441 is presenting many irregularities.

Comparing the cross section of Figure 3.32 with those of 1000 and 2000 h aged from oxidation resistance, a different morphology is evident: all coatings of ASR presented a dense layer in the inner zone, followed by a wider one with high porosity.

In Table 3.16, both the dense zone thicknesses and the porosity value are reported. Concerning the second one, it was calculated considering the total coating thickness (without subtracting the dense zone one), so that is was possible to compare it to the previously discussed samples.

Each value in Table 3.16 is the average obtained by measurements on four SEM images for each kind of sample: two were taken from the bottom, where the "down" connection of the ASR set-up was, and two from the other one ("up" connection)., The total thickness was measured for every samples as well.

The two steels followed different trends: indeed, for AISI 441 samples it decreased till the same value for 5% and 10% doped MCO; the lowest value was found to be for the 10FeMCO_R1000 coating; on Crofer 22 APU, the MCO doping with Fe caused on increasing of porosity for 5FeMCO and 10FeMCO.

Table 3.16: average porosity and dense zone thickness of samples for ASR_LSM after 3200 h.

Steel	**Coating**	Av. porosity %	Doping /sintering effect on porosity	Compared to 2000 h aged	Compared to as sintered	Dense zone thickness [µm]
AISI 441	MCO	19,5%	-	+8%	-5%	2,4
	5FeMCO	15%	-4,5%	+6%	-16%	3,0
	10FeMCO	15,8%	-3,7%	+11%	-13%	2,9
	10FeMCO_R1000	9%	-10,5%	+6%	-11%	2,4
Crofer 22 APU	MCO	14,8%	-	+4%	-13%	2,7
	5FeMCO	16,8%	+2,0%	+10%	-10%	3,9
	10FeMCO	20,2%	+5,4%	+15%	-4%	3,4
	10FeMCO_R1000	14,9%	+0,1%	+11%	-3%	3,3

As it can be deduced from Table 3.16, the densification of these samples is lower compared to the ones from oxidation resistance test of 4-15%, proving in certain way that, in that case, the chromium contamination modified or influenced the results.

Linking the results with the as sintered samples instead, one can check that porosity decreasing after 3200 h for AISI 441 samples was higher for the Fe-doped samples (without following a trend related to doping amount/sintering), while the doped coatings on Crofer 22 APU densified less that the undoped MCO, especially the ones doped with 10% of Fe.

Shifting the attention to the last column of Table 3.16, one can see that all the dense zone thicknesses are included between 2,4 and 3,9 µm.

Plotting these values as a percentage of the total coating thickness, as shown in Figure 3.33, turned out being a more interesting approach.

Indeed, it revealed that for both the substrates the iron doping and the reduction at 1000 °C, instead of 900 °C, progressively reduced the relative width of the dense layer.

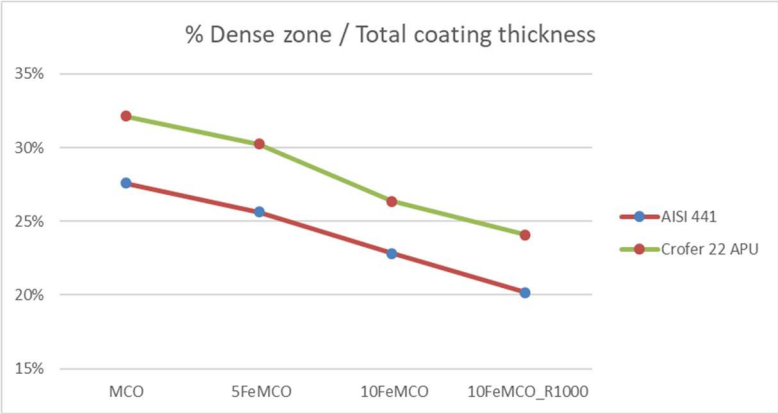

Figure 3.33: Percentage of dense area compared to total thickness, for all studied samples from ASR_LSM after 3200 h.

However, it is worth to highlight that the hypothesis following the analysis in Figure 3.33 is that the densification of the inner coating layer is influenced by the overall depth: considering that the process needs oxygen and ions migration to happen, this idea can be considered realistic, at least in the first instance.

Furthermore, again from Figure 3.33, it can be seen that the Crofer 22 APU line is always above the one of AISI 441; by focusing on the EDS evidences, more information about it can be discovered.

Figure 3.34 is showing the EDS map of the undoped MCO on Crofer 22 APU. The Cr oxide scale is not uniform, making it is tough to define its actual thickness; moreover, especially where it is thinner the reaction layer can be seen, formed by the inter-diffusion of Co and Cr (orange arrows).

Looking at the oxygen map, it can be also noted that the element signal is stronger at the Cr_2O_3 formations, which are, not accidentally, just under the deeper pores.

At the lower left under the steel surface, a Cr-Mn spinel formation is visible, as well (blue arrows).

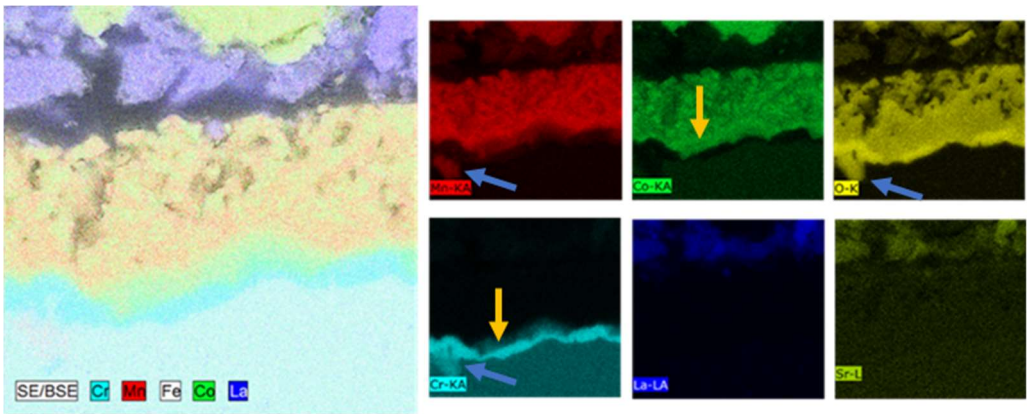

Figure 3.34: EDS map of MCO_C22A, from ASR_LSM after 3200 h.

The EDS map of the same MCO coating on AISI 44, shown in Figure 3.35, is quite distinct, instead.

Starting from the top (where no steel can be seen because of delamination), a thin (ca. 0,2 µm) but continuous silica layer followed by a smooth Cr oxide scale of 2 µm were detected. No reaction layer appeared.

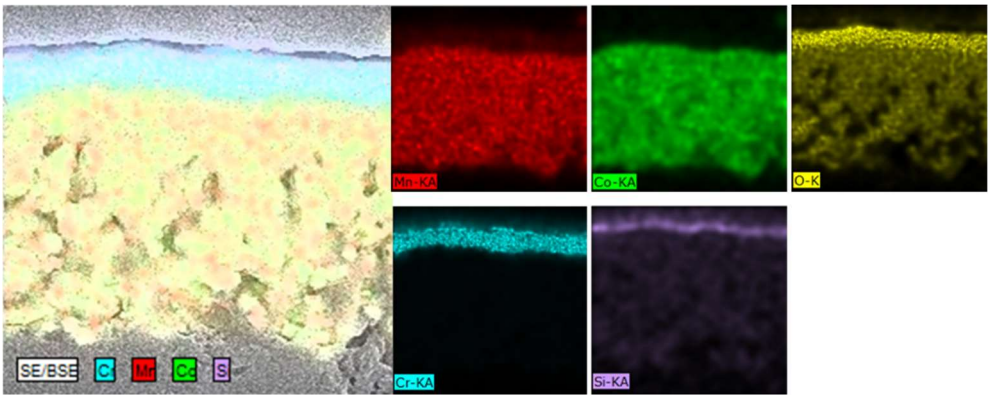

Figure 3.35: EDS map of MCO_441, from ASR_LSM after 3200 h.

The EDS map of Figure 3.35 displays that the coating detached from the substrate not at the Cr oxide interface, but at the silicon oxide one.

A similar situation happened to the 5FeMCO on AISI 441, therefore, in Figure 3.36 the map of the steel is presented: while, even near the surface, the quantity of Cr remains constant, the remarkable concentration of titanium oxides can be seen (together with a slight oxygen enrichment).

The Si signal is not showing any evidence of its presence and in the map of iron alone, some depletion areas can be seen, corresponding to the zone where Ti oxides are present.

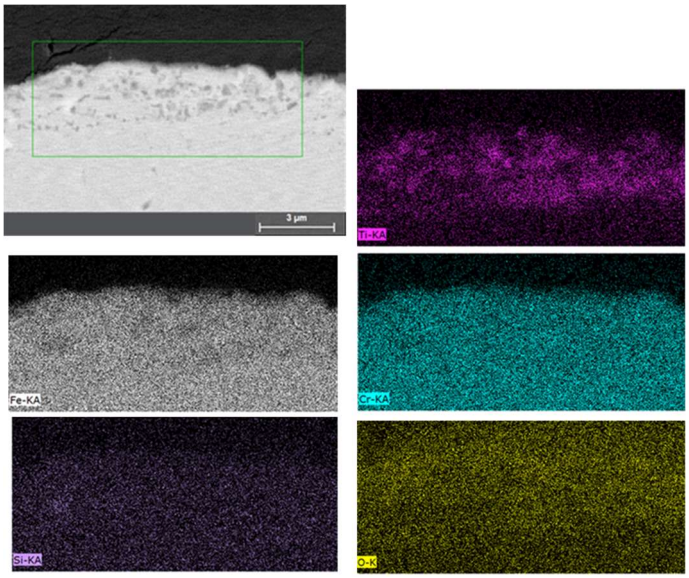

Figure 3.36: EDS map of AISI 441 under 5FeMCO coating from ASR_LSM.

Similar features can be verified in Figure 3.37, an EDS map of 10FeMCO_R1000 on AISI 441 (see Figure 3.32 h): a thick and constant Cr oxide scale, no reaction layer, a diffuse layer of Ti oxides beneath the steel surface are detected.

Moreover, Figure 3.37 is much relevant to identify the presence of the so called Laves phases in the steel, made by the reaction of Si and Nb. As already explained in the Introduction, this element is added to the alloy to block the Si diffusion; nevertheless, as in Figure 3.35, also here silica is forming almost a continuous layer between the steel and the chromia scale.

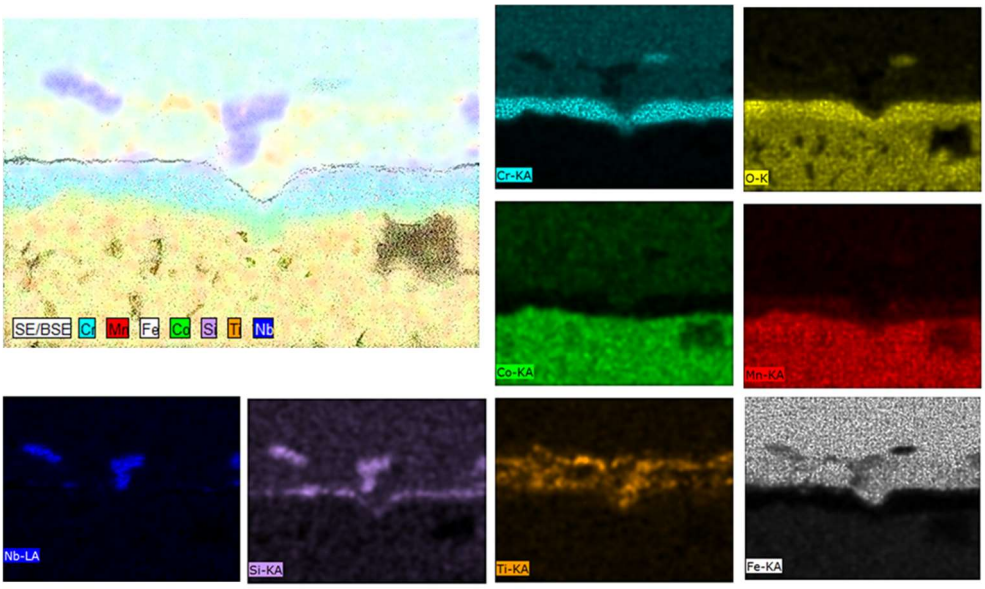

Figure 3.37: EDS map of 10FeMCO_R1000_441 after 3200 h of ASR measurement.

By comparing Figure 3.37 with AISI 441 SEM images from the oxidation test (3.2.1), it can be noted that after 2000 h at 750 °C, the silica layer, as well as the high concentration of Ti oxide were not present; this could suggest either that the kinetics relative to those element diffusion became more significant after 2000 h or that the already discussed issues occurred during the oxidation test (Cr contamination, cracks due to thermal cycling) considerably modified the oxidation parameters.

In any case, the Nb addition was proved not to be enough for avoiding the silica layer to form.

Finally, the EDS line scan on 10FeMCO_R1000_441 in Figure 3.38 shows a more clear resume of what has just been discussed, useful to better quantify and compare the presence of each element.

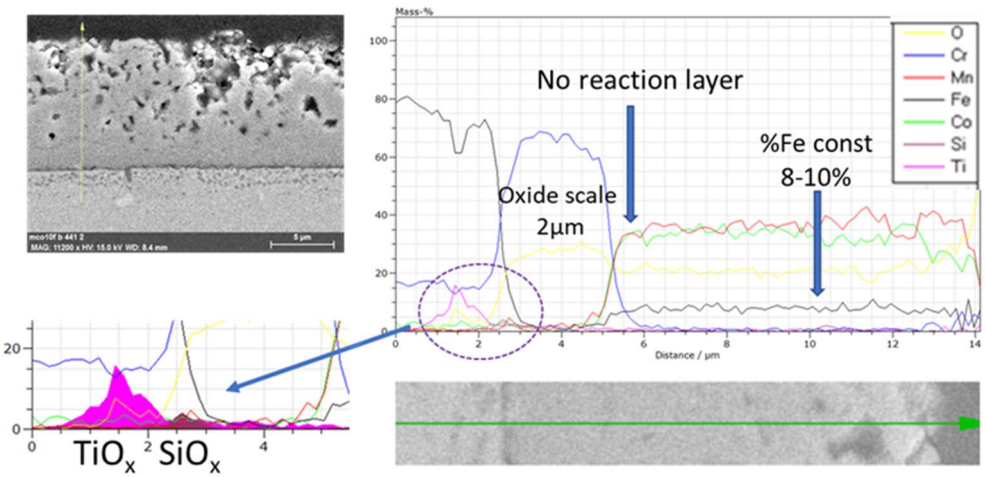

Figure 3.38: EDS line scan of 10FeMCO_R1000 on AISI 441, from ASR_LSM after 3200 h.

Figure 3.39 shows two examples of the possible interactions between Crofer 22 APU and the doped coatings.

To the left, the Cr oxide scale is almost not present, while the reaction layer is much more visible (it measures more than 2,5 µm); to the right, it is much thinner, but the oxide scale exceeds 1 µm.

In any case, by summing the width of the two zones, nearly the same value is obtained (≈3 µm).

Moreover, especially in the left image, a higher signal of the Mn line can be seen: this manganese enrichment of the coating is due to its diffusion from the LSM plate used as contact.

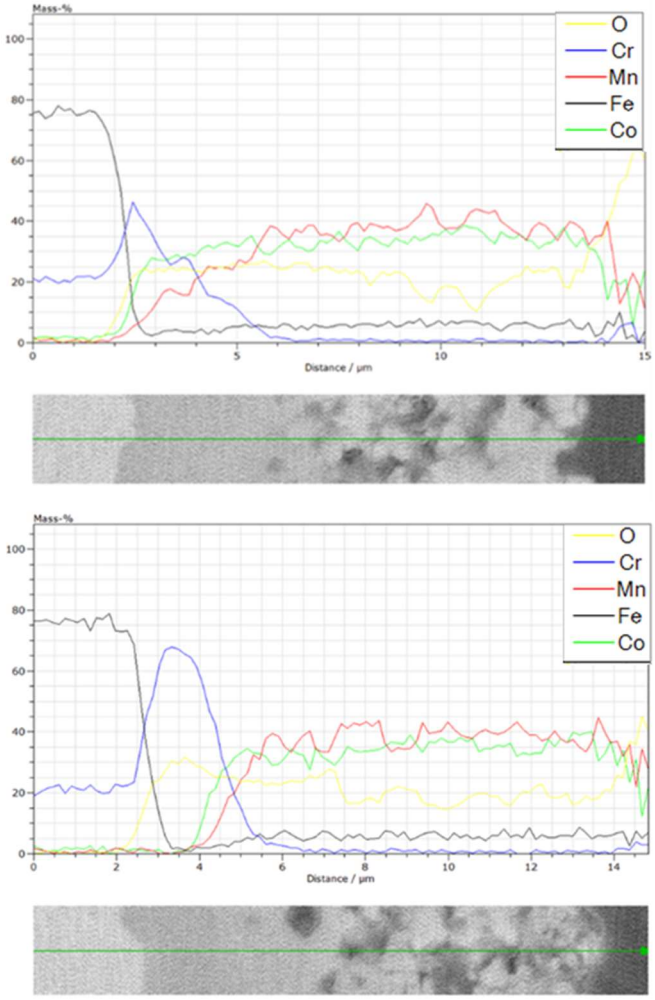

Figure 3.39: EDS line scans of different zones of 5FeMCO_C22A, from ASR_LSM after 3200 h.

Figure 3.39 shows the EDS line scans both taken from close areas of 5FeMCO_C22A (of Figure 3.32 c); the same behaviour is exhibited by 10FeMCO_C22A, as well.

The same 10% Fe-doped coating reduced at 1000 °C on Crofer 22 APU presented a slightly different cross section composition: as shown in Figure 3.40, the Cr oxide is narrow on the whole section and the thicker reaction layer is fairly homogeneously distributed.

This feature can be explained as following: as already discussed for Figure 3.34, the formation of the Cr_2O_3 scale requires more oxygen than the reaction layer, thus, since the densification of the 10FeMCO_R1000 was high already after the sintering, this prevented the O_2 diffusion and forced it to a winding way.

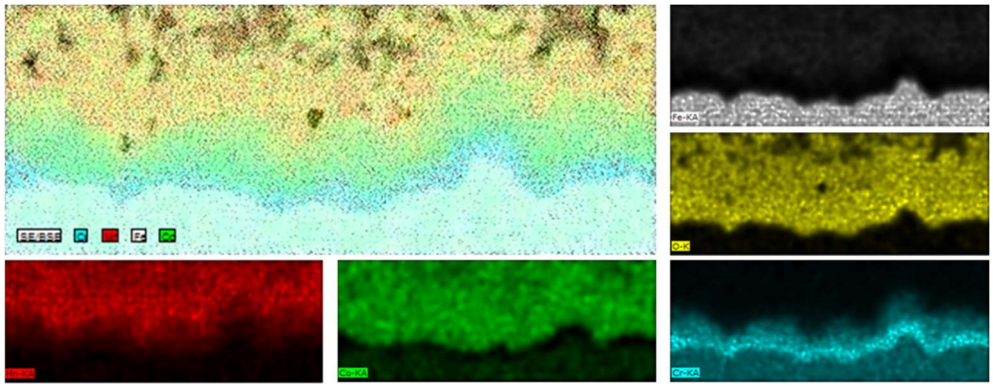

Figure 3.40: EDS map of the interface between 10FeMCO_R1000 and Crofer 22 APU, from ASR_LSM after 3200 h.

No chromium was detected inside any of the coatings, proving both the contamination of the oxidation furnace and the effectiveness of the deposited films toward Cr retention.

Focusing on all the different phases identified, in Table 3.17, all the data obtained thanks to EDS analysis are presented; these data are also compared to the dense zone length measured by FE-SEM micrographs. At least two EDS images were considered for every sample.

For the AISI 441 specimens, an overall 0,2 silica layer was fixed, since it resulted too thin to specify it in a more detailed way.

Considered the irregularity of the interfaces, for Crofer 22 APU samples, the values reported in the Cr oxide and reaction layer columns have to be considered as maximum ones, while the numbers written brackets are respectively the depth of the other component of the couple (e.g. Cr oxide thickness (+ reaction layer next to it)). Therefore, in the "Sum" column, the mathematical average between all of them is reported, since it was impossible to estimate the real surface fraction where each behaviour was prevailing.

Moreover, though in [58] a reduction of the reaction layer thickness thanks to Fe (or Ti) doping on $(MnCo)_3O_4$ was asserted, here the same result was not verified.

Table 3.17: Cr oxide, reaction layer and Si oxide thicknesses compared to the one of the dense zone.

Steel	Coating	Cr oxide [µm]	Reaction layer [µm]	Si oxide [µm]	Sum [µm]	Dense zone [µm]	Δ [µm]
AISI 441	MCO	2,2	NO	0,2	2,4	2,4	+0,0
	5FeMCO	2,5	NO	0,2	2,7	3,0	+0,3
	10FeMCO	2,1	NO	0,2	2,3	2,9	+0,6
	10FeMCO_R1000	2,0	NO	0,2	2,2	2,4	+0,2
Crofer 22 APU	MCO	1,4 (+1,0)	2,0(+0,5)	NO	2,4	2,7	+0,3
	5FeMCO	1,2 (+1,0)	2,2 (+0,3)	NO	2,3	3,9	+1,6
	10FeMCO	1,1(+0,7)	1,4 (+0,8)	NO	2,0	3,4	+1,4
	10FeMCO_R1000	1,1 (+0,8)	2,2 (+0,2)	NO	2,1	3,3	+1,2

While for the AISI 441 samples the Δ between the measured dense zone and the sum of the Cr_2O_3 and the silica layer is negligible, for the Fe-doped coatings on Crofer 22 APU there is about 1 µm that is

likely due to inner coating densification: this effect could prove that by matching Crofer 22 APU and doped MCO both high chromium retention and low oxygen inward diffusion are achieved, which is also confirmed by gravimetric analysis.

Finally, by plotting the oxide scale and reaction layer thickness as a percentage of the total one of the coatings (Figure 3.41), the opposite behaviours of the steel compared to Figure 3.33 can be appreciated.

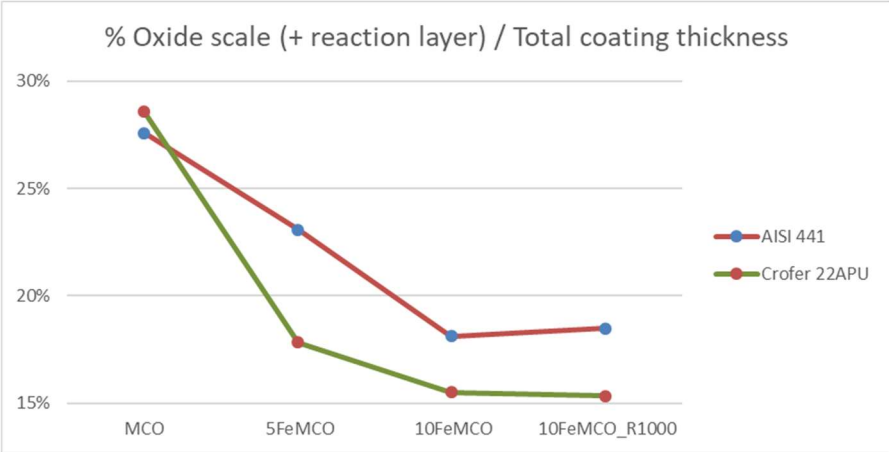

Figure 3.41: Oxide scale and reaction layer (by EDS) plotted as a percentage of the total coating thickness.

As reported in Figure 3.41, while the undoped coating exhibited the same trend on both steels, the doped ones reduced the relative amount of the considered layer, with the minimum result on Crofer 22 APU.

Summarizing the main points discussed in this section, it can be stated that:

- After 3200 h at 750 °C, all the coatings exhibited reasonable and very close ASR values;
- All the coated Crofer 22 APU samples showed an increasing resistance over time; the coatings doped with 10 wt.% Fe had the worst behaviour;
- The coated AISI 441 displayed a high ASR stability at constant temperature;
- The interfaces between Crofer 22 APU samples and the coating were found to be continuous;
- The reaction layer was seen only for Crofer 22 APU specimens: it was formed by the Co diffusion in the chromium scale and by the Cr diffusion toward the MCO coating.
  The sum of the RL and the oxide scale thickness can be approximated at ca. 2,2 µm. In addition to them, the Fe-doped MCO presented a denser layer (ca. 1 µm) at the bottom of the coating;
- AISI 441 exhibited very weak interfaces with the coatings, presenting cracks between the continuous silica layer and chromia scale. In this case, no reaction layer was detected and all the denser zone in contact with the steel was made of Cr_2O_3 (ca. 2,4 µm);

3.4.Oxidation mechanisms

As already discussed, the microscopic investigation of the 1000 and 2000 h aged samples did not allow to reveal a clear difference in the thickness of the oxide scale depending on the coating (doped/undoped); it was therefore only possible to indicate average values for the two studied steels.

In this regard, in Figure 3.42 the average values of the oxide scale thicknesses for Crofer 22 APU and AISI 441, measured by EDS after 1000, 2000 and 3200 h are plotted; the trendlines have been included as well, showing that the measurements are perfectly fitting a parabola.

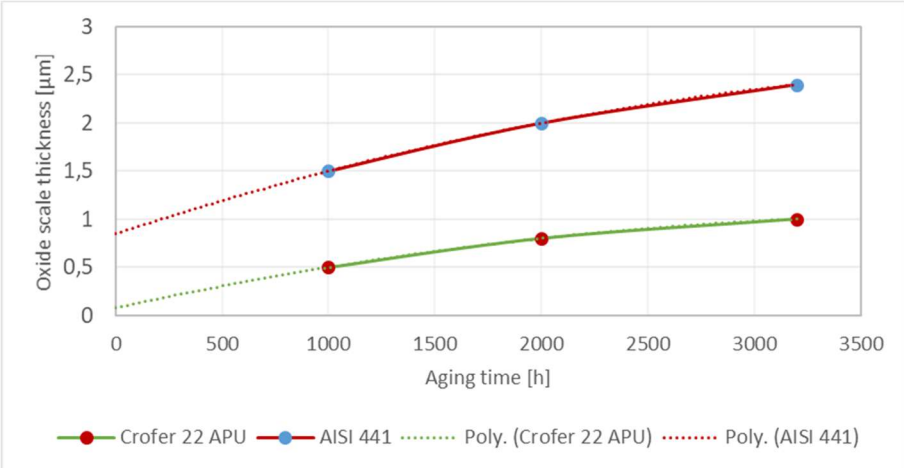

Figure 3.42: Average oxide scale thickness mesured by EDS for Crofer 22 APU and AISI 441 samples.

The growth of the oxide scale is governed by parabolic law for both steels, meaning that the rate limiting step for the oxidation behaviour is the diffusion of ionic species (metallic cations and oxygen ions) [51].

Thus, it is possible to calculate the parabolic rate in terms of oxide scale thickness, $k_{p,t}$ [cm^2s^{-1}], by plotting the oxide scale thickness in parabolic unit [cm^2] over time [s], as reported in Figure 3.43.

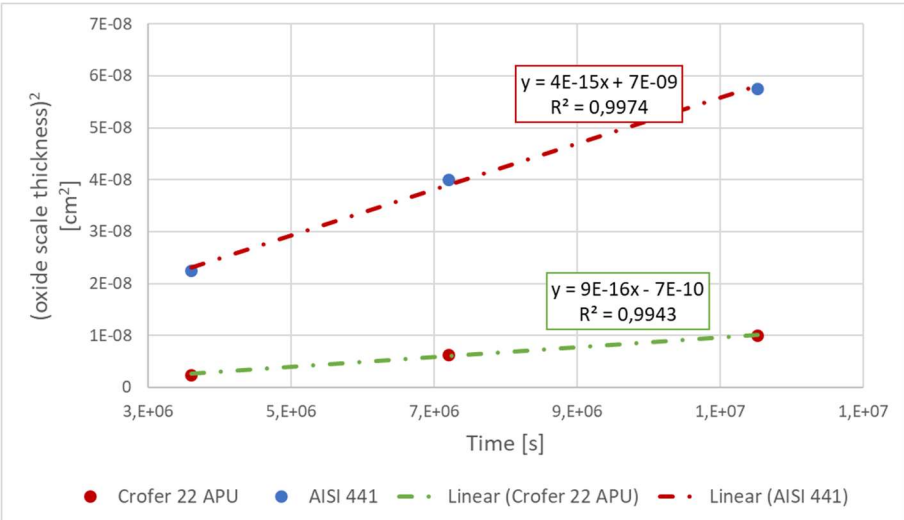

Figure 3.43: Oxide scale thickness in parabolic unit.

According to the parabolic law:

$$\xi^2 = 2k_{p,\xi} \cdot t + C$$

The calculated parabolic rates[4] for the oxide scale growth are $9x10^{-16}$ cm^2s^{-1} for Crofer 22 APU and $4x10^{-15}$ cm^2s^{-1} for AISI 441: thus, the two values differ for one order of magnitude (the reader should consider that the oxide scale thickness indicated for Crofer 22 APU samples does not include the RL).

With these oxidation rates, after 40000 h running, the AISI 441 interconnects should have an oxide scale of 7,63 µm, whereas the Crofer 22 APU ones 3,6 µm. These values are quite good, considering that the

[4] For simplicity, the slope of the straight lines was considered, not dividing it by the factor 2, as required by the parabolic law.

critical oxide scale thickness of Crofer 22 APU for spallation due to CTE mismatch was previously calculated at 11,4 µm [139].

Transforming the $k_{p,t}$ to the equivalent $k_{p,m}$ using [126]:

$$k_{p,m} = \left(\frac{V_{Cr_2O_3}}{16\,y}\right)^{-2} k_{p,t}$$

where, $V_{Cr_2O_3}$ is the molar volume of the oxide scale (29,2 cm^3mol^{-1}), it is found 2,4x10^{-15} $g^2cm^{-4}s^{-1}$ for Crofer 22 APU and 10,8x10^{-15} $g^2cm^{-4}s^{-1}$ for AISI 441.

These values can be compared to the $k_{p,m}$ obtained from gravimetric measurements (Table 3.18), checking that the formation of the real oxide scale would have caused considerably lower oxidation rates.

Table 3.18: Comparison between the oxidation rates from gravimentric measurement and the calculated ones.

$k_{p,m}$ [g^2 cm^{-4} s^{-1} 10^{-15}] from gravimetric measurement					**Calculated**
	MCO	5FeMCO	10FeMCO	10FeMCO_R1000	
Crofer 22 APU	14,5	6,6	6,6	3,3	2,4
AISI 441	24,6	33,7	30,6	23,0	10,8

The gap between the experimental and calculated $k_{p,m}$, is due to the oxygen uptake exploited by reactions of coating densification.

Similar result can be verified in the opposite direction. Under the assumption that the mass gain measurements were entirely due to the oxygen uptake to form the oxide scale, the corresponding Cr_2O_3 thickness can be calculated by [126]:

$$\tau_{Cr_2O_3} = \frac{MW_{Cr_2O_3}}{48 \cdot \rho_{Cr_2O_3}} \cdot \left(\frac{\Delta m}{A}\right)$$

where τ is the Cr_2O_3 thickens, ρ is it density (5,21 gcm^{-3}) and MW is the molar weight (152 $gmol^{-1}$) and 48 is a factor for converting the oxygen mass in the Cr_2O_3 (i.e. 16x3).

The values obtained by substituting the mass gain measured at 2000 h, are reported in Table 3.19. In the same table, the real oxide scale thickness measured by EDS of the 2000 h aged samples are presented as well.

Table 3.19: Theoretic oxide scale thicknesses at 2000 h based on mass gain, compared to the ones estimated by EDS.

Oxide scale thickness [µm]					
Steel/coating	MCO	5FeMCO	10FeMCO	10FeMCO_R1000	EDS 2000 h
Crofer 22 APU	1,76	1,21	1,21	0,85	0,8
AISI 441	2,30	2,67	2,55	2,1	2,0

This result shows that, if the weight gain was due entirely to the formation of chromia, its thickness should be generally greater than the measured ones.

It is also noted that the calculated values of the coatings reduced at 1000 °C instead of 900°C are closer to the measured ones, i.e. the higher temperature could improve the stability over time of the steel/coating couple.

Even if the growth of the oxide scale is confirmed to be parabolic, it is obvious that Crofer 22 APU and AISI 441 samples showed quite a different behaviour. Given that similar coatings were deposited, the difference in the oxidation mechanisms is likely to be related to the different compositions of the steels.

In an attempt to give an explanation to the results, two oxidation mechanisms are proposed below.

Crofer 22 APU

Figure 3.44 provides an overview of the first oxidation stage for Crofer 22 APU samples.

Oxygen can migrate through the open pores of the coating, thus reaching the steel surface.

The oxide scale is easily developed due to the inward diffusion of oxygen ions and of metallic cations from the steel, gradually forming Cr_2O_3 and $(MnCr)_3O_4$. This second phase is positioned under the chromium oxide because of the lower oxygen ratio required for the reaction; the round shape suggest that it forms where the oxygen ions find a favourite route for the diffusion, such as oxygen vacancies at the grain boundaries.

Not only the presence of Mn, but also the one of the RE (La) has a great influence in reducing the outward chromium diffusion: this is proved by the fact that a thin and irregular oxide scale is formed.

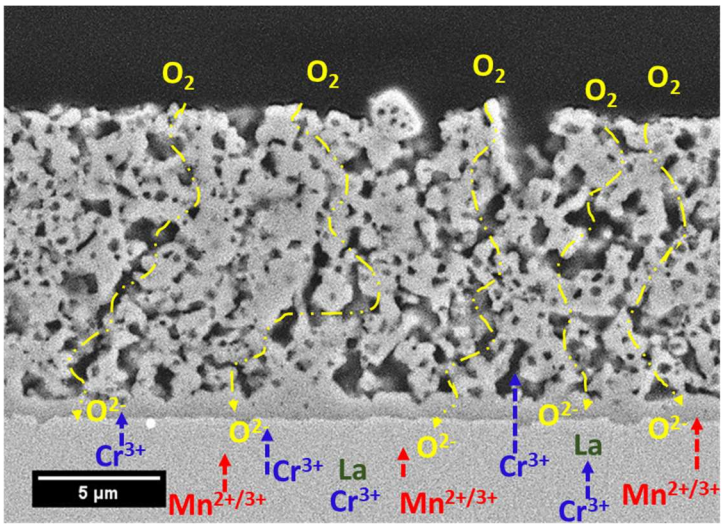

Figure 3.44: Schematization of the first stage of the oxidation for Crofer 22 APU samples (as sintered sample).

No iron was found in the undoped samples and the doped ones contained only the amount expected by the doping level: for this reason, the outward Fe diffusion is unlikely to be significant or negligible.

At this stage of oxidation, the formation of the RL is not detected, since its growth starts only after the rate of oxide scale is reduced.

This is also proved by the RL absence after 1000 h of oxidation and by the increasing of the ASR for the steel up to 3200 hrs.

The previous consideration introduces the second stage of the oxidation mechanism, proposed in Figure 3.45.

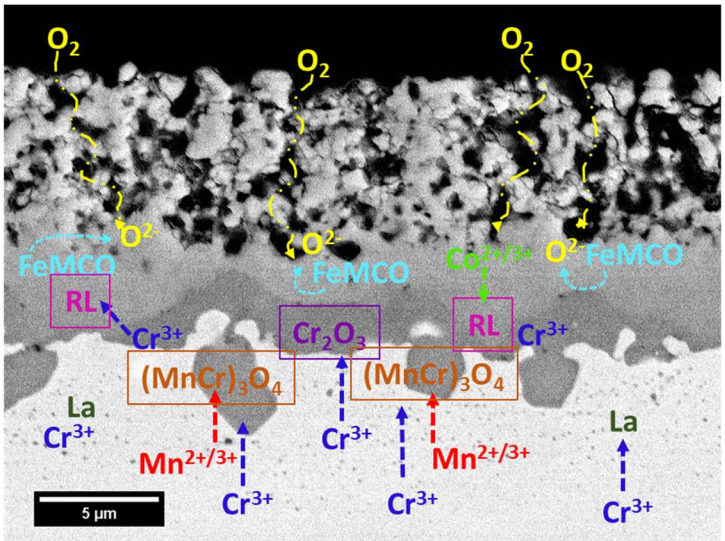

Figure 3.45: Schematization of the second stage of the oxidation for Crofer 22 APU samples (3200 h aged sample)

While the oxide scale becomes thicker, the ions diffusion path becomes longer: in agreement with the parabolic law, this results in a reduction of the oxide growth rate.

Moreover, the high Cr concentration in Crofer 22 APU makes the Cr_2O_3 layer to be much more protective and stable, meaning that few Cr cations can leave it.

In this scenario, the kinetics of the Co diffusion toward the chromium oxide scale gains importance.

As a consequence, the reaction layer is the result of the formation of a mixed spinel containing Mn-Co-Cr.

As already highlighted in [140], the RL is an evidence of the good Cr retention capability thanks to a good compatibility between the steel and the coating.

A densified coating layer (about 1 µm) was detected in contact with the RL only for the Fe-doped coatings on the Crofer substrate; this evidence suggests that the iron doping enhances the coating reactivity. The presence of this densified layer is supposed to reduce the oxygen partial pressure on the scale, with benefits for the mass gain and therefore for the oxidation rates.

Despite the presence of many different phases (steel/$(MnCr)_3O_4$/Cr_2O_3/RL/coating) no cracks due to CTE mismatch occurred, pointing out a functionally graded composition.

AISI 441

Figure 3.46 presents a schematization of the first stage of oxidation for AISI 441 samples.

As for the other steel, oxygen can migrate through the pores of the coating.

However, in the case of AISI 441, the greater amount of impurities causes the increase in the cations outward diffusion rate compared to that of oxygen ions inward diffusion.

This is confirmed by the progressive formation of a thick Cr_2O_3 toward the coating direction and not inside the steel.

The outward Cr diffusion is more relevant compared to Crofer 22 APU due to the absence of REs; for this reason, even the formation of $(MnCr)_3O_4$ under the steel surface seems to be impossible.

Silicon is only partially blocked by the Laves phase (Fe-Nb).

Titanium can either be oxidised by oxygen or diffuse toward the oxide scale and the coating.

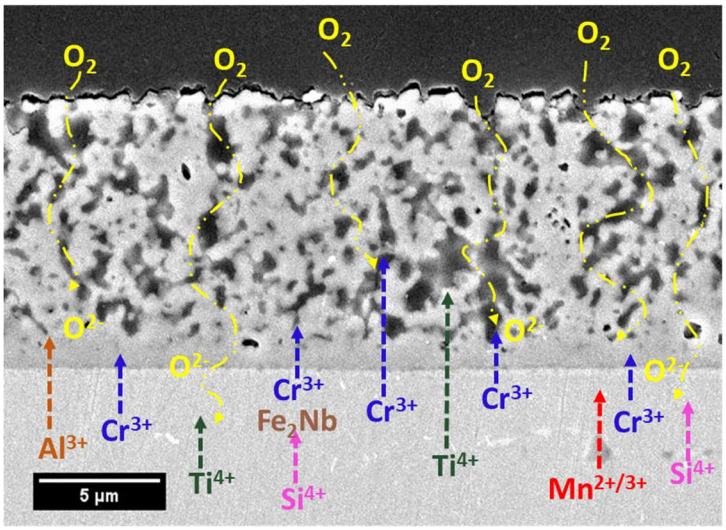

Figure 3.46: Schematization of the first stage of the oxidation for AISI 441 samples (as sintered sample).

The outward Cr diffusion is more relevant compared to Crofer 22 APU due to the absence of REs; for this reason, even the formation of $(MnCr)_3O_4$ under the steel surface seems to be impossible.

Silicon is only partially blocked by the Laves phase (Fe_2Nb).

Titanium can either be oxidised by oxygen or diffuse toward the oxide scale and the coating.

Therefore, Figure 3.47 shows an overview of the AISI 441 oxidation after 3200 h at 750°C.

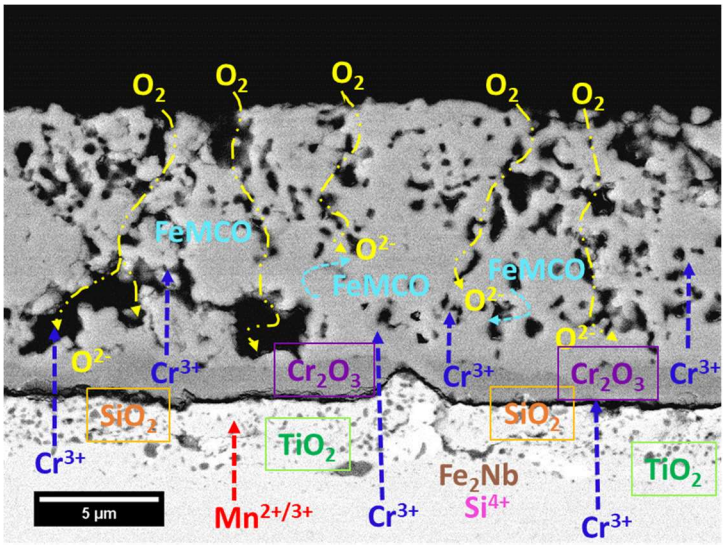

Figure 3.47: Schematization of the oxidation of AISI 441 samples at constant temperature (3200 h aged sample).

Fewer pores are present in the coating, which represent the preferential paths for the inward oxygen migration.

Titanium oxides formed in the sub-superficial area of steel, as a result of oxygen inward diffusion. Laves phases are present as well. Even if both Ti and Nb were added to the alloy to improve its performances, these second phases introduce many grain boundary defects, thus enhancing the cations diffusion.

Indeed, a steady and thick Cr_2O_3 layer forms in the outer part of the steel.

The Mn content is likely to be insufficient to achieve an acceptable Cr retention and the formation of the mixed spinel. It should also be reminded that the lower Cr content in the alloys, makes the passivating layer less protective and stable.

With this high Cr mobility, the RL is not formed, supporting that idea that its kinetic is slower compared to that of the Cr scale formation.

Silicon diffuses forming a continuous silica layer between the steel the oxide scale, suggesting a poor solubility in the Cr_2O_3.

The great densification of the whole thickness of the coating can be explained as following: the significant movement of cations creates much disorder in the system, which, together with the Fe-doping, increases the coating reactivity. In this regard, the smaller grain size in the doped coatings could have a negative influence for the further outward cations diffusion.

Cracks occur at the silica/chromia interface, proving both the insufficient effect of the Laves phase on Si retention and the significant CTE mismatch, particularly detrimental when samples are submitted to thermal cycling.

Some final considerations about the ASR results of the AISI 441 samples can now be suggested. Indeed, the formation of a steady and thick oxide scale, together with a continuous silica layer should theoretically worsen the electrical performances of the interconnect.

Nevertheless, since the conduction of the studied materials is strongly influenced by defects presence in the crystalline structure, it can be supposed that the outward diffusion of some small quantities of Ti, Si, Al, Fe and Mn can partially modify the electrical behaviour of the scales.

4. Conclusions

4.1. In-situ Fe-doping by electrophoretic co-deposition

The initial objective of the project was to identify the possibility of achieving the "in-situ" Fe doping of the MCO spinel by electrophoretic deposition.

The XRD analysis on the coatings after reduction confirmed that Fe was deposited and that after the first step of sintering Fe_2O_3 was completely reduced. In particular, the intermetallic compound $Co_{0,7}Fe_{0,3}$ was detected, which could have some effect of the dispersion of the metallic Co particles after the reduction and on the dimension of the cubic and tetragonal grains of the coating.

After the re-oxidation step, the XRD patters revealed that no residual Fe_2O_3 was present and that the spinel structure was formed.

All the obtained coatings were dense and continuous, meaning that they were effective in reducing the oxygen partial pressure on the scale.

The coatings reduced at higher temperature demonstrated higher densification (probably with more close porosity) and better stability over the long term, both considering the mass gain due to oxidation and the reactivity of the coating itself.

This new approach demonstrated the feasibility of achieving a mixed spinel structure by a low-cost, easy and fast production method.

4.2. Suitability of Fe-doped MCO coatings for Crofer 22 APU

The Crofer 22 APU samples coated with the Fe-doped spinels demonstrated a significant reduction in the oxidation rate compared to both the uncoated and the undoped MCO coated steel.

This effect was explained by the higher reactivity of the modified spinel, which formed a dense layer in contact with the Cr-rich reaction layer, considerably reducing the oxygen partial pressure on the oxide scale.

Furthermore, it is believed that the Cr contamination, due to thermal cycling and cracking of the AISI 441 samples in the oxidation test, affected the gravimetric measurements for Crofer 22 APU: without that drawback, the oxidation rates would have been even closer to the calculated ones.

The development of both the reaction layer and the densified coating can be ascribed as the reason for the increasing ASR from ca. 1500 h. By a linear extrapolation of the degradation rates, the coatings doped with 10% of iron demonstrated the highest ASR increase; however, it can be assumed that the growth of these zones also follows a parabolic trend and that the calculation represents the worst-case scenario.

Although more research is needed to determine the long-term effect of RL formation, it can be concluded that the Crofer 22 APU composition (high Cr content, Mn, La, low impurities level) ensures an improvement of the interconnect performances with the Fe-doped MCO coating; the best case can be identified in the 10FeMCO_R1000.

4.3. Suitability of Fe-doped MCO coatings for AISI 441

The explanation of the results on the samples of AISI 441 was found to be challenging.

Even if the mass gain of the coated sample was lower than that of the uncoated ones, the oxidation rates demonstrated to follow a para-linear behaviour. This was due to cracks occurring at the steel/coating interfaces because of thermal cycling and CTE mismatch, as well as the formation of Cr-rich spinels on the surfaces of the samples.

The microscopic investigation revealed the formation of a thick Cr_2O_3 layer growing on the outer part of the steel surface, which proved the low Cr retention of AISI 441. Moreover, a continuous silica layer formed beneath the oxide scale.

Despite these evidences, the ASR measurement at constant temperature surprisingly demonstrated to be stable at a low value, even after 3200 h. However, it is strongly believed that by applying one thermal cycling to the samples the ASR increase would have been dramatic because of cracks at the coating/steel interface.

On the basis of the research carried out so far, it cannot be concluded that the Fe-doped MCO coating improves the AISI 441 performances.

4.4. Future perspectives

The analysis of the potentials and limits of this work has provided some hints to which future research can be directed.

- Given that by co-depositing $Mn_{1,5}Co_{1,5}O_4$ and Fe_2O_3 the doped spinel structure was formed, the further research can be focused on exploring the feasibility of applying the same procedure for the co-deposition of manganese oxide, cobalt oxide and iron oxide. If this turns out to be possible, it would potentially lead to a reduction of coating production times and costs;
- It is considered useful to repeat the mass gain measurements, with samples divided by steel and coating type, to have a clearer evaluation of the source of the Cr contamination;
- Considering the good results obtained by the Crofer 22 APU samples, a new experiment could be carried out to study the oxidation mechanism on the dual (reducing and oxidizing) atmosphere;
- Some measures of Cr evaporation from AISI 441 with the doped coatings seem to be necessary in order to evaluate the effect of Fe presence in enhancing ions diffusion.

At the moment, the research is focused on:

- Examining the doped spinel structure by transmission electron microscopy and selected area electron diffraction;
- Evaluating the electrical conductivity on Fe-doped MnCo spinels in form of pellets:
- Measuring the ASR in air by applying thermal cycling;
- Measuring the ASR at different oxygen partial pressures.

Abbreviations

10FeMCO: Manganese cobalt spinel ($Mn_{1,5}Co_{1,5}O_4$) doped with 10 wt.% of Fe

10FeMCO_R1000: Manganese cobalt spinel ($Mn_{1,5}Co_{1,5}O_4$) doped with 10 wt.% of Fe and reduced at 1000 °C

441: Ferritic stainless steel AISI 441 by Sandvik

5FeMCO: Manganese cobalt spinel ($Mn_{1,5}Co_{1,5}O_4$) doped with 5 wt.% of Fe

ASR: Area Specific Resistance [$m\Omega\ cm^2$]

ASR_LSM: Area Specific Resistance measured using LSM plates as contacts

ASR_Pt: Area Specific Resistance measured using platinum contacts

C22A: Ferritic stainless steel CROFER 22 APU by Thyssenkrupp

CTE: Coefficient of thermal expansion [$10^{-6}K^{-1}$]

E_A: Activation energy [$kJmol^{-1}$]

EDL: Electrical Double Layer

EDS/EDX: Energy-dispersive X-ray spectroscopy

EP-co-D: Electrophoretic co-deposition

EPD: Electrophoretic deposition

FC: Fuel Cell

FE-SEM: Field emission scanning electron microscope

FSS: Ferritic stainless steel

$k_{p,m}$: Parabolic rate constant in term of mass gain [$g^2cm^{-4}s^{-1}$]

$k_{p,t}$: Parabolic rate constant in term of oxide scale thickness [cm^2s^{-1}]

LSM: lanthanum strontium manganite perovskite ($La_{1-x}Sr_xMnO_3$)

MCO: Manganese cobalt spinel ($Mn_{1,5}Co_{1,5}O_4$)

OR: Oxidation resistance

RE: Reactive element (rare earth)

RL: Reaction layer

SEM: Scanning electron microscope

SOFC: Solid Oxide Fuel Cell

XRD: X-ray diffraction

σ: Electrical conductivity [Scm^{-1}]

Bibliography

[1] N. Mahato, A. Banerjee, A. Gupta, S. Omar, and K. Balani, "Progress in material selection for solid oxide fuel cell technology: A review," *Prog. Mater. Sci.*, vol. 72, pp. 141–337, 2015.

[2] EIA, "Today in Energy," 2017. [Online]. Available: https://www.eia.gov/todayinenergy/detail.php?id=32912. [Accessed: 10-Aug-2018].

[3] The British Petroleum Company, "BP Energy outlook 2018," 2018. [Online]. Available: https://www.bp.com/content/dam/bp/en/corporate/pdf/energy-economics/energy-outlook/bp-energy-outlook-2018.pdf. [Accessed: 16-Aug-2016].

[4] European Commission, "2050 Energy Strategy." [Online]. Available: https://ec.europa.eu/energy/en/topics/energy-strategy-and-energy-union/2050-energy-strategy. [Accessed: 10-Aug-2018].

[5] EIA, "Global Energy & CO2 Status Report, 2017," 2018. [Online]. Available: https://www.iea.org/publications/freepublications/publication/GECO2017.pdf. [Accessed: 13-Aug-2018].

[6] Cambridge Econometrics, "A Study on Oil Dependency in the EU," 2016. [Online]. Available: https://www.camecon.com/wp-content/uploads/2016/11/Study-on-EU-oil-dependency-v1.4_Final.pdf.

[7] J. Mermelstein and O. Posdziech, "Development and Demonstration of a Novel Reversible SOFC System for Utility and Micro Grid Energy Storage," *Fuel Cells*, vol. 17, no. 4, pp. 562–570, 2017.

[8] O. Z. Sharaf and M. F. Orhan, "An overview of fuel cell technology: Fundamentals and applications," *Renew. Sustain. Energy Rev.*, vol. 32, pp. 810–853, 2014.

[9] S. M. Haile, "Fuel cell materials and components," *Acta Mater.*, vol. 51, no. 19, pp. 5981–6000, 2003.

[10] F. S. da Silva and T. M. de Souza, "Novel materials for solid oxide fuel cell technologies: A literature review," *Int. J. Hydrogen Energy*, vol. 42, no. 41, pp. 26020–26036, 2017.

[11] M. P. Carpanese, M. Panizza, M. Viviani, E. Mercadelli, A. Sanson, and A. Barbucci, "Study of reversible SOFC/SOEC based on a mixed anionic-protonic conductor," *J. Appl. Electrochem.*, vol. 45, no. 7, pp. 657–665, 2015.

[12] P. D. Jablonski, C. J. Cowen, and J. S. Sears, "Exploration of alloy 441 chemistry for solid oxide fuel cell interconnect application," *J. Power Sources*, vol. 195, no. 3, pp. 813–820, 2010.

[13] Research Centre Jülich, "World Record: Jülich Fuel Cell Passes 40,000 Hour Mark," 2012. [Online]. Available: https://fuelcellsworks.com/archives/2012/03/30/world-record-julich-fuel-cell-passes-40000-hour-mark/.

[14] M. K. Mahapatra and K. Lu, "Seal glass for solid oxide fuel cells," *J. Power Sources*, vol. 195, no. 21, pp. 7129–7139, 2010.

[15] W. Z. Zhu and S. C. Deevi, "Development of interconnect materials for solid oxide fuel cells," *Mater. Sci. Eng. A*, vol. 348, no. 1, pp. 227–243, 2003.

[16] F. Smeacetto, A. Chrysanthou, M. Salvo, Z. Zhang, and M. Ferraris, "Performance and testing of glass-ceramic sealant used to join anode-supported-electrolyte to Crofer22APU in planar solid oxide fuel cells," *J. Power Sources*, vol. 190, no. 2, pp. 402–407, 2009.

[17] B. Talic, *PhD Thesis. Metallic Interconnects for Solid Oxide Fuel Cells: High Temperature Corrosion and Protective Spinel Coatings*, vol. 7. 2016.

[18] S. M. Majhi *et al.*, "Anode supported solid oxide fuel cells (SOFC) by electrophoretic deposition," *Int. J. Hydrogen Energy*, vol. 36, no. 22, pp. 14930–14935, 2011.

[19] F. Smeacetto *et al.*, "Electrophoretic deposition of Mn1.5Co1.5O4on metallic interconnect and interaction with glass-ceramic sealant for solid oxide fuel cells application," *J. Power Sources*, vol. 280, pp. 379–386, 2015.

[20] J. Wu and X. Liu, "Recent Development of SOFC Metallic Interconnect • Invited Review," *J. Mater. Sci. Technol.*, vol. 26, no. 4, pp. 293–305, 2010.

[21] A. Weber and E. Ivers-Tiffée, "Materials and concepts for solid oxide fuel cells (SOFCs) in stationary and mobile applications," *J. Power Sources*, vol. 127, no. 1–2, pp. 273–283, 2004.

[22] N. Shaigan, W. Qu, D. G. Ivey, and W. Chen, "A review of recent progress in coatings, surface modifications and alloy developments for solid oxide fuel cell ferritic stainless steel interconnects," *J. Power Sources*, vol. 195, no. 6, pp. 1529–1542, 2010.

[23] W. J. Quadakkers, J. Piron-Abellan, V. Shemet, and L. Singheiser, "Metallic interconnectors for solid oxide fuel cells – a review," *Mater. High Temp.*, vol. 20, no. 2, pp. 115–127, Jan. 2003.

[24] J. C. W. Mah, A. Muchtar, M. R. Somalu, and M. J. Ghazali, "Metallic interconnects for solid oxide fuel cell: A review on protective coating and deposition techniques," *Int. J. Hydrogen Energy*, vol. 42, no. 14, pp. 9219–9229, 2017.

[25] N. Q. Minh, "Ceramic Fuel Cells," *J. Am. Ceram. Soc.*, vol. 76, no. 3, pp. 563–588, Mar. 1993.

[26] P. KOFSTAD and R. BREDESEN, "High temperature corrosion in SOFC environments," *Solid State Ionics*, vol. 52, no. 1–3, pp. 69–75, May 1992.

[27] M. Stanislowski *et al.*, "Reduction of chromium vaporization from SOFC interconnectors by highly effective coatings," *J. Power Sources*, vol. 164, no. 2, pp. 578–589, 2007.

[28] J. Puranen *et al.*, "The structure and properties of plasma sprayed iron oxide doped manganese cobalt oxide spinel coatings for SOFC metallic interconnectors," *J. Therm. Spray Technol.*, vol. 20, no. 1–2, pp. 154–159, 2011.

[29] Y.-Y. Chang, C.-P. Chang, D.-Y. Wang, S.-M. Yang, and W. Wu, "High temperature oxidation resistance of CrAlSiN coatings synthesized by a cathodic arc deposition process," *J. Alloys Compd.*, vol. 461, no. 1–2, pp. 336–341, Aug. 2008.

[30] P. Piccardo *et al.*, "ASR evaluation of different kinds of coatings on a ferritic stainless steel as SOFC interconnects," *Surf. Coatings Technol.*, vol. 202, no. 4–7, pp. 1221–1225, Dec. 2007.

[31] N. Orlovskaya, A. Coratolo, C. Johnson, and R. Gemmen, "Structural Characterization of Lanthanum Chromite Perovskite Coating Deposited by Magnetron Sputtering on an Iron-Based Chromium-Containing Alloy as a Promising Interconnect Material for SOFCs," *J. Am. Ceram. Soc.*, vol. 87, no. 10, pp. 1981–1987, Jan. 2005.

[32] Y. Larring and T. Norby, "Spinel and Perovskite Functional Layers Between Plansee Metallic Interconnect (Cr-5 wt % Fe-1 wt % Y[sub 2]O[sub 3]) and Ceramic (La[sub 0.85]Sr[sub 0.15])[sub 0.91]MnO[sub 3] Cathode Materials for Solid Oxide Fuel Cells," *J. Electrochem. Soc.*, vol. 147, no. 9, p. 3251, 2000.

[33] A. Masi *et al.*, "Cu-Mn-Co oxides as protective materials in SOFC technology: The effect of chemical composition on mechanochemical synthesis, sintering behaviour, thermal expansion and electrical conductivity," *J. Eur. Ceram. Soc.*, vol. 37, no. 2, pp. 661–669, 2017.

[34] S. Chevalier, C. Valot, G. Bonnet, J. . Colson, and J. . Larpin, "The reactive element effect on

thermally grown chromia scale residual stress," *Mater. Sci. Eng. A*, vol. 343, no. 1–2, pp. 257–264, Feb. 2003.

[35] B. Talic, H. Falk-Windisch, V. Venkatachalam, P. V. Hendriksen, K. Wiik, and H. L. Lein, "Effect of coating density on oxidation resistance and Cr vaporization from solid oxide fuel cell interconnects," *J. Power Sources*, vol. 354, pp. 57–67, 2017.

[36] T. Brylewski *et al.*, "Microstructure and electrical properties of Mn1+xCo2−xO4 (0≤x≤1.5) spinels synthesized using EDTA-gel processes," *Ceram. Int.*, vol. 40, no. 9, pp. 13873–13882, Nov. 2014.

[37] Y. Liu, J. W. Fergus, and C. Dela Cruz, "Electrical properties, cation distributions, and thermal expansion of manganese cobalt chromite spinel oxides," *J. Am. Ceram. Soc.*, vol. 96, no. 6, pp. 1841–1846, 2013.

[38] Z. YANG, G. XIA, X. LI, and J. STEVENSON, "(Mn,Co)3O4 spinel coatings on ferritic stainless steels for SOFC interconnect applications," *Int. J. Hydrogen Energy*, vol. 32, no. 16, pp. 3648–3654, Nov. 2007.

[39] L. Chen, E. Y. Sun, J. Yamanis, and N. Magdefrau, "Oxidation Kinetics of Mn[sub 1.5]Co[sub 1.5]O[sub 4]-Coated Haynes 230 and Crofer 22 APU for Solid Oxide Fuel Cell Interconnects," *J. Electrochem. Soc.*, vol. 157, no. 6, p. B931, 2010.

[40] S. Molin *et al.*, "Microstructural and electrical characterization of Mn-Co spinel protective coatings for solid oxide cell interconnects," *J. Eur. Ceram. Soc.*, vol. 37, no. 15, pp. 4781–4791, 2017.

[41] Å. H. Persson, L. Mikkelsen, P. V. Hendriksen, and M. A. J. Somers, "Interaction mechanisms between slurry coatings and solid oxide fuel cell interconnect alloys during high temperature oxidation," *J. Alloys Compd.*, vol. 521, pp. 16–29, Apr. 2012.

[42] V. I. Gorokhovsky *et al.*, "Deposition and Evaluation of Protective PVD Coatings on Ferritic Stainless Steel SOFC Interconnects," *J. Electrochem. Soc.*, vol. 153, no. 10, p. A1886, 2006.

[43] C. C. Mardare, M. Spiegel, A. Savan, and A. Ludwig, "Thermally Oxidized Mn–Co Thin Films as Protective Coatings for SOFC Interconnects," *J. Electrochem. Soc.*, vol. 156, no. 12, p. B1431, 2009.

[44] J. Puranen *et al.*, "Post-mortem evaluation of oxidized atmospheric plasma sprayed Mn-Co-Fe oxide spinel coatings on SOFC interconnectors," *Int. J. Hydrogen Energy*, vol. 39, no. 30, pp. 17284–17294, 2014.

[45] H. H. Zhang and C. L. Zeng, "Preparation and performances of Co–Mn spinel coating on a ferritic stainless steel interconnect material for solid oxide fuel cell application," *J. Power Sources*, vol. 252, pp. 122–129, Apr. 2014.

[46] S. J. Han, Z. Pala, and S. Sampath, "Plasma sprayed manganese–cobalt spinel coatings: Process sensitivity on phase, electrical and protective performance," *J. Power Sources*, vol. 304, pp. 234–243, Feb. 2016.

[47] S. R. Akanda, M. E. Walter, N. J. Kidner, and M. M. Seabaugh, "Mechanical characterization of oxide coating–interconnect interfaces for solid oxide fuel cells," *J. Power Sources*, vol. 210, pp. 254–262, Jul. 2012.

[48] S.-I. Lee *et al.*, "Highly Dense Mn-Co Spinel Coating for Protection of Metallic Interconnect of Solid Oxide Fuel Cells," *J. Electrochem. Soc.*, vol. 161, no. 14, pp. F1389–F1394, Oct. 2014.

[49] A. Kruk, M. Stygar, and T. Brylewski, "Mn–Co spinel protective–conductive coating on AL453 ferritic stainless steel for IT-SOFC interconnect applications," *J. Solid State Electrochem.*, vol. 17, no. 4, pp. 993–1003, Apr. 2013.

[50] M. Bobruk, S. Molin, M. Chen, T. Brylewski, and P. V. Hendriksen, “Sintering of MnCo2O4coatings prepared by electrophoretic deposition,” *Mater. Lett.*, vol. 213, pp. 394–398, 2018.

[51] V. Venkatachalam, S. Molin, W. R. Kiebach, M. Chen, and P. V Hendriksen, “Influence of Mn-Co Spinel Coating on Oxidation Behavior of Ferritic Ss Alloys for Sofc Interconnect Applications,” *Mater. Sci. Technol. 2014*, pp. 1213–1220, 2014.

[52] H. Zhang, Z. Zhan, and X. Liu, “Electrophoretic deposition of (Mn,Co)3O4spinel coating for solid oxide fuel cell interconnects,” *J. Power Sources*, vol. 196, no. 19, pp. 8041–8047, 2011.

[53] F. Cheng, J. Cui, L. Wang, S. Li, and J. Sun, “Performance of Co Ni O spinel oxide coating on AISI 430 stainless steel as interconnect for intermediate temperature solid oxide fuel cell,” *Int. J. Hydrogen Energy*, vol. 42, no. 17, pp. 12477–12484, Apr. 2017.

[54] G. Jalilvand and M. A. Faghihi-Sani, “Fe doped Ni-Co spinel protective coating on ferritic stainless steel for SOFC interconnect application,” *Int. J. Hydrogen Energy*, vol. 38, no. 27, pp. 12007–12014, 2013.

[55] R. Irankhah, B. Raissi, A. Maghsoudipour, A. Irankhah, and S. Ghashghai, “NiFe2O4 Spinel Protection Coating for High-Temperature Solid Oxide Fuel Cell Interconnect Application,” *J. Mater. Eng. Perform.*, vol. 25, no. 4, pp. 1515–1525, Apr. 2016.

[56] S. Joshi and A. Petric, “Nickel substituted CuMn 2 O 4 spinel coatings for solid oxide fuel cell interconnects,” *Int. J. Hydrogen Energy*, vol. 42, no. 8, pp. 5584–5589, Feb. 2017.

[57] J. Froitzheim, S. Canovic, M. Nikumaa, R. Sachitanand, L. G. Johansson, and J. E. Svensson, “Long term study of Cr evaporation and high temperature corrosion behaviour of Co coated ferritic steel for solid oxide fuel cell interconnects,” *J. Power Sources*, vol. 220, pp. 217–227, Dec. 2012.

[58] K. Wang, Y. Liu, and J. W. Fergus, “Interactions between SOFC interconnect coating materials and chromia,” *J. Am. Ceram. Soc.*, vol. 94, no. 12, pp. 4490–4495, 2011.

[59] C.-O. P. B.-K. Park, J.-W. Lee, S.-B. Lee, T.-H. Lim, S.-J. Park, “Cu-and Ni-doped Mn 1.5 Co 1.5 O 4 spinel coatings on metallic interconnects for solid oxide fuel cells.,” *Int. J. Hydrogen Energy*, vol. 38, pp. 12043–12050, 2013.

[60] J. W. Stevenson, Z. G. Yang, G. G. Xia, Z. Nie, and J. D. Templeton, “Long-term oxidation behavior of spinel-coated ferritic stainless steel for solid oxide fuel cell interconnect applications,” *J. Power Sources*, vol. 231, pp. 256–263, 2013.

[61] J. Xiao, W. Zhang, C. Xiong, B. Chi, J. Pu, and L. Jian, “Oxidation behavior of Cu-doped MnCo 2 O 4 spinel coating on ferritic stainless steels for solid oxide fuel cell interconnects,” *Int. J. Hydrogen Energy*, vol. 41, no. 22, pp. 9611–9618, Jun. 2016.

[62] Z. Sun, S. Gopalan, U. B. Pal, and S. N. Basu, “Cu 1.3 Mn 1.7 O 4 spinel coatings deposited by electrophoretic deposition on Crofer 22 APU substrates for solid oxide fuel cell applications,” *Surf. Coatings Technol.*, vol. 323, pp. 49–57, Aug. 2017.

[63] G. Chen *et al.*, “Mn 1.4 Co 1.4 Cu 0.2 O 4 spinel protective coating on ferritic stainless steels for solid oxide fuel cell interconnect applications,” *J. Power Sources*, vol. 278, pp. 230–234, Mar. 2015.

[64] Y. Xu, Z. Wen, S. Wang, and T. Wen, “Cu doped Mn–Co spinel protective coating on ferritic stainless steels for SOFC interconnect applications,” *Solid State Ionics*, vol. 192, no. 1, pp. 561–564, Jun. 2011.

[65] B. Talic, S. Molin, K. Wiik, P. V. Hendriksen, and H. L. Lein, “Comparison of iron and copper doped manganese cobalt spinel oxides as protective coatings for solid oxide fuel cell interconnects,” *J. Power Sources*, vol. 372, no. September, pp. 145–156, 2017.

[66] A. Masi *et al.*, “The effect of chemical composition on high temperature behaviour of Fe and Cu doped Mn-Co spinels,” *Ceram. Int.*, vol. 43, no. November 2016, pp. 2829–2835, 2016.

[67] S. Molin, A. G. Sabato, H. Javed, G. Cempura, A. R. Boccaccini, and F. Smeacetto, “Co-deposition of CuO and Mn 1.5 Co 1.5 O 4 powders on Crofer22APU by electrophoretic method: Structural, compositional modifications and corrosion properties,” *Mater. Lett.*, vol. 218, pp. 329–333, May 2018.

[68] A. Purwanto, A. Fajar, H. Mugirahardjo, J. W. Fergus, and K. Wang, “Cation distribution in spinel (Mn,Co,Cr)3O4 at room temperature,” *J. Appl. Crystallogr.*, vol. 43, no. 3, pp. 394–400, 2010.

[69] Aditya vardhan Vutturi, “adichemistry,” 2011. [Online]. Available: https://www.adichemistry.com/inorganic/cochem/spinels/spinel-structures.html. [Accessed: 13-Aug-2018].

[70] “crystallography365,” 2014. [Online]. Available: https://crystallography365.wordpress.com/tag/spinel/. [Accessed: 13-Aug-2018].

[71] H. Bordeneuve, C. Tenailleau, S. Guillemet-Fritsch, R. Smith, E. Suard, and A. Rousset, “Structural variations and cation distributions in Mn3-xCoxO4(0 ≤ x ≤ 3) dense ceramics using neutron diffraction data,” *Solid State Sci.*, vol. 12, no. 3, pp. 379–386, 2010.

[72] R. Valenzuela, *Magnetic ceramics*. Cambridge, 1994.

[73] A. K. Giri, E. M. Kirkpatrick, P. Moongkhamklang, S. A. Majetich, and V. G. Harris, “Photomagnetism and structure in cobalt ferrite nanoparticles,” *Appl. Phys. Lett.*, vol. 80, no. 13, pp. 2341–2343, Apr. 2002.

[74] K. K. Bamzai, G. Kour, B. Kaur, and S. D. Kulkarni, “Preparation, and Structural and Magnetic Properties of Ca Substituted Magnesium Ferrite with Composition MgCa x Fe 2− x O 4 (x = 0.00, 0.01, 0.03, 0.05, 0.07),” *J. Mater.*, vol. 2014, pp. 1–8, 2014.

[75] S. Lower, “Cubic Lattices and Close Packing,” 2018. [Online]. Available: https://chem.libretexts.org/Textbook_Maps/General_Chemistry/Book%3A_Chem1_(Lower)/07%3A_Solids_and_Liquids/7.08%3A_Cubic_Lattices_and_Close_Packing. [Accessed: 13-Aug-2018].

[76] E. AUKRUST and A. MUAN, “Phase Relations in the System Cobalt Oxide-Manganese Oxide in Air,” *J. Am. Ceram. Soc.*, vol. 46, no. 10, pp. 511–511, Oct. 1963.

[77] D. G. Wickham and J. B. Goodenough, “Suggestion Concerning Magnetic Interactions in Spinels,” *Phys. Rev.*, vol. 115, no. 5, pp. 1156–1158, Sep. 1959.

[78] B. Boucher, R. Buhl, R. Di Bella, and M. Perrin, “Etude par des mesures de diffraction de neutrons et de magnétisme des propriétés cristallines et magnétiques de composés cubiques spinelles Co3-xMnxO4(0,6 ≤ x ≤ 1,2),” *J. Phys.*, vol. 31, no. 1, pp. 113–119, 1970.

[79] E. Lee, J.-H. Jang, and Y.-U. Kwon, “Composition effects of spinel MnxCo3−xO4 nanoparticles on their electrocatalytic properties in oxygen reduction reaction in alkaline media,” *Journal of Power Sources*, vol. 273. pp. 735–741, 2015.

[80] D. W. Jeong, W. J. Jang, J. O. Shim, and H. S. Roh, “High temperature water–gas shift without pre-reduction over spinel ferrite catalysts synthesized by glycine assisted sol–gel combustion method,” *Int. J. Hydrogen Energy*, vol. 41, no. 6, pp. 3870–3876, 2016.

[81] C. N. R. Rao and G. V. Subba Rao, “Electrical conduction in metal oxides,” *Phys. Status Solidi*, vol. 1, no. 4, pp. 597–652, Apr. 1970.

[82] Z. Lu, J. Zhu, E. Andrew Payzant, and M. P. Paranthaman, “Electrical Conductivity of the Manganese Chromite Spinel Solid Solution,” *J. Am. Ceram. Soc.*, vol. 88, no. 4, pp. 1050–1053,

Apr. 2005.

[83] A. Petric and H. Ling, “Electrical conductivity and thermal expansion of spinels at elevated temperatures,” *J. Am. Ceram. Soc.*, vol. 90, no. 5, pp. 1515–1520, 2007.

[84] Y. Liu, J. W. Fergus, K. Wang, and C. Dela Cruz, “Crystal Structure, Chemical Stabilities and Electrical Conductivity of Fe-Doped Manganese Cobalt Spinel Oxides for SOFC Interconnect Coatings,” *J. Electrochem. Soc.*, vol. 160, no. 11, pp. F1316–F1321, Oct. 2013.

[85] N. Sakai *et al.*, “Structure and transport property of manganese-chromium-iron oxide as a main compound in oxide scales of alloy interconnects for SOFCs,” *Solid State Ionics*, vol. 176, no. 7–8, pp. 681–686, 2005.

[86] W. Nicodemi, *Acciai e leghe non ferrose*, 2nd ed. 2008.

[87] M. Mcguire, “Austenitic Stainless Steels,” *Stainl. Steels Des. Eng.*, pp. 69–78, 2008.

[88] J. Akram, R. Puli, P. R. Kalvala, and M. Misra, “A novel weld transition joint by friction surfacing,” *Manuf. Lett.*, vol. 2, no. 4, pp. 104–107, Oct. 2014.

[89] Z. Yang, K. S. Weil, D. M. Paxton, and J. W. Stevenson, “Selection and Evaluation of Heat-Resistant Alloys for SOFC Interconnect Applications,” *J. Electrochem. Soc.*, vol. 150, no. 9, p. A1188, 2003.

[90] M. Stanislowski, E. Wessel, K. Hilpert, T. Markus, and L. Singheiser, “Chromium Vaporization from High-Temperature Alloys,” *J. Electrochem. Soc.*, vol. 154, no. 4, p. A295, 2007.

[91] H. Falk-Windisch, J. E. Svensson, and J. Froitzheim, “The effect of temperature on chromium vaporization and oxide scale growth on interconnect steels for Solid Oxide Fuel Cells,” *J. Power Sources*, vol. 287, pp. 25–35, 2015.

[92] W. Wongpromrat, H. Thaikan, W. Chandra-Ambhorn, and S. Chandra-Ambhorn, “Chromium vaporisation from AISI 441 stainless steel oxidised in humidified oxygen,” *Oxid. Met.*, vol. 79, no. 5–6, pp. 529–540, 2013.

[93] H. Bartzsch, D. Glöß, B. Böcher, P. Frach, and K. Goedicke, “Properties of SiO2 and Al2O3 films for electrical insulation applications deposited by reactive pulse magnetron sputtering,” *Surf. Coatings Technol.*, vol. 174–175, pp. 774–778, Sep. 2003.

[94] H. Tada *et al.*, “Thermal expansion coefficient of polycrystalline silicon and silicon dioxide thin films at high temperatures,” *J. Appl. Phys.*, vol. 87, no. 9, pp. 4189–4193, May 2000.

[95] B. El-Kareh, *Fundamentals of Semiconductor Processing Technology*. Boston, MA: Springer US, 1995.

[96] J. Froitzheim *et al.*, “Development of high strength ferritic steel for interconnect application in SOFCs,” *J. Power Sources*, vol. 178, no. 1, pp. 163–173, 2008.

[97] T. Horita *et al.*, “Evaluation of Laves-phase forming Fe-Cr alloy for SOFC interconnects in reducing atmosphere,” *J. Power Sources*, vol. 176, no. 1, pp. 54–61, 2008.

[98] R. Sachitanand, M. Sattari, J. E. Svensson, and J. Froitzheim, “Evaluation of the oxidation and Cr evaporation properties of selected FeCr alloys used as SOFC interconnects,” *Int. J. Hydrogen Energy*, vol. 38, no. 35, pp. 15328–15334, 2013.

[99] J. G. Grolig, “Coated Ferritic Stainless Steels as Interconnects in Solid Oxide Fuel Cells,” 2013.

[100] D. P. Whittle and J. Stringer, “Improvements in High Temperature Oxidation Resistance by Additions of Reactive Elements or Oxide Dispersions,” *Philos. Trans. R. Soc. A Math. Phys. Eng. Sci.*, vol. 295, no. 1413, pp. 309–329, Feb. 1980.

[101] J. G. Grolig, J. Froitzheim, and J. E. Svensson, “Coated stainless steel 441 as interconnect

material for solid oxide fuel cells: Oxidation performance and chromium evaporation," *J. Power Sources*, vol. 248, pp. 1007–1013, 2014.

[102] Z. Yang *et al.*, "Investigation of iron-chromium-niobium-titanium ferritic stainless steel for solid oxide fuel cell interconnect applications," *J. Power Sources*, vol. 183, no. 2, pp. 660–667, 2008.

[103] H. Ebrahimifar and M. Zandrahimi, "Oxidation and electrical behavior of AISI 430 coated with cobalt spinels for SOFC interconnect applications," *Surf. Coatings Technol.*, vol. 206, no. 1, pp. 75–81, Oct. 2011.

[104] A. M. Huntz *et al.*, "Oxidation of AISI 304 and AISI 439 stainless steels," *Mater. Sci. Eng. A*, vol. 447, no. 1–2, pp. 266–276, Feb. 2007.

[105] S. Frangini, A. Masci, S. J. McPhail, T. Soccio, and F. Zaza, "Degradation behavior of a commercial 13Cr ferritic stainless steel (SS405) exposed to an ambient air atmosphere for IT-SOFC interconnect applications," *Mater. Chem. Phys.*, vol. 144, no. 3, pp. 491–497, Apr. 2014.

[106] VDM-Metals, "VDM ® Crofer 22 APU," no. Werkstoffdatenblatt Ausgabe Januar, p. 10, 2010.

[107] H. Falk-Windisch, J. Claquesin, J.-E. Svensson, and J. Froitzheim, "The Effect of Metallic Co-Coating Thickness on Ferritic Stainless Steels Intended for Use as Interconnect Material in Intermediate Temperature Solid Oxide Fuel Cells," *Oxid. Met.*, vol. 89, no. 1, pp. 233–250, 2017.

[108] B. Talic, S. Molin, P. V. Hendriksen, and H. L. Lein, "Effect of pre-oxidation on the oxidation resistance of Crofer 22 APU," *Corros. Sci.*, vol. 138, no. April, pp. 189–199, 2018.

[109] P. D. Jablonski and D. E. Alman, "Oxidation resistance of novel ferritic stainless steels alloyed with titanium for SOFC interconnect applications," *J. Power Sources*, vol. 180, no. 1, pp. 433–439, 2008.

[110] W. Z. Zhu and S. C. Deevi, "Opportunity of metallic interconnects for solid oxide fuel cells: A status on contact resistance," *Mater. Res. Bull.*, vol. 38, no. 6, pp. 957–972, 2003.

[111] N. J. Magdefrau, L. Chen, E. Y. Sun, J. Yamanis, and M. Aindow, "Formation of spinel reaction layers in manganese cobaltite-coated Crofer22 APU for solid oxide fuel cell interconnects," *J. Power Sources*, vol. 227, pp. 318–326, 2013.

[112] C. J. Wiley, I. All, and X. Liu, "Other Technologies Energy Technology 2012 : Fuel Cells Session Chairs : Other Technologies Energy Technology 2012 : Fuel Cells Session Chairs :," 2018.

[113] H. C. Hamaker, "Formation of a deposit by electrophoresis," *Trans. Faraday Soc.*, vol. 35, p. 279, 1940.

[114] I. N. Levine, "Physical Chemistry, Second Edition," *J. Chem. Educ.*, vol. 64, no. 3, p. A91, Mar. 1987.

[115] L. Besra and M. Liu, "A review on fundamentals and applications of electrophoretic deposition (EPD)," *Prog. Mater. Sci.*, vol. 52, no. 1, pp. 1–61, 2007.

[116] H.-J. Butt, K. Graf, and M. Kappl, *Physics and Chemistry of Interfaces*. Weinheim, FRG: Wiley-VCH Verlag GmbH & Co. KGaA, 2003.

[117] I. Corni, M. P. Ryan, and A. R. Boccaccini, "Electrophoretic deposition: From traditional ceramics to nanotechnology," *J. Eur. Ceram. Soc.*, vol. 28, no. 7, pp. 1353–1367, 2008.

[118] M. Ammam, "Electrophoretic deposition under modulated electric fields: A review," *RSC Advances*, vol. 2, no. 20. pp. 7633–7646, 2012.

[119] O. O. Van der Biest and L. J. Vandeperre, "ELECTROPHORETIC DEPOSITION OF MATERIALS," *Annu. Rev. Mater. Sci.*, vol. 29, no. 1, pp. 327–352, Aug. 1999.

[120] P. Sarkar and P. S. Nicholson, "Electrophoretic Deposition (EPD): Mechanisms, Kinetics, and

Application to Ceramics," *J. Am. Ceram. Soc.*, vol. 79, no. 8, pp. 1987–2002, Aug. 1996.

[121] J. G. P. Biner, *Advanced Ceramic Processing and Technology*. 1990.

[122] A. Simchi, F. Pishbin, and A. R. Boccaccini, "Electrophoretic deposition of chitosan," *Mater. Lett.*, vol. 63, no. 26, pp. 2253–2256, 2009.

[123] B. Ferrari and R. Moreno, "EPD kinetics: A review," *J. Eur. Ceram. Soc.*, vol. 30, no. 5, pp. 1069–1078, 2010.

[124] A. R. Boccaccini, C. Peters, J. A. Roether, D. Eifler, S. K. Misra, and E. J. Minay, "Electrophoretic deposition of polyetheretherketone (PEEK) and PEEK/Bioglass® coatings on NiTi shape memory alloy wires," *J. Mater. Sci.*, vol. 41, no. 24, pp. 8152–8159, 2006.

[125] L. V. Gambino, N. J. Magdefrau, and M. Aindow, "Microstructural effects of the reduction step in reactive consolidation of manganese cobaltite coatings on Crofer 22 APU," *Mater. High Temp.*, vol. 32, no. 1–2, pp. 142–147, 2015.

[126] D. J. Young, *High Temperature Oxidation and Corrosion of Metals, volume 1*. Elsevier, 2008.

[127] H. J. T. Ellingham, "Transactions and Communications," *J. Soc. Chem. Ind.*, vol. 63, no. 5, pp. 125–160, May 1944.

[128] Wikipedia, "Ellingham diagram," 2018. [Online]. Available: https://en.wikipedia.org/wiki/Ellingham_diagram. [Accessed: 25-Aug-2018].

[129] C. Wagner, "Beitrag zur theorie des anlaufvorgangs.," *Z. Phys. Chem.*, vol. B, no. 21, pp. 25–41, 1993.

[130] N. Birks, G. H. Meier, and F. S. Pettit, *Introduction to the High-Temperature Oxidation of Metals*. Cambridge: Cambridge University Press, 2006.

[131] A. C. S. Sabioni *et al.*, "About the role of chromium and oxygen ion diffusion on the growth mechanism of oxidation films of the AISI 304 austenitic stainless steel," *Oxid. Met.*, vol. 78, no. 3–4, pp. 211–220, 2012.

[132] J. G. Grolig, J. Froitzheim, and J. E. Svensson, "Coated stainless steel 441 as interconnect material for solid oxide fuel cells: Evolution of electrical properties," *J. Power Sources*, vol. 284, pp. 321–327, 2015.

[133] M. Linder *et al.*, "Model-based prediction of the ohmic resistance of metallic interconnects from oxide scale growth based on scanning electron microscopy," *J. Power Sources*, vol. 272, pp. 595–605, 2014.

[134] S. Molin, P. Jasinski, L. Mikkelsen, W. Zhang, M. Chen, and P. V. Hendriksen, "Low temperature processed MnCo2O4and MnCo1.8Fe0.2O4as effective protective coatings for solid oxide fuel cell interconnects at 750 ï¿½C," *J. Power Sources*, vol. 336, pp. 408–418, 2016.

[135] H. Liu, X. Zhu, M. Li, Q. Tang, G. Sun, and W. Yang, "Single Crystal (Mn,Co)3O4 Octahedra for Highly Efficient Oxygen Reduction Reactions," *Electrochimica Acta*, vol. 144. pp. 31–41, 2014.

[136] E. Lee, J. H. Jang, and Y. U. Kwon, "Composition effects of spinel MnxCo3-xO4nanoparticles on their electrocatalytic properties in oxygen reduction reaction in alkaline media," *J. Power Sources*, vol. 273, pp. 735–741, 2015.

[137] H. Zhu, S. Zhang, Y.-X. Huang, L. Wu, and S. Sun, "Monodisperse $M_x Fe_{3-x} O_4$ (M = Fe, Cu, Co, Mn) Nanoparticles and Their Electrocatalysis for Oxygen Reduction Reaction," *Nano Lett.*, vol. 13, no. 6, pp. 2947–2951, 2013.

[138] A. Khan and P. G. Smirniotis, "Relationship between temperature-programmed reduction profile and activity of modified ferrite-based catalysts for WGS reaction," *J. Mol. Catal. A Chem.*, vol. 280, no. 1–2, pp. 43–51, 2008.

[139] W. N. Liu, X. Sun, E. Stephens, and M. A. Khaleel, “Life prediction of coated and uncoated metallic interconnect for solid oxide fuel cell applications,” *J. Power Sources*, vol. 189, no. 2, pp. 1044–1050, 2009.

[140] H. S. Seo, G. Jin, J. H. Jun, D. H. Kim, and K. Y. Kim, “Effect of reactive elements on oxidation behaviour of Fe-22Cr-0.5Mn ferritic stainless steel for a solid oxide fuel cell interconnect,” *J. Power Sources*, vol. 178, no. 1, pp. 1–8, 2008.